Structure and Lattice Dynamics of GaN and AlN: Ab-Initio Investigations of Strained Polytypes and Superlattices

Dissertation

zur Erlangung des akademischen Grades
doctor rerum naturalium (Dr. rer. nat.)

vorgelegt dem Rat der Physikalisch-Astronomischen Fakultät
der Friedrich-Schiller-Universität Jena

von Dipl.-Phys. Jan-Martin Wagner
geboren am 24. Juli 1967 in Berlin

Gutachter:

1. Prof. Dr. F. Bechstedt, Jena
2. Prof. Dr. D. Strauch, Regensburg
3. Priv.-Doz. Dr. habil. A. Hoffmann, Berlin

Tag der letzten Rigorosumsprüfung: 16. Juli 2004

Tag der öffentlichen Verteidigung: 14. Oktober 2004

Rien n'est plus dangereux qu'une idée,
quand on n'a qu'une idée.

(Émile Chartier, dit Alain)

Woher
soll ich wissen,
was ich denke,
bevor ich höre,
was ich sage?

(N. N.)

Contents

Chapter 1

Introduction and Outline

Modern semiconductor technology has lead to a variety of beneficial and useful devices playing an important role in every-day life. For most applications, silicon is still the predominant material. However, since the demands regarding functionality are ever growing, different materials are introduced in areas where silicon is ill-suited. These are, e. g., optical communication as well as high-frequency, high-power, high-voltage, and high-temperature electronics. Here, substances like gallium arsenide (GaAs) or silicon carbide (SiC) are used [*Mor94*].

A specific goal of the last decade was to obtain a high-brightness blue light–emitting diode (LED) and its further development towards a laser diode (LD). For these devices, there are many possible applications in solid-state lighting and as versatile tools, e. g., in medicine, for ordinary and effect lighting, traffic lights etc. Most important, since standard compact disc and DVD players are based on long-wavelength infrared LDs, optical discs with much higher storage capacity would be possible if blue-light emitting LDs would be used to read the data tracks (which, in fact, will appear on the market in the near future [*CSN04*]). Due to the shorter wavelength, the blue light can be focused on a smaller area, allowing a higher storage density. SiC-based blue emitters, existing already for many years, have an output power far too low even to be used in a large-area full-colour display consisting of LEDs. This is because SiC is an indirect-gap material and therefore ill-suited for highly effective light emission; its blue luminescence comes from donor-acceptor pair recombinations as well as free and impurity-bound excitons.

First attempts to achieve blue luminescence from p–n junctions of direct-gap semiconductors were based on the wide-gap II–VI compounds zinc sulfide (ZnS) and zinc selenide (ZnSe) [*Rob75*, *Yam77*]. However, the lifetime of high-brightness ZnSe-based LEDs and LDs [*Haa91*] was severely limited by degradation, even if grown on homoepitaxial substrates [*Bon96*]. Therefore, as an alternative material system, among the III–V semiconductors the nitride compounds were taken into consideration [*Nak97*]. Due to its room-temperature band-gap energy of about 3.4 eV [*Mon74*], gallium nitride (GaN) is well-suited for light emission in the blue spectral region. Moreover, by alloying with aluminium and/or indium, an energetical range even wider than the whole visible spectrum can be covered, since InN has a (low-temperature) band gap of about 0.7 eV [*Dav02*], and AlN of about 6.1 eV [*Li03*], respectively. In contrast to other III–V compounds crystallizing in cubic zinc-blende (3*C*) structure, under ambient conditions, group-III nitrides crystallize in the hexagonal wurtzite (2*H*) structure. In epitaxial growth, however, also thin films of the metastable cubic phase can be obtained. Cubic AlN (c-AlN) is an indirect-

gap material with a minimum gap of about 5.3 eV [*Tho01*]. The room-temperature band gap of c-GaN (also known as β-GaN; α-GaN refers to the wurtzite polytype) is about 3.2 eV [*Ram94*], i. e., it is slightly lower than that of the hexagonal polytype. It can be expected that the same holds for the band gap of c-InN [*Bec02a*].

Due to the wurtzite structure and the high electronegativity of nitrogen, the $2H$ polytypes of the group-III nitrides are pyroelectric. Their spontaneous polarization is significantly larger than that of SiC and of pyroelectric II–VI semiconductors. Moreover, since pyroelectric crystals are always piezoelectric, the strain present in layered nitride structures modifies the polarization and, accordingly, the internal electric field. In turn, this affects the electronic and optical properties, especially for thin layers as, e. g., quantum wells [*Cho96*]. Therefore, strain is a very important issue for the group-III nitrides. On the other hand, the polarization difference between layers of different composition can be employed to create large sheet carrier concentrations at the interfaces. These "natural" two-dimensional electron gases (2DEGs) in the nitrides can be utilized as channel of a field-effect transistor, which can be used as high-power microwave amplifier [*Amb98*]. Since these 2DEGs result from a redistribution of charge from the bulk material due to the polarization-induced interface charge, other induced charges inside the device or, most important, at the surface must be eliminated by passivation in order to guarantee stable device operation. On the other hand, this surface sensitivity can be utilized to create various types of chemical detectors. Further possible applications of group-III nitrides include surface acoustic wave devices, photodetectors operating in the UV range, and solar cells absorbing the full solar spectrum.

However, using group-III nitrides for electronic devices leads to several problems. In general, they are very hard materials requiring special etching and polishing techniques. Ohmic contacts are not easily achieved [*PGN94*; chapter 10]. Most important, for a long time only n-type material had been available and, thus, successful p-type doping of GaN (using magnesium) was a main breakthrough [*Ama89*]. Furthermore, since their lattice constants differ from those of all well-established substrate materials, group-III nitrides are difficult to epitaxially grow without a high density of dislocations and considerable residual strains. The most common substrates for growing hexagonal GaN are [0001]-oriented sapphire (Al$_2$O$_3$) and $6H$-SiC. The former is usually covered first with a nucleation layer. For growing cubic polytypes, mainly [001]-oriented GaAs, $3C$-SiC, SiC-coated Si, or Si are used [*Miz86*, *Pai89*, *Liu93*, *Lei91*].

Although these epitaxies are far from the pseudomorphic growth mode, structures obtained are not completely relaxed and, hence, not free from strain. Considerable reduction of the dislocation density can be achieved by growth on patterned substrates, resulting in lateral overgrowth, and/or by first growing a relatively thick buffer layer structure. Because of the rather high growth temperatures (in the range of about $500 \ldots 1000$ °C; see, e. g., [*Jai00*]), thermal strains occur during cooling due to thermal misfit, i. e., deviating thermal expansion coefficients of epilayer and substrate. For instance, the resulting stress is compressive for hexagonal GaN grown on sapphire and tensile for GaN on $6H$-SiC [*Vol96*], respectively. The situation is even more complex for GaN/Al$_x$Ga$_{1-x}$N (and other, similar) heterostructures or superlattices, where a mutual influence of the different material layers occurs. Provided the layer height is less than the critical thickness, homogeneously strained structures are obtained [*Byk97*]. Although highly strained, such structures are free from cracks and have therefore been used as cladding layers for laser diodes [*Nak98*]. In general, other applications of nitride superlattices include the

creation of highly conductive *p*-type layers [*Koz99*] as well as Bragg reflectors [*Som98*]. Also, considering the electronic intersubband transitions in the quantum wells formed by the super-lattice, they are suited for optoelectronic applications in the infrared spectral region. For the operation of such devices a knowledge of their phonon properties is important [*Jov03*]. Nitride superlattices have been grown with a period of only a few monolayers [*Kis02*]. Furthermore, spontaneous ordering into thin layers has been observed for nitride alloys [*Kor97*, *Beh99*].

While most of the technical problems can be solved, the influence of strain on the performance of nitride-based devices remains an intrinsic physical effect. Since strain can noticeably change the desired characteristics, it has to be taken into account already in the design of a device. This requires both a profound understanding and a reliable theoretical modelling of strain effects in the nitrides. Furthermore, it is important to verify that after growth the strain is in the specified range. An easy way to experimentally evaluate the strain is provided by Raman spectroscopy, i.e., through measuring the frequencies of lattice vibrations. These depend on the inter-atomic forces, which change upon deformations of the material due to their nonlinear dependence on the distances between atoms [*She80*]. Comparing the measured frequencies with those of unstrained material therefore provides information about the strain. Then, using the so-called micro-Raman technique, the strain distribution can be determined with a spatial resolution in the order of $1\,\mu m$.

However, this is only possible if samples of sufficient quality are available allowing to isolate the strain influence from the experimental data, which then can be used as a reference. For a long time, such high-quality samples were not available; there were always problems with large background electron concentrations and high dislocation densities (in the order of up to 10^8 cm^{-2} [*Hof96*]). The elastic constants of GaN were determined only from powdered samples [*Sav78*]. The bulk modulus was not precisely known; experimental data ranged from 188 GPa [*Xia93*] to 245 GPa [*Per92*]. This, in turn, influenced the determination of the mode Grüneisen parameters, the phonon deformation potentials and the biaxial stress coefficients of the phonon modes [*Kis96*], which are key parameters for the characterization of strained materials using Raman spectroscopy. Moreover, the few available strain-related phonon data even deviated significantly from each other.

To overcome these problems of experimental uncertainty and lack of knowledge, first-principles calculations can be used, since they provide the requested data from a full quantum-mechanical treatment of the material investigated. Since no other experimental parameters than the atomic numbers and masses as well as the crystal structure are needed, these calculations are, in principle, able to reasonably predict experimental results, reaching sufficient accuracy to provide reliable data. For group-III nitrides, theoretical studies have started in the beginning of the '90s with calculations of structural, electronic and optical properties (see, e.g., [*Chr94*], chapter 4 of [*PGN94*], and references therein). These calculations required special care since the group-III nitrides are, similar to the II–VI compounds, highly ionic materials. Numerical difficulties arise due to the localized *d* orbitals of gallium and indium that are close in energy to the 2*s* state of nitrogen, which has been carefully investigated in several studies.

On the other hand, only few first-principles studies were devoted to the elastic and vibrational properties of the nitrides [*Miw93*, *Chr94*, *Kim94*, *Kim96*], determining elastic constants as well as phonon frequencies of unstrained crystals. The employed frozen-phonon method, however, limits these calculations to non-polar modes, thus no results could be ob-

tained for longitudinal-optical (LO) phonon frequencies. The influence of strain on the zone-center phonon frequencies was theoretically investigated only for the case of hydrostatic pressure [*Gor95*]. Since the Fröhlich coupling of LO phonons to electrons is governed both by the high-frequency and the static dielectric constant, also a knowledge of the dielectric properties of strained samples is necessary. According to the Lyddane–Sachs–Teller relation, the latter dielectric constant is related to the former one by the zone-center LO-phonon and transverse-optical-(TO-)phonon frequency. However, no such data are available in the literature. Therefore, a consistent description of the elastic properties and of the strain and stress dependence of phonon frequencies as well as of dielectric properties of wurtzite and cubic GaN and AlN is highly desirable. Moreover, a reliable result can only be obtained if structural changes under the influence of different deformations are fully taken into account. Especially the change of the cell-internal structural parameter u cannot be obtained from macroscopic elasticity theory, whose application would, in addition, have the drawback that its validity range is not known.

In this work, we investigate the strain dependence of the structural and dielectric properties as well as of the phonon frequencies of the nitride semiconductors GaN and AlN using quantum-mechanical first-principles calculations. For both the $3C$ and the $2H$ polytype as well as for short-period superlattices the strained crystal geometry and the corresponding phonon spectrum will be determined without using experimental parameters. Three types of strain will be considered for the bulk materials, corresponding to the application of hydrostatic pressure, of an isotropic biaxial stress in the basal plane, and of a uniaxial pressure along the crystal axis. For the $2H$ polytypes, the chosen deformations will preserve the wurtzite symmetry, whereas for the $3C$ polytypes the deformations will be directed along the crystallographic axes, resulting in a tetragonal structure.

On the one hand, these calculations are complementary to respective experimental investigations, both by helping to correctly interpret results and by providing information not easily accessible from experiments. On the other hand, the theoretical investigation yields valuable informations for the physical understanding of the material properties of the nitride compounds.

This thesis is structured as follows. After an overview of the theoretical fundamentals our calculations are based on (Chapter 2), we present the results in three parts: First, the properties of unstrained GaN and AlN are determined (Chapter 3), which are used as reference values for those in a strained state. Second, the strain dependence of the structural, dielectric and vibrational properties is investigated (Chapter 4). This requires to precisely calculate both the equilibrium and the strained crystal geometry. The results will be compared with a variety of experimental data in order to clarify existing discrepancies. Third, short-period superlattices are studied as a model system for layered nitride structures (Chapter 5). Our findings are concluded by a summary and an outlook, given in the last chapter.

Chapter 2

Fundamentals and Objectives

2.1 Preliminaries and Basic Approximations

From a quantum-mechanical point of view, a crystal — like any molecule — is a system of nuclei and electrons and, in equilibrium, is electrically neutral as a whole. It consists of a very large number of nuclei (and an even larger number of electrons), whereas (in most cases) the number of different kinds of nuclei (i. e., atomic species) is rather small. In thermal equilibrium, the nuclei of a perfect crystal are found (on the temporal average) at positions $\mathbf{R}\left(_\kappa^l\right)$ that, except for the surface, form a three-dimensional periodic array, the positions being labeled in the following way. One can identify a set consisting of the minimum number of nuclei required to make up the bulk crystal array by periodic repetition in space, which is called a basis. A part of space containing a basis and leading to a complete filling of the bulk crystal volume when translated along with the basis, neither overlapping itself nor leaving voids, is called a primitive cell. Then, the position of the κth nucleus (i. e., basis element) in the lth cell is, in general, given by

$$\mathbf{X}\left(_\kappa^l\right) = \mathbf{R}(l) + \boldsymbol{\tau}(\kappa) + \mathbf{u}\left(_\kappa^l\right) = \mathbf{R}\left(_\kappa^l\right) + \mathbf{u}\left(_\kappa^l\right), \tag{2.1}$$

with the Bravais lattice vector $\mathbf{R}(l)$, the basis vector $\boldsymbol{\tau}(\kappa)$, the equilibrium position $\mathbf{R}\left(_\kappa^l\right)$ and the momentary displacement $\mathbf{u}\left(_\kappa^l\right)$ of this nucleus, its mass being M_κ. In the presence of constant external stress, $\mathbf{R}\left(_\kappa^l\right)$ is still to be understood as the corresponding equilibrium position, which differs from the one of the unstrained crystal. As an abbreviation, let $\mathbf{X}$ denote the set of all displaced atomic positions, $\left\{\mathbf{X}\left(_\kappa^l\right)\right\}$, and let analogously $\mathbf{R} = \left\{\mathbf{R}\left(_\kappa^l\right)\right\}$ and $\mathbf{u} = \left\{\mathbf{u}\left(_\kappa^l\right)\right\}$.

Since all physical properties of a given system can be derived from its many-particle wavefunction, the fundamental problem of an ab-initio determination of these properties is to solve the stationary Schrödinger equation for the system, $\mathcal{H}^{\text{tot}}\Psi = E^{\text{tot}}\Psi$. Here, the Hamiltonian

$$\mathcal{H}^{\text{tot}} = \mathcal{T}^{\text{nuc}} + \mathcal{W}^{\text{n-n}} + \mathcal{T}^{\text{el}} + \mathcal{W}^{\text{e-e}} + \mathcal{W}^{\text{e-n}} \tag{2.2}$$

consists of the kinetic energy and the (pairwise) Coulomb interaction of the nuclei ($\mathcal{T}^{\text{nuc}} + \mathcal{W}^{\text{n-n}}$) and of the electrons ($\mathcal{T}^{\text{el}} + \mathcal{W}^{\text{e-e}}$) as well as of the (pairwise) Coulomb interaction between electrons and nuclei ($\mathcal{W}^{\text{e-n}}$). For $\mathcal{W}^{\text{e-e}}$, in diamagnetic systems (such as undoped semiconductors) the transverse interaction of the electrons does not play an important role: Since it is based on a vector potential whose sources are the magnetic momenta of the nuclei, the spin momenta of the

electrons, and the current densitites, and the expectation value of the latter vanishes, it suffices to assume spin degeneracy as well as to take into account only the bare Coulomb repulsion.

Viewed as a collection of atoms in a common bonding state, obviously atomic bonding and dynamics of a crystal refer mainly to the motions of electrons and nuclei, respectively. For studying the lattice dynamics in detail, it is therefore desirable to separate the electronic and nuclear subsystems within the quantum-mechanical description of the crystal. Born and Oppenheimer [*Bor27*; see also *Bor54,* Appendix VIII] showed that this is indeed possible provided that the conditions of the *adiabatic approximation* are fulfilled (see below). The adiabatic approximation is motivated by the fact that, due to the large mass difference, in thermal equilibrium the movement of the nuclei is rather slow (by oreders of magnitude) compared to that of the electrons. This leads to the assumption that, at least as long as no significant changes occur in the electronic subsystem, the movement of the nuclei does not depend on the actual positions of the electrons, $\mathbf{x} = \{\mathbf{x}_i\}$, since the former experience merely an average effect of the electron cloud. Stated another way, one assumes that, as the nuclei move, the electrons follow adiabatically, i. e., their distribution adjusts itself nearly instantaneously and, therefore, can be determined from a Schrödinger equation for fixed nuclei at *momentary* positions $\mathbf{X}$,

$$\mathcal{H}^{\text{frozen}}\psi_i = E_i^{\text{frozen}}\psi_i\,. \tag{2.3}$$

The corresponding Hamiltonian is that of a solid with a "frozen" lattice:

$$\mathcal{H}^{\text{frozen}} = \mathcal{T}^{\text{el}} + \mathcal{W}^{\text{e-e}} + \mathcal{W}^{\text{e-n}} + \mathcal{W}^{\text{n-n}}\,. \tag{2.4}$$

Since $\mathcal{H}^{\text{frozen}}$ depends parametrically on the coordinates of the nuclei, so do E_i^{frozen} and ψ_i. Then, the adiabatic approximation is formally obtained by two basic steps:[1] First, the wavefunction of the total system of nuclei and electrons, Ψ, is expanded in terms of the complete system of solutions of Eq. (2.3), keeping the dependence on all electronic coordinates *only* for the electronic wavefunction,

$$\Psi(\mathbf{X}, \mathbf{x}) = \sum_i \chi_i(\mathbf{X})\,\psi_i(\mathbf{X}, \mathbf{x})\,, \tag{2.5}$$

so that (using $\mathcal{T}^{\text{nuc}} = \sum_{l\kappa} \frac{1}{2M_\kappa}\mathcal{P}_{\binom{l}{\kappa}}^2$ with the momentum $\mathcal{P}_{\binom{l}{\kappa}}$ of the $\binom{l}{\kappa}^{\text{th}}$ nucleus) the Schrödinger equation of the total system reads (where $\langle\ |\ \rangle$ denotes the *scalar product* with respect to the *electronic* coordinates $\mathbf{x}$ only)

$$\begin{aligned} E_j^{\text{tot}}\chi_j &= \left(\mathcal{T}^{\text{nuc}} + E_j^{\text{frozen}}(\mathbf{X})\right)\chi_j \\ &\quad + \sum_i \left(\langle\psi_j|\,\mathcal{T}^{\text{nuc}}\psi_i\rangle + \sum_{l\kappa}\frac{1}{M_\kappa}\langle\psi_j|\,\mathcal{P}_{\binom{l}{\kappa}}\psi_i\rangle\,\mathcal{P}_{\binom{l}{\kappa}}\right)\chi_i\,. \end{aligned} \tag{2.6}$$

Second, the nondiagonal elements of the last term of Eq. (2.6) are dropped, since they involve a non-adiabatic coupling among electronic states (i. e., transitions) due to the movement of the nuclei, whereas a part of the diagonal ones can be shown to vanish and the other part to

---

[1] It was found that the adiabatic approximation can be used beyond the limits imposed by the older ansatz of Born and Oppenheimer (to expand the Hamiltonian in terms of the 4th root of the mass ratio between an electron and any of the nuclear masses). Here, we follow an approach proposed later by Born [*Bor54*; Appendix VIII].

be negligibly small [*Zim92*] (but see also [*Hau64*]). Obviously, the validity of the adiabatic approximation is limited by the second step; this will be further discussed below. Then, the Schrödinger equation of the crystal changes into an equation for the wavefunction of the nuclei, determined by the properties of the jth electronic state only:

$$\left(\mathcal{T}^{\text{nuc}} + E_j^{\text{frozen}}(\mathbf{X})\right)\chi_{jv} = E_{jv}^{\text{tot}}\chi_{jv}. \tag{2.7}$$

Here, v represents a vibrational quantum number. The energy of the "frozen" lattice, E_j^{frozen}, obviously acts as a potential term for the movement of the nuclei. It contains both the Coulomb interaction of the nuclei as well as the adiabatic contribution of the electrons to the total energy, thus it completely determines the properties of the vibrating lattice.

In general, the equilibrium positions $\mathbf{R}$ of the nuclei follow from the minimum of the free enthalpy. In this work, thermal effects are not investigated and the temperature is assumed to be 0 K. For zero external pressure, then, the free enthalpy reduces to the internal energy, which comprises both the static energy E^{frozen} as well as that of the zero-point motions. The latter one is neglected.[2] Then, the equilibrium positions $\mathbf{R}$ of the nuclei are (approximatively) given by the condition $(\nabla_{\mathbf{X}} E_j^{\text{frozen}})|_{\mathbf{X}=\mathbf{R}} = \mathbf{0}$. This means that, in general, they depend on the eigenstate the electronic subsystem is in.

In a state with total energy E_{jv}^{tot}, the wavefunction of the total system is given by $\Psi_{jv}(\mathbf{X}, \mathbf{x}) = \chi_{jv}(\mathbf{X})\,\psi_j(\mathbf{X}, \mathbf{x})$, i.e. effectively, the adiabatic approximation amounts to keeping only a single term from the expansion given by Eq. (2.5) [*Böt83*]. Since the terms neglected in Eq. (2.6) contain the electron-phonon coupling, the adiabatic approximation requires that no transitions shall occur in the electronic subsystem. To ensure this, the nuclei should move very slowly in comparison to the electrons, i.e. the frequencies of the nuclear motions must be much smaller than the characteristic electronic transition frequencies. This holds for insulators and semiconductors (in their ground state) exhibiting an energy gap between the occupied and non-occupied bands that implies electronic transition energies larger than the characteristic vibrational frequencies. Therefore, the adiabatic approximation is in principle expected to be sensible for wide-gap materials such as group-III nitrides GaN and AlN and, on the other hand, seemingly poor for metallic systems. However, it works well even for such systems because the Pauli principle guarantees that only few electrons near the Fermi level can undergo transitions [*Ven75, Böt83*].

As further approximations, in the following the crystal is assumed to be infinite and the electrons to be in their ground state. The latter condition is used since neither electronic transitions nor excited states are of interest in this work. The infinite crystal is modeled by periodic (or, cyclic) boundary conditions (as introduced by Born and von Kármán [*Bor12*]), which were shown to yield the correct asymptotic expression for the distribution of vibrational frequencies of a finite crystal [*Led43*; see also *Mar63*]. All energies refer to this macroscopic periodicity volume.

In this work, we determine the equilibrium positions of the nuclei for strained crystal structures (cf. Sect. 2.6) from a numerical calculation of the ground-state energy E_0^{frozen} using density-functional theory in local-density approximation and based on a plane wave–pseudopotential method (cf. the following Section). The vibrational properties are determined in the

---

[2] Cf. Sect. 2.3.1. This approximation leads to a minor systematic error in the volume dependence of the total energy. As a consequence, the equilibrium lattice constant (the equilibrium bulk modulus) will be determined somewhat too small (too large) [*Alc01*].

harmonic approximation (cf. Sect. 2.3) by density-functional perturbation theory (cf. Sect. 2.4), with some supplementary investigations based on frozen-phonon calculations (cf. Sect. 2.5).

2.2 Density-Functional Theory

After separation of the ionic and the electronic problem according to the adiabatic approximation, the total energy of a "frozen" lattice has to be calculated in order to obtain the full potential energy that determines the properties of the lattice. However, because of the large number of variables involved, an exact treatment of the eigenvalue problem of the corresponding Hamiltonian, Eq. (2.3), is impossible. Fortunately, it is possible to determine the desired ground-state properties of the electronic subsystem on the basis of an exact theory — the density functional theory (DFT). Its basic concepts as well as further approximations related to the numerical realization used in this work are described in the following subsections.

The (pairwise) Coulomb interaction of the nuclei, $\mathcal{W}^{\text{n-n}}$, does not influence the behavior of the electrons. This allows to split the the frozen-lattice Hamiltonian, Eq. (2.4), according to $\mathcal{H}^{\text{frozen}} = \mathcal{W}^{\text{n-n}} + \mathcal{H}^{\text{el}}$ and the ground-state energy is obtained as

$$E_0^{\text{frozen}} = W^{\text{n-n}} + E_0^{\text{el}}, \tag{2.8}$$

where $W^{\text{n-n}} = \langle \mathcal{W}^{\text{n-n}} \rangle_0$ formally is the ground-state expectation value of $\mathcal{W}^{\text{n-n}}$; it can be calculated analytically (cf. Sect. 2.2.6). E_0^{el} is the ground-state eigenvalue and ψ_0 the ground-state wavefunction of $\mathcal{H}^{\text{el}}$:

$$\mathcal{H}^{\text{el}} \psi_0 = E_0^{\text{el}} \psi_0. \tag{2.9}$$

Usually, one considers the electronic subsystem as being subject to an external potential. To achieve this representation, we rewrite the interaction between electrons and nuclei as

$$\mathcal{W}^{\text{e-n}} = -\frac{e^2}{4\pi\varepsilon_0} \sum_{i=1}^{N} \sum_{l\kappa} \frac{Z\binom{l}{\kappa}}{\left|\mathbf{x}_i - \mathbf{X}\binom{l}{\kappa}\right|} =: \int \varrho(\mathbf{r}) V^{\text{ext}}(\mathbf{r}) \, d\mathbf{r}, \tag{2.10}$$

where N is the number of electrons, e is the elementary charge, $Z\binom{l}{\kappa}$ is the atomic number of the $\binom{l}{\kappa}^{\text{th}}$ nucleus, ε_0 is the dielectric permittivity constant,

$$\varrho(\mathbf{r}) = \sum_{i=1}^{N} \delta(\mathbf{r} - \mathbf{x}_i) \tag{2.11}$$

is the electron density operator, and

$$V^{\text{ext}}(\mathbf{r}) = -\frac{e^2}{4\pi\varepsilon_0} \sum_{l\kappa} \frac{Z\binom{l}{\kappa}}{\left|\mathbf{r} - \mathbf{X}\binom{l}{\kappa}\right|} \tag{2.12}$$

is the external potential, which is a local single-particle potential. The electronic Hamiltonian then reads

$$\mathcal{H}^{\text{el}} = \mathcal{T}^{\text{el}} + \mathcal{W}^{\text{e-e}} + \int \varrho(\mathbf{r}) V^{\text{ext}}(\mathbf{r}) \, d\mathbf{r}. \tag{2.13}$$

Here, the external potential depends on the actual positions $\mathbf{X}$ of the nuclei and thus represents their influence on the electronic subsystem. Since the equilibrium positions of the nuclei are obtained from a respective minimization of E_0^{frozen}, it is necessary to calculate E_0^{el} for various positions $\mathbf{X}$, i.e., in dependence on V^{ext}. In the general theory, however, the specific nature of V^{ext} is unimportant. Instead, one focuses on the *principles* of how the properties of a many-electron system depend on the governing external potential. In the following, we present the theory in a way that emphasizes these general aspects and their consequences.

2.2.1 Hohenberg–Kohn Theorem and Variational Principle

The idea of using the electron density as a fundamental quantity was first proposed by Thomas [*Tho27*] and Fermi [*Fer27*, *Fer28*] in order to approximatively describe atomic systems. DFT in its present form, however, is an exact theory for a many-body system. It is based on the work of Hohenberg and Kohn on the inhomogeneous electron gas [*Hoh64*]. Assuming a Hamiltonian as given by Eq. (2.13) that contains a local $V^{\text{ext}}(\mathbf{r})$, they have shown that external potentials which differ by more than a constant lead to different ground-state densities $n(\mathbf{r})$ of the corresponding inhomogeneous electron gas. This means that, vice versa, V^{ext} is — up to an arbitrary constant — uniquely determined by n;[3] this is the fundamental Hohenberg–Kohn theorem. Since the external potential fixes the Hamiltonian, all physical properties of the system are implicitly determined by the ground-state density, which therefore can be used as fundamental quantity to describe many-electron systems.

This unique dependence on n can be used to construct auxiliary functionals allowing to derive a variational principle to determine of the ground-state density and energy of a given system as follows. We start by rewriting the eigenvalue equation for the ground-state energy, Eq. (2.9), as $E_0^{\text{el}} = \langle \psi_0 | \mathcal{H}^{\text{el}} \psi_0 \rangle$.[4] For a given electron-electron interaction, the eigenvalue E_0^{el} of all Hamiltonians $\mathcal{H}^{\text{el}}$ of type (2.13) depends only on the external potential. To emphasize this dependence on V^{ext}, the desired electronic ground-state energy is written as a functional

$$E_0^{\text{el}}[V^{\text{ext}}] := \left\langle \psi_0 \left| \left(\mathcal{T}^{\text{el}} + \mathcal{W}^{\text{e-e}} + \int \varrho(\mathbf{r}) V^{\text{ext}}(\mathbf{r}) \, \mathrm{d}\mathbf{r} \right) \psi_0 \right\rangle, \tag{2.14}$$

where ψ_0 is the normalized ground state corresponding to the given V^{ext}. Next we notice that in general, the functional dependence on V^{ext} can formally be transfered into a functional dependence on n. For a given ground-state density n, this is achieved by replacing the external potential with the one determined by virtue of the Hohenberg–Kohn theorem. This density-dependent[5] external potential is denoted as $V_{[n]}^{\text{ext}}$ [*Esch96*; p. 77]. However, this implies that $E_0^{\text{el}}[V_{[n]}^{\text{ext}}] = \left\langle \psi_{[n]} \left| \left(\mathcal{T}^{\text{el}} + \mathcal{W}^{\text{e-e}} + \int \varrho(\mathbf{r}) V_{[n]}^{\text{ext}}(\mathbf{r}) \, \mathrm{d}\mathbf{r} \right) \psi_{[n]} \right\rangle$ is fixed only up to an arbitrary constant [*Dre90*; p. 9], so that it is meaningless. Here, $\psi_{[n]}$ denotes the ground state corresponding to $V_{[n]}^{\text{ext}}$. Nevertheless, by subtracting the ambiguous contribution of the external potential [which

---

[3] This holds both for degenerate and non-degenerate ground states [*Lie83*]. The external potential, however, uniquely determines the ground-state density only for a non-degenerate ground state. — In the following, a non-degenerate ground state is assumed. However, the formulae are also valid for degenerate ground states [*Dre90*].

[4] As above, $\langle \ | \ \rangle$ denotes the scalar product with respect to all electronic coordinates.

[5] The index notation "$f_{[g]}$" indicates that a quantity f is uniquely determined by a function g but additionally is a function of some other variable(s), in contrast to a functional which is written as "$f[g]$." Both the index and the functional notation are used regardless whether the dependence of f on g is given explicitly or implicitly.

equals $\int n(\mathbf{r})V_{[n]}^{\text{ext}}(\mathbf{r})\,d\mathbf{r}$ since $\langle\psi_{[n]}|\varrho(\mathbf{r})\psi_{[n]}\rangle = n(\mathbf{r})$] one obtains a well-defined functional of the density [*Dre90, Esch96*; loc. cit.],

$$F[n] := E_0^{\text{el}}[V_{[n]}^{\text{ext}}] - \int n(\mathbf{r})V_{[n]}^{\text{ext}}(\mathbf{r})\,d\mathbf{r}, \tag{2.15}$$

which obviously can also be written as [*Dre90*; p. 10]

$$F[n] = \langle\psi_{[n]}|\,(\mathcal{T}^{\text{el}} + \mathcal{W}^{\text{e-e}})\psi_{[n]}\rangle. \tag{2.16}$$

For any given ground-state density, this yields the kinetic and Coulomb energy of the corresponding interacting many-particle system. Thus, for a given interaction $\mathcal{W}^{\text{e-e}}$, F is a well-defined universal functional since it is not related to a specific system.

The desired variational principle is based on the following general energy functional that, by virtue of F not depending on V^{ext}, allows to choose n and V^{ext} *independently* [*Esch96*],

$$E[n, V^{\text{ext}}] := F[n] + \int n(\mathbf{r})V^{\text{ext}}(\mathbf{r})\,d\mathbf{r}, \tag{2.17}$$

so that n can be varied for *fixed* V^{ext}: Hohenberg and Kohn have shown that, upon a variation of n (among all possible ground-state densities), $E[n, V^{\text{ext}}]$ reaches its minimal value — which equals the desired ground-state energy — for the specific n corresponding to the given V^{ext}. Therefore, one has for the (electronic) ground-state energy functional, Eq. (2.14), that

$$E_0^{\text{el}}[V^{\text{ext}}] = \min_n E[n, V^{\text{ext}}]. \tag{2.18}$$

Thus instead of solving the eigenvalue problem of the Hamiltonian (2.13), the exact ground-state energy (and density) of an interacting many-electron system can be obtained by minimizing the functional (2.17) with respect to the density n, a function of only three variables.[6]

2.2.2 Kohn–Sham Equation

Although it is well defined, no explicit expression is known for the functional F. Therefore, the variational principle of Hohenberg and Kohn is of no practical use for an immediate application. Moreover, even if one knows an explicit expression, one still lacks a systematic way how to vary n in order to find the ground state. To overcome the latter problem, Kohn and Sham have derived a set of self-consistent equations to be solved iteratively [*Koh65*]. Applying the variational principle, Eq. (2.18), to a *formally* non-interacting electron gas (i. e., $\mathcal{W}^{\text{e-e}} \equiv 0$), they obtained an expression for an effective external potential so that this auxiliary system has the *same* ground-state density (and energy) as the given interacting system.[7]

The most important aspect of the Kohn–Sham approach is that, since the Hamiltonian of a non-interacting system is a sum of single-particle operators, the many-particle wavefunction can

---

[6] The variational principle, as presented here, only holds for those densities n that correspond to the (possibly degenerate) ground state of any Hamiltonian of type (2.13); such densities are called V^{ext}-representable. However, not all "reasonably well-behaved" functions are V^{ext}-representable (see, e. g., chapter 2.3 of [*Dre90*]).

[7] This, of course, implies the assumption that ground-state densities of interacting systems are also obtainable as ground-state densities of non-interacting systems. The validity of this assumption is addressed in chapter 4.2 of [*Dre90*]; however, see also chapter 6.4 of [*Esch96*] for a different justification.

be composed of single-particle ones, φ_i, which obey individual Schrödinger equations. However, since the interaction-free electron gas is only an auxiliary system, these single-particle wavefunctions have no physical meaning, and the ground-state wavefunction of this auxiliary system is not the exact ground-state wavefunction of the interacting system. Merely the corresponding N-particle density (written here for the case of spin degeneracy; N is assumed even)

$$n(\mathbf{r}) = 2 \sum_{i=1}^{N/2} |\varphi_i(\mathbf{r})|^2, \tag{2.19}$$

obtained from the $N/2$ lowest-in-energy single-particle orbitals of the Kohn–Sham (KS) equation (where m is the free-electron mass)

$$\mathcal{H}^{\text{KS}}_{[n,V^{\text{ext}}]} \varphi_i(\mathbf{r}) \equiv \left(-\frac{\hbar^2}{2m} \nabla_{\mathbf{r}}^2 + V^{\text{KS}}_{[n,V^{\text{ext}}]} \right) \varphi_i(\mathbf{r}) = E_i^{\text{KS}} \varphi_i(\mathbf{r}) \tag{2.20}$$

equals the exact ground-state density of the interacting system; for the corresponding energy see below.

An iterative solution of Eq. (2.20) is possible since the local Kohn–Sham potential

$$V^{\text{KS}}_{[n,V^{\text{ext}}]} := V^{\text{ext}} + V^{\text{H}}_{[n]} + V^{\text{XC}}_{[n]} \tag{2.21}$$

allows to vary n for fixed V^{ext}. It consists of the external potential V^{ext} of the interacting system under consideration, the (classical electrostatic) Hartree potential

$$V^{\text{H}}_{[n]}(\mathbf{r}) = \frac{e^2}{4\pi \varepsilon_0} \int \frac{n(\mathbf{r}')}{|\mathbf{r} - \mathbf{r}'|} \, d\mathbf{r}', \tag{2.22}$$

and the Kohn–Sham exchange and correlation (XC) potential

$$V^{\text{XC}}_{[n]} := \frac{\delta E^{\text{XC}}}{\delta n}, \tag{2.23}$$

which is given by the functional derivative of the Kohn–Sham exchange and correlation energy E^{XC}. The latter is *defined* as

$$E^{\text{XC}}[n] := F[n] - E^{\text{H}}[n] - T_{\text{s}}[n], \tag{2.24}$$

with the Hohenberg–Kohn functional F of the interacting system, Eq. (2.16), the functional of the Hartree energy

$$E^{\text{H}}[n] := \frac{1}{2} \int n(\mathbf{r}) V^{\text{H}}_{[n]}(\mathbf{r}) \, d\mathbf{r}, \tag{2.25}$$

and the universal kinetic energy functional T_{s} of non-interacting particles (i. e., where the Hamiltonian is a sum of <u>s</u>ingle-particle operators).[8] The functional $T_{\text{s}}[n]$ is *defined* in the following

---

[8] Since in Eq. (2.24) the kinetic energy of the interacting system, as contained in F, is not completely compensated by T_{s}, E^{XC} differs from the true exchange and correlation energy $W^{\text{XC}}[n] := \langle \psi_{[n]} | \mathcal{W}^{\text{e-e}} \psi_{[n]} \rangle - E^{\text{H}}[n]$; see, e. g., chapters 2.6 and 4.2 of [*Esch96*] and Eqs. (4.16), (7.32), and (7.33) of [*Dre90*].

way: Consider the *given* ground-state density n as being a ground-state density of a fictitious Hamiltonian *without* electron-electron interaction,[9] $\mathcal{H}_{[n]}^{\mathrm{el,s}} = \mathcal{T}^{\mathrm{el}} + \int \varrho(\mathbf{r}) V_{[n]}^{\mathrm{ext}}(\mathbf{r}) \, d\mathbf{r}$, the corresponding ground-state wavefunction being $\psi_{[n]}^{\mathrm{s}}$. For this interaction-free system the Hohenberg–Kohn functional F, Eq. (2.16), obviously reduces to $\langle \psi_{[n]}^{\mathrm{s}} | \mathcal{T}^{\mathrm{el}} \psi_{[n]}^{\mathrm{s}} \rangle \equiv T_{\mathrm{s}}[n]$. Therefore, since F is a well-defined functional of n, so is T_{s} [*Esch96*; p. 79].

In the Kohn–Sham scheme, T_{s} can be calculated from

$$T_{\mathrm{s}}[n] = 2 \sum_{i=1}^{N/2} \left(-\frac{\hbar^2}{2m} \right) \int \varphi_i^*(\mathbf{r}) \nabla_{\mathbf{r}}^2 \varphi_i(\mathbf{r}) \, d\mathbf{r} . \tag{2.26}$$

The Kohn–Sham eigenvalues can be used to express the electronic ground-state energy of the *interacting* system as follows. From Eq. (2.20) and by using Eqs. (2.19), (2.21), (2.25), and (2.26) as well as the orthonormality of the Kohn–Sham orbitals one obtains

$$T_{\mathrm{s}}[n] = 2 \sum_{i=1}^{N/2} E_i^{\mathrm{KS}} - 2 E^{\mathrm{H}}[n] - \int n(\mathbf{r}) \left[V^{\mathrm{ext}}(\mathbf{r}) + V_{[n]}^{\mathrm{XC}}(\mathbf{r}) \right] d\mathbf{r} . \tag{2.27}$$

By expressing F through Eqs. (2.24) and (2.27), the energy functional the Hohenberg–Kohn variational principle is based on, Eq. (2.17), becomes

$$E[n, V^{\mathrm{ext}}] = 2 \sum_{i=1}^{N/2} E_i^{\mathrm{KS}} - E^{\mathrm{H}}[n] + E^{\mathrm{XC}}[n] - \int n(\mathbf{r}) V_{[n]}^{\mathrm{XC}}(\mathbf{r}) \, d\mathbf{r} , \tag{2.28}$$

the eigenvalues E_i^{KS} depending implicitly on n and V^{ext}, cf. Eq. (2.20). Once self-consistency is reached, Eq. (2.28) yields the desired electronic ground-state energy of the interacting many-particle system under consideration. This means that the gound-state properties of the latter are obtained from an effective single-particle formalism. Moreover, up to this point, the self-consistent Kohn–Sham scheme, as established by Eqs. (2.19)–(2.21), is mathematically exact. However, no explicit expression is known for $E^{\mathrm{XC}}[n]$. Thus, for practical applications, an approximation has to be used for E^{XC}, the most "popular" one being the local-density approximation (LDA), which is described in the following subsection.[10]

2.2.3 Local-Density Approximation

The Kohn–Sham XC energy functional can, in general, be written in the form

$$E^{\mathrm{XC}}[n] = \int n(\mathbf{r}) e_{[n]}^{\mathrm{XC}}(\mathbf{r}) \, d\mathbf{r} , \tag{2.29}$$

thereby defining the Kohn–Sham XC energy density $e_{[n]}^{\mathrm{XC}}$. For a homogeneous electron gas, the XC energy density is a spatially constant quantity and, hence, just a function of the ($\mathbf{r}$-independent) electron density, $e_{\mathrm{hom}}^{\mathrm{XC}}(n)$. Now, within the the local-density approximation (LDA; here and in the following, indicated by a *tilde*), $e_{[n]}^{\mathrm{XC}}$ is simply replaced by $e_{\mathrm{hom}}^{\mathrm{XC}}$:

$$\widetilde{E}^{\mathrm{XC}}[n] := \int n(\mathbf{r}) e_{\mathrm{hom}}^{\mathrm{XC}}\big(n(\mathbf{r})\big) \, d\mathbf{r} , \tag{2.30}$$

---

[9] See footnote 7.

[10] In principle, E^{XC} can be calculated exactly using a self-consistent perturbation approach [*Gör94, Gör95*]. However, the numerical effort is immense, hence this method is basically impracticable.

i. e. for the inhomogeneous electron gas at position **r** one uses the XC energy density of the homogeneous gas having an electron density given by the local value $n(\mathbf{r})$. Although one may assume the LDA to hold merely for spatially weakly varying densities, it has been found to work rather well also for solids with covalent bonds exhibiting large gradients of the charge density. This has been attributed to the fact that $(\widetilde{V}^{\mathrm{XC}} + V^{\mathrm{H}})$ fulfills the same sum rule which can be derived for the exact expression and that only the spherical average of the so-called exchange and correlation hole enters the XC energy within the exact theory. Therefore, particular details of the XC hole, not being reproduced by the LDA, are often unimportant and a partial cancellation of errors can usually be expected [*Dre90*; chapter 7.2].

However, there are some drawbacks related to the LDA, for systematic errors are being introduced in some calculations. Usually, the bonding is overestimated and, correspondingly, the lattice constants are underestimated. For certain semiconductors, the metal–insulator transition is obtained at too large volumina [*God89*]. One flaw of the LDA is that the Coulomb self-interaction is not properly cancelled by the local form of the exchange energy [*Dre90*]. Another one is that for free atoms the electron transfer energies from an s to a p or a d state (of the same main quantum number) are underestimated [*Gun85*].

Whereas the exchange part of $e_{\mathrm{hom}}^{\mathrm{XC}}$ can be calculated analytically, values for the correlation part have to be taken from numerical calculations. They have been parameterized using explicit functions. Here, we use the Perdew and Zunger parameterization [*Per81*] of the Monte Carlo calculation results obtained by Ceperley and Alder [*Cep80*].

2.2.4 Frozen-Core Approximation and Nonlinear Core Correction

In general, not all electrons contribute to the bonding of a crystal or a molecule: When the chemical environment of an atom changes, the inner shells remain closed. Therefore, the effort needed for a reasonable numerical modeling of the atomic binding in a crystal can be reduced if one assumes these states as being "frozen" in an ionic core and uses an effective ionic potential that acts on the remaining valence electrons. However, this independent treatment of core and valence electrons is possible only if, on the one hand, core regions of different atoms do not overlap and, on the other hand, the overlap of core and valence electron densities of an atom is rather small.[11] The latter condition can be troublesome for atoms exhibiting semicore states which overlap significantly both with the valence and the rest of the core electrons. This holds, e. g., for the $3d$ states of Gallium [*Gar93b*], which furthermore are close in energy to the $2s$ states of Nitrogen, so that for GaN they can be expected to contribute to the bonding.

In the Kohn–Sham scheme the frozen-core approximation amounts to splitting the total electron density, Eq. (2.19), into core and valence parts, $n = n_{\mathrm{c}} + n_{\mathrm{v}}$, and assuming the core electron density to be constant, so that it is sufficient to solve the Kohn–Sham equation for the valence electrons only. This requires an expression for the effective KS potential, Eq. (2.21), with n_{v} as its only variable. It is obtained as follows. The Hartree potential, Eq. (2.22), is linear in the density and provides no difficulties in defining $V_{[n_{\mathrm{c}}]}^{\mathrm{H}}$ and $V_{[n_{\mathrm{v}}]}^{\mathrm{H}}$. The XC potential, however,

---

[11] Strictly speaking, this is necessary only in those regions where the valence electron density varies significantly when the chemical environment changes; a large overlap of core and valence densities may still occur in regions where the latter remains approximately constant.

follows from the XC energy, which is nonlinear in the density. As further approximation, one splits the XC energy [assumed to be treated in LDA, Eq. (2.30)] as follows:

$$\widetilde{E}^{\mathrm{XC}}[n_{\mathrm{c}} + n_{\mathrm{v}}] \approx \widetilde{E}^{\mathrm{XC}}[n_{\mathrm{c}}] + \widetilde{E}^{\mathrm{XC}}[n_{\mathrm{v}}] + \widetilde{E}^{\mathrm{XC}}[n_{\mathrm{c}}, n_{\mathrm{v}}], \tag{2.31}$$

where the core part, $\widetilde{E}^{\mathrm{XC}}[n_{\mathrm{c}}] = \int n_{\mathrm{c}}(\mathbf{r}) e_{\mathrm{hom}}^{\mathrm{XC}}(n_{\mathrm{c}}(\mathbf{r})) \, d\mathbf{r}$, is constant and can be omitted (which amounts to shifting the energy zero), whereas the mixed part,

$$\widetilde{E}^{\mathrm{XC}}[n_{\mathrm{c}}, n_{\mathrm{v}}] := \int \left[n_{\mathrm{c}}(\mathbf{r}) e_{\mathrm{hom}}^{\mathrm{XC}}(n_{\mathrm{v}}(\mathbf{r})) + n_{\mathrm{v}}(\mathbf{r}) e_{\mathrm{hom}}^{\mathrm{XC}}(n_{\mathrm{c}}(\mathbf{r})) \right] d\mathbf{r}, \tag{2.32}$$

is neglected. Due to the locality of $e_{\mathrm{hom}}^{\mathrm{XC}}$, this approximation is justified for vanishing overlap of n_{c} and n_{v}. Then, one is left with $\widetilde{E}^{\mathrm{XC}}[n_{\mathrm{v}}]$, from which $\widetilde{V}_{[n_{\mathrm{v}}]}^{\mathrm{XC}}$ follows.

In the frozen-core approximation, core-level shifts and core polarization [*Shi97*] are neglected. Nevertheless, the frozen-core approximation has been found to be very successful. This is due to the fact that the error thereby introduced in the electronic ground-state energy is merely of second order in the density [*Bar80*].

However, if the overlap between n_{c} and n_{v} becomes non-negligible, the above splitting of $\widetilde{E}^{\mathrm{XC}}$ and the subsequent neglect of the mixed part, Eq. (2.32), introduces significant errors. For this case, Louie, Frøyen, and Cohen suggested a rigorous frozen-core treatment by not splitting the XC energy. For given V^{ext}, the KS potential is written as

$$\widetilde{V}_{[n_{\mathrm{c}}+n_{\mathrm{v}}]}^{\mathrm{KS}} = V_{[n_{\mathrm{c}}]}^{\mathrm{ion}} + V_{[n_{\mathrm{v}}]}^{\mathrm{H}} + \widetilde{V}_{[n_{\mathrm{c}}+n_{\mathrm{v}}]}^{\mathrm{XC}}, \quad \text{where} \quad V_{[n_{\mathrm{c}}]}^{\mathrm{ion}} = V^{\mathrm{ext}} + V_{[n_{\mathrm{c}}]}^{\mathrm{H}}. \tag{2.33}$$

Then, in the so-called nonlinear core correction (NLCC), one uses the sum of the *atomic* core-states' densities for n_{c}, which requires to calculate — once for all — the full core charge distribution (of the free atom). However, since the valence charge density is very small in the vicinity of the core, one can replace the true core charge density inside some (appropriately chosen) radius with some numerically easily manageable function; this helps to minimize numerical errors [*Lou82*].

2.2.5 Pseudopotentials and Plane-Wave Expansion

A pseudopotential was first used by Fermi [*Fer34*] in a study of high-lying atomic states, whereas for solids, the orthogonalized-plane-wave (OPW) method for electronic band-structure calculation [*Her40*] can be considered as a precursor to pseudopotential methods. The aim of a pseudopotential approach is to reduce the numerical effort needed for treating the valence electrons. The wavefunctions of the latter oscillate in the core region, since they must be orthogonal to those of the core states which are localized due to the (singular) Coulomb potential contained in V^{ion}, Eq. (2.33). These oscillations are unfavorable for an expansion of the valence wavefunctions in most basis sets, since they cause a significant change in the character of the wavefunctions when going from the inter-atomic to the core region.

However, as in the frozen-core approximation, one may assume that only the part of the valence wavefunction outside the core region contributes to the bonding. Therefore, both the valence wavefunction and the ionic potential need to be treated exactly in this region only, whereas inside the core region they may be altered so that the oscillations vanish. This degree

of freedom can be used in many different ways according to the objective of the specific calculation. In general, the pseudopotential represents a "pseudo ion," since it replaces both the ionic potential and the core electrons as well as their effects among themselves and on the valence electrons.

There are various categories of pseudopotentials differing with respect to the kind of input data required for their construction as, e. g., empirical pseudopotentials (using experimental lattice constants and reflection data) or model potentials (mimicking atomic scattering properties) [*Coh89*]. Based on an extension of the OPW method, a nonempirical approach to finding a pseudopotential was introduced by Phillips and Kleinman [*Phi59*]. They showed that by using smoothed Bloch functions as pseudo wavefunctions, the orthogonalization correction in the KS equation leads to a repulsive part of the pseudopotential that depends on the angular-momentum component of the pseudo wavefunction and therefore must be described by a nonlocal operator.

All these methods aim at describing a certain crystal of a given structure and atomic composition; transferability of the above-mentioned pseudopotentials is not guaranteed but has first been achieved by so-called norm-conserving pseudopotentials [*Ham79*]. They are based on a DFT-LDA solution of the atomic Schrödinger equation or, to include relativistic effects, the Dirac equation [*Kle80*] (or the Pauli equation); therefore, they are also called ab-initio (or first-principles) pseudopotentials. Different schemes for their generation can be found in the literature. First-principles pseudopotentials allow to accurately calculate total energies of different crystal phases and their lattice constants, structural properties of surfaces and interfaces, cohesive energies, bulk modulus, elastic constants, lattice vibrations, etc.

The choice of a specific pseudopotential depends both on the basis functions one is going to use as well as on the atomic composition of the material under consideration. In this work, in order to correctly treat differently strained structures as well as lattice vibrations, first-principles pseudopotentials and a plane-wave basis set (i. e., a Fourier expansion) are employed. The latter is not biased to a specific atomic arrangement and allows to systematically increase (and thereby check) the accuracy of the calculations by increasing the number of plane waves (i. e., taking into account higher Fourier coefficients). In a plane-wave basis, however, those atoms are not easy to manage that exhibit markedly localized states, or nodes in their wavefunctions, since these lead to contributions of high Fourier coefficients so that a large number of plane waves is required to model them. For group-III nitrides, this localization occurs for the the $2p$ states of nitrogen, since it has no p states in its core. Therefore, so-called soft (or smooth) pseudopotentials are required for the present calculations, since despite these problematic atomic states they lead to an expeditious convergence of the total energy with respect to an increase in the number of plane waves.

The softest (smoothest) norm-conserving pseudopotentials are obtained by the generation scheme of Troullier and Martins (TM) [*Tro91*]. The special properties of these pseudopotentials result from (i) the pseudo wavefunction being parameterized in the core region by a polynomial of 12th degree, (ii) the condition that the pseudo wavefunction and its first four derivatives are continuous at the core radius (i. e., the so-called cutoff radius), and (iii) the condition that the curvature of the total (i. e., not only the pseudo-ionic part) TM pseudopotential is zero at the nucleus. This allows to choose a rather large cutoff radius, which increases the smoothness (but might reduce the transferability) of the pseudopotential.

The conditions of the frozen-core approximation are well fulfilled for nitrogen and aluminium, whereas for gallium and indium the NLCC is required because of the semicore Ga 3*d* or In 4*d* electrons. For comparison, a Ga pseudopotential was created that treats the 3*d* electrons as completely frozen in the core. However, from this pseudopotential unusable results were obtained for GaN [*Kar97a*]. The core radius (and the NLCC parameters) of the TM pseudopotentials used in this work were chosen according to the concept of chemical hardness [*Tet93*, *Fil95*]. This method was implemented and the pseudopotentials were generated by Pletl [*Ple98*], who also fitted the pseudopotentials to the parameterization proposed by Bachelet, Hamann, and Schlüter, which allows a calculation of plane-wave matrix elements by an analytical expression [*Bac82*].

2.2.6 Total-Energy Calculation and Brillouin-Zone Summation

In the adiabatic approximation and using the Kohn–Sham DFT-LDA approach, the ground-state energy (per unit cell) of a frozen lattice follows, for given positions $\mathbf{X}$ of the nuclei (and therefore for given V^{ext}), as [cf. Eqs. (2.8), (2.17), (2.18), and (2.24)]

$$E_0^{\text{frozen}} = W^{\text{n-n}} + \min_n \left(T_s[n] + E^{\text{H}}[n] + \widetilde{E}^{\text{XC}}[n] + E^{\text{e-n}}[n, V^{\text{ext}}] \right), \tag{2.34}$$

where $E^{\text{e-n}}[n, V^{\text{ext}}] := \int n(\mathbf{r}) V^{\text{ext}}(\mathbf{r}) \, d\mathbf{r}$. For a crystal, the plane-wave basis functions are distinguished by the vector $\mathbf{k}$ that lies within the first Brillouin zone, the expansion extending over all vectors $\mathbf{G}$ of the reciprocal lattice. In the numerical calculation, however, the number of plane waves is limited by a so-called kinetic cutoff energy according to

$$\frac{\hbar^2}{2m} |\mathbf{k} + \mathbf{G}|^2 \leqq E_{\text{cut}}. \tag{2.35}$$

The total-energy contributions are calculated from the Fourier coefficients (i. e., in reciprocal space), except for the XC energy which is calculated in real space (using fast Fourier transforms). Due to the long-range character of the Coulomb potential involved in $W^{\text{n-n}}$, E^{H}, and $E^{\text{e-n}}$, their Fourier coefficients diverge for $\mathbf{G} = \mathbf{0}$. However, due to the overall charge neutrality, these divergencies cancel exactly. This allows to rewrite the sum of these three contributions as

$$W^{\text{n-n}} + E^{\text{H}} + E^{\text{e-n}} = E^{\text{Ew}} + \mathring{E}^{\text{H}} + \mathring{E}^{\text{e-n}}, \tag{2.36}$$

where the divergent terms have been omitted from the ringed quantities but included into the interaction energy of the nuclei, which then can be calculated analytically by an Ewald summation techique [*Mar63*] — and therefore (in that form) is called Ewald energy E^{Ew}.

In a crystal described by periodic boundary conditions, there exists a dense mesh of "allowed" $\mathbf{k}$ points in the Brillouin zone. Accordingly, the sum over the Kohn–Sham eigenvalues becomes a sum over all occupied bands (index ν) in the first Brillouin zone (BZ); it is therefore called band-structure energy

$$E^{\text{bs}} := 2 \sum_{j=1}^{N/2} E_j^{\text{KS}} = 2 \sum_{\nu} \sum_{\mathbf{k} \in \text{BZ}}^{\text{occ.}} E_\nu^{\text{KS}}(\mathbf{k}). \tag{2.37}$$

For the numerical calculation, only a finite number of $\mathbf{k}$ can be taken into account. Therefore, one usually chooses a set of so-called special $\mathbf{k}$-points (SP) adapted to the crystal symmetry. Any sum of the form $\sum_{\mathbf{k}\in\mathrm{BZ}} f(\mathbf{k})$ then becomes a weighted sum $\sum_{\mathbf{k}\in\mathrm{SP}} w_\mathbf{k} f(\mathbf{k})$ with $\sum_{\mathbf{k}\in\mathrm{SP}} w_\mathbf{k} = 1$. The KS equation is now solved for these special $\mathbf{k}$-points only, thus the numerical effort scales linearly with the number of special points. In the literature a variety of schemes for choosing special $\mathbf{k}$-points can be found (see, e. g., [*Eva83*]). In this work, sets of Chadi-Cohen special points [*Cha73*] are used, which have been found to ensure a good convergence for phonon calculations, both of zinc-blende and wurtzite nitrides [*Kar97a, Kar97b*].

Using the Ewald and the band-structure energy as well as Eq. (2.27) for T_s, the ground-state total energy of the frozen lattice can be written as [cf. Eq. (2.28)]

$$E_0^{\mathrm{frozen}} = E^{\mathrm{Ew}} + \min_n \left(E^{\mathrm{bs}} - \mathring{E}^{\mathrm{H}}[n] + \widetilde{E}^{\mathrm{XC}}[n] - \int n(\mathbf{r})\widetilde{V}_{[n]}^{\mathrm{XC}}(\mathbf{r}) \right). \tag{2.38}$$

In this work, the two XC contributions are abbreviated as

$$\widetilde{E}^{\Delta\mathrm{XC}}[n] := \widetilde{E}^{\mathrm{XC}}[n] - \int n(\mathbf{r})\widetilde{V}_{[n]}^{\mathrm{XC}}(\mathbf{r})\,\mathrm{d}\mathbf{r}. \tag{2.39}$$

This nomenclature will be used in the context of frozen-phonon calculations (Sect. 2.5).

2.3 Lattice Dynamics in the Harmonic Approximation

2.3.1 Potential Energy Expansion and Equation of Motion

The harmonic approximation is motivated by the fact that for sufficiently low temperatures (i. e., well below the melting point) the amplitudes of the atomic vibrations are usually small (as compared to the interatomic distances) and anharmonic effects (as, e. g., thermal expansion of the lattice, temperature dependence of elastic constants, or interactions of lattice vibrations) can be neglected. This is assumed throughout this work. Then, the potential energy of the lattice, which is given by $E_0^{\mathrm{frozen}}(\mathbf{X})$, can be approximated by a Taylor series up to quadratic terms in the atomic displacements as

$$\begin{aligned}\Phi(\mathbf{u}) &:= E_0^{\mathrm{frozen}}(\mathbf{X}) - E_0^{\mathrm{frozen}}(\mathbf{R}) \\ &= \sum_{\alpha l\kappa} \Phi_\alpha\binom{l}{\kappa} u_\alpha\binom{l}{\kappa} + \frac{1}{2}\sum_{\alpha l\kappa}\sum_{\beta l'\kappa'} \Phi_{\alpha\beta}\binom{l\ l'}{\kappa\ \kappa'} u_\alpha\binom{l}{\kappa} u_\beta\binom{l'}{\kappa'} + O(\mathbf{u}^3),\end{aligned} \tag{2.40}$$

with

$$\Phi_\alpha\binom{l}{\kappa} = \left.\frac{\partial E_0^{\mathrm{frozen}}}{\partial u_\alpha\binom{l}{\kappa}}\right|_{\mathbf{u}=0} \quad \text{and}$$

$$\Phi_{\alpha\beta}\binom{l\ l'}{\kappa\ \kappa'} = \left.\frac{\partial^2 E_0^{\mathrm{frozen}}}{\partial u_\alpha\binom{l}{\kappa}\,\partial u_\beta\binom{l'}{\kappa'}}\right|_{\mathbf{u}=0} \tag{2.41}$$

being the so-called atomic force constants of first and second order, respectively. They are interrelated due to the crystal symmetry and due to their invariance against rigid-body translations and rotations [*Bor54, Mar63, Ven75, Böt83*].

In the equilibrium configuration all forces vanish:

$$\Phi_\alpha \begin{pmatrix} l \\ \kappa \end{pmatrix} = 0 \quad (\forall\, \alpha, l, \kappa), \tag{2.42}$$

so that in harmonic approximation, the potential energy can be written as

$$\Phi^{\text{harm}}(\mathbf{u}) = \frac{1}{2} \sum_{\alpha l \kappa} \sum_{\beta l' \kappa'} \Phi_{\alpha\beta} \begin{pmatrix} l\ l' \\ \kappa\ \kappa' \end{pmatrix} u_\alpha \begin{pmatrix} l \\ \kappa \end{pmatrix} u_\beta \begin{pmatrix} l' \\ \kappa' \end{pmatrix}. \tag{2.43}$$

The harmonic approximation is of general use, regardless of a (semi-)classical or quantum-mechanical treatment of the lattice vibrations. Since in this work quantum aspects of lattice vibrations are unimportant, in the following the movement of the nuclei is described as that of a classical charged point mass (i. e., zero-point vibrations are neglected; cf. Sect. 2.1). The harmonic approximation is used since thermal effects are generally neglected and only the stationary vibrational properties shall be investigated.

If the κth basis atom in the lth cell is displaced from its equilibrium position, it is exposed to a force given by

$$F_\alpha \begin{pmatrix} l \\ \kappa \end{pmatrix} = -\frac{\partial\, \Phi^{\text{harm}}}{\partial u_\alpha \begin{pmatrix} l \\ \kappa \end{pmatrix}} = -\sum_{\beta l' \kappa'} \Phi_{\alpha\beta} \begin{pmatrix} l\ l' \\ \kappa\ \kappa' \end{pmatrix} u_\beta \begin{pmatrix} l' \\ \kappa' \end{pmatrix}, \tag{2.44}$$

which yields the classical equation of motion

$$M_\kappa \ddot{u}_\alpha \begin{pmatrix} l \\ \kappa \end{pmatrix} = -\sum_{\beta l' \kappa'} \Phi_{\alpha\beta} \begin{pmatrix} l\ l' \\ \kappa\ \kappa' \end{pmatrix} u_\beta \begin{pmatrix} l' \\ \kappa' \end{pmatrix}. \tag{2.45}$$

2.3.2 Dynamical Matrix and Phonons

For solving Eq. (2.45), the translational symmetry of the crystal is employed in choosing a basis system of complex functions (whose superposition is supposed to yield real displacements) [*Ven75*; Sect. 2.2.6]:

$$u_\alpha \begin{pmatrix} l \\ \kappa \end{pmatrix} = \frac{1}{\sqrt{M_\kappa}} U_\alpha(\kappa | \mathbf{q})\, \mathrm{e}^{\mathrm{i}[\mathbf{q}\cdot\mathbf{R}(l) - \omega(\mathbf{q})t]}, \tag{2.46}$$

where the notation $U_\alpha(\kappa | \mathbf{q})$ indicates that the amplitude factor for the displacement of the κth atom is considered for the case of a vibration with wave vector $\mathbf{q}$. The grid of "allowed" wave vectors $\mathbf{q}$ is determined by the periodic boundary conditions. If the crystal basis consists of N_{b} atoms, on inserting (2.46) into (2.45) one obtains a system of $3N_{\text{b}}$ equations

$$\omega^2(\mathbf{q})\, U_\alpha(\kappa | \mathbf{q}) = \sum_{\kappa' \beta} \mathcal{D}_{\alpha\beta} \begin{pmatrix} \mathbf{q} \\ \kappa\ \kappa' \end{pmatrix} U_\beta(\kappa' | \mathbf{q}) \quad (\alpha = x, y, z;\ \kappa = 1, \dots, N_{\text{b}}), \tag{2.47}$$

where

$$\mathcal{D}_{\alpha\beta} \begin{pmatrix} \mathbf{q} \\ \kappa\ \kappa' \end{pmatrix} = \frac{1}{\sqrt{M_\kappa M_{\kappa'}}} \sum_{l'} \Phi_{\alpha\beta} \begin{pmatrix} l\ l' \\ \kappa\ \kappa' \end{pmatrix} \mathrm{e}^{\mathrm{i}\mathbf{q}\cdot[\mathbf{R}(l) - \mathbf{R}(l')]}$$

$$= \frac{1}{\sqrt{M_\kappa M_{\kappa'}}} \sum_{l''} \Phi_{\alpha\beta} \begin{pmatrix} 0\ l'' \\ \kappa\ \kappa' \end{pmatrix} \mathrm{e}^{\mathrm{i}\mathbf{q}\cdot\mathbf{R}(l'')} \quad (l'' = l' - l). \tag{2.48}$$

The last step follows from the lattice periodicity of the potential. Since $\Phi_{\alpha\beta}\left(\begin{smallmatrix} l & l' \\ \kappa & \kappa' \end{smallmatrix}\right)$ is symmetric in the index sets (α, l, κ) and (β, l', κ') [cf. Eq. (2.41)], the $\mathcal{D}_{\alpha\beta}\left(\begin{smallmatrix} \mathbf{q} \\ \kappa & \kappa' \end{smallmatrix}\right)$ form a Hermitian matrix; it is called dynamical matrix. Except for the additional mass factors the dynamical matrix represents the Fourier transform of the second-order force constant matrix with respect to the lattice vector $\mathbf{R}(l)$.

According to Eq. (2.47), the equation of motion (2.45) is solved if and only if the eigenvalues and eigenvectors of the dynamical matrix are found, which follow from the the so-called secular equation (where $\mathbb{1}$ is the identity matrix of the specified dimension):

$$\det\left[\,\boldsymbol{\mathcal{D}}(\mathbf{q}) - \omega^2(\mathbf{q})\,\mathbb{1}_{3N_{\mathrm{b}}}\,\right] = 0\,. \tag{2.49}$$

Since $\boldsymbol{\mathcal{D}}(\mathbf{q})$ is Hermitian, for each $\mathbf{q}$ one gets real eigenvalues $\omega_j^2(\mathbf{q})$ $(j = 1, \ldots, 3N_{\mathrm{b}})$. They establish the dispersion relations of the lattice vibrations. The stability of the lattice requires all $\omega_j(\mathbf{q})$ being real. According to the symmetry of the crystal, at some points $\mathbf{q}$ in the Brillouin zone the eigenfrequencies $\omega_j(\mathbf{q})$ may be degenerate. In the long-wavelength limit (i. e., $\mathbf{q} \to \mathbf{0}$), three modes have zero frequency, corresponding to a rigid translation of the crystal as a whole (along three mutually perpendicular directions). These branches are referred to as acoustic modes, the remaining $3N_{\mathrm{b}} - 3$ ones as optical modes.

Substituting the amplitude factor as

$$U_\alpha\left(\kappa\,\big|\,\begin{smallmatrix} \mathbf{q} \\ j \end{smallmatrix}\right) = A\left(\begin{smallmatrix} \mathbf{q} \\ j \end{smallmatrix}\right) e_\alpha\left(\kappa\,\big|\,\begin{smallmatrix} \mathbf{q} \\ j \end{smallmatrix}\right) \tag{2.50}$$

allows to choose dimensionless eigenvectors $\mathbf{e}\left(\begin{smallmatrix} \mathbf{q} \\ j \end{smallmatrix}\right)$ of the $(3N_{\mathrm{b}} \times 3N_{\mathrm{b}})$-dimensional matrix $\boldsymbol{\mathcal{D}}(\mathbf{q})$ that fulfill the normalization condition (where $\dagger$ indicates transposition combined with complex conjugation, i. e., Hermitian conjugation)

$$\mathbf{e}^\dagger\left(\begin{smallmatrix} \mathbf{q} \\ j \end{smallmatrix}\right) \cdot \mathbf{e}\left(\begin{smallmatrix} \mathbf{q} \\ j' \end{smallmatrix}\right) = \sum_{\alpha\,\kappa} e_\alpha^*\left(\kappa\,\big|\,\begin{smallmatrix} \mathbf{q} \\ j \end{smallmatrix}\right) e_\alpha\left(\kappa\,\big|\,\begin{smallmatrix} \mathbf{q} \\ j' \end{smallmatrix}\right) = \delta_{jj'}\,. \tag{2.51}$$

Their completeness can be expressed in mixed matrix and component notation as

$$\sum_j \left[\mathbf{e}\left(\begin{smallmatrix} \mathbf{q} \\ j \end{smallmatrix}\right) \cdot \mathbf{e}^\dagger\left(\begin{smallmatrix} \mathbf{q} \\ j \end{smallmatrix}\right)\right]_{\alpha\beta}(\kappa\kappa') = \sum_j e_\alpha\left(\kappa\,\big|\,\begin{smallmatrix} \mathbf{q} \\ j \end{smallmatrix}\right) e_\beta^*\left(\kappa'\,\big|\,\begin{smallmatrix} \mathbf{q} \\ j \end{smallmatrix}\right) = \delta_{\kappa\kappa'}\,\delta_{\alpha\beta}\,. \tag{2.52}$$

From Eqs. (2.46) and (2.50) it follows that for a vibrational mode j with wave vector $\mathbf{q}$ the amplitude $\hat{\mathbf{u}}\left(\kappa\,\big|\,\begin{smallmatrix} \mathbf{q} \\ j \end{smallmatrix}\right)$ of the displacement $\mathbf{u}\left(\begin{smallmatrix} l \\ \kappa \end{smallmatrix}\,\big|\,\begin{smallmatrix} \mathbf{q} \\ j \end{smallmatrix}\right)$ of the κth basis atom in the lth cell is given by

$$\hat{u}_\alpha\left(\kappa\,\big|\,\begin{smallmatrix} \mathbf{q} \\ j \end{smallmatrix}\right) = A\left(\begin{smallmatrix} \mathbf{q} \\ j \end{smallmatrix}\right) e_\alpha\left(\kappa\,\big|\,\begin{smallmatrix} \mathbf{q} \\ j \end{smallmatrix}\right)\big/\sqrt{M_\kappa}\,. \tag{2.53}$$

Upon transformation to so-called normal coordinates and generalized momenta, these modes become vibrations of independent harmonic oscillators. The quantum-mechanical behavior of the latter leads to the picture of vibrational quanta called phonons, a nomenclature that is also used in the present classical description.

In this work, the vibrational properties are determined from a direct numerical calculation of the dynamical matrix and a subsequent diagonalization that yields the mode frequencies and eigenvectors. This calculation is based on density-functional perturbation theory (cf. Sect. 2.4). Additionally, in some cases also the so-called frozen-phonon method is used (cf. Sect. 2.5).

2.3.3 Long-Wavelength Limit in Polar Crystals

Lattice vibrations of any finite wavelength in polar semiconductors can be treated in the same way as those of nonpolar ones. The long-wavelength limit (i. e., $\mathbf{q} \to \mathbf{0}$), however, needs special attention, since the long-range character of the Coulomb interaction causes a macroscopic electric field $\mathbf{E}$ for optical modes, where oppositely charged sublattices vibrate against each other and create a dynamical dipole moment. Vice versa, the vibrating ions are coupled to this field. However, since the corresponding potential energy $V_{\mathbf{E}}(\mathbf{r}) = e\,\mathbf{E} \cdot \mathbf{r}$ does not have the periodicity of the lattice, this coupling has not been taken into account in the harmonic approximation based on a periodic potential.

2.3.3.1 Determination of the Dynamical Matrix

Following Born and Huang [*Bor54*; Chap. 33], this coupling can be treated phenomenologically by taking into account in the potential energy of the vibrating lattice the appropriate contributions due to the electric field. In the long-wavelength limit, the displacements of the κth atom are identical in each cell and it suffices to consider a single primitive cell (so that one can suppress the cell index l). In contrast to Eq. (2.43), here the potential-energy *density* ϕ is considered and a slightly different notation for its "purely mechanical" contribution (i. e., the one being solely determined by the atomic force constants) is used, emphasizing its relation to the corresponding part of the dynamical matrix (see below). In general,[12]

$$
\begin{aligned}
\phi_{\mathbf{q} \to \mathbf{0}}(\mathbf{u}) = {}& \frac{1}{2} \sum_{\kappa \kappa'} \mathbf{u}(\kappa) \cdot \boldsymbol{C}(\kappa \kappa') \cdot \mathbf{u}(\kappa') \\
& - \frac{\varepsilon_0}{2}\, \mathbf{E} \cdot \boldsymbol{\varepsilon}_\infty \cdot \mathbf{E} - \frac{e}{V} \sum_{\kappa} \mathbf{E} \cdot \boldsymbol{Z}_{\mathrm{B}}(\kappa) \cdot \mathbf{u}(\kappa),
\end{aligned}
\tag{2.54}
$$

depends on the direction $\vec{q} := \mathbf{q}/|\mathbf{q}|$ along which the limit $\mathbf{q} \to \mathbf{0}$ is reached (see below). Here, besides the matrix $\boldsymbol{C}(\kappa \kappa')$, which will be discussed below, the following quantities appear: $\mathbf{E}$ is the macroscopic electric field accompanying the lattice vibrations. It is considered in the electrostatic approximation [*Ven75*; Sect. 4.3.4], so that polariton effects are not taken into account. Therefore, the $\mathbf{q} \to \mathbf{0}$ limit is restricted to $|\mathbf{q}| \gg \omega_{\max}/c$ (with $\omega_{\max}$ being the maximum frequency of the vibrating lattice). This corresponds to the case of Raman scattering using visible light. Considering a Fourier component [with spatial variation $\exp(\mathrm{i}\mathbf{q}\cdot\mathbf{r})$] of $\mathbf{E}$, in the electrostatic approximation it is given through $\mathbf{E} = -\vec{q}\varepsilon_0^{-1}\vec{q} \cdot \mathbf{P}$, with $\mathbf{P}$ being the total polarization present in the crystal. $\boldsymbol{\varepsilon}_\infty$ is the tensor of the electronic dielectric constant of the crystal, V is the volume of the primitive cell, and $\boldsymbol{Z}_{\mathrm{B}}(\kappa)$ is the tensor of the Born effective charge of the κth atom, introduced to describe the coupling between the atomic displacement and the electric field. Both $\boldsymbol{\varepsilon}_\infty$ and $\boldsymbol{Z}_{\mathrm{B}}(\kappa)$ are considered in their $\mathbf{q} \to \mathbf{0}$ limit. The (dynamical) dipole moment of the primitive cell, caused by the displacement of the ions, is given by

$$
\mathbf{p} = e \sum_{\kappa} \boldsymbol{Z}_{\mathrm{B}}(\kappa) \cdot \mathbf{u}(\kappa).
\tag{2.55}
$$

---

[12] Any quantity printed in bold upright is a vector, whereas boldface italic indicates a matrix. If a vector is multiplied from the left, this is to be understood as a matrix product with the transpose of the vector.

The Born effective charge takes into account both the valence charge $Z_{val}(\kappa)$ of the ions and the change in the electronic charge distribution caused by the displacement of the ions. Due to charge neutrality of the primitive cell, it holds that $\sum_\kappa \mathbf{Z}_B(\kappa) = \mathbf{0}$ [*Coc62*].

The force entering the equation of motion is obtained from Eq. (2.54). It can be written as[13]

$$F_\alpha(\kappa) = -V \frac{\partial \phi(\mathbf{u})}{\partial u_\alpha(\kappa)} = -V \sum_{\beta \kappa'} C_{\alpha\beta}(\kappa\kappa') u_\beta(\kappa') + e \left[\mathbf{Z}_B^{tr}(\kappa) \cdot \mathbf{E} \right]_\alpha . \tag{2.56}$$

Obviously, in the long-wavelength limit, the dynamical matrix consists of two different contributions: A (mathematically) regular one from the forces due to the lattice-periodic potential (at zero macroscopic field), which is identical to the expression given by Eq. (2.48), and a (mathematically) non-analytic one from the forces due to the macroscopic electric field:

$$\boldsymbol{\mathcal{D}} \begin{pmatrix} \mathbf{q} \to \mathbf{0} \\ \kappa \kappa' \end{pmatrix} = \boldsymbol{\mathcal{D}}^{rg} \begin{pmatrix} \mathbf{q} \to \mathbf{0} \\ \kappa \kappa' \end{pmatrix} + \boldsymbol{\mathcal{D}}^{n.a.} \begin{pmatrix} \mathbf{q} \to \mathbf{0} \\ \kappa \kappa' \end{pmatrix}. \tag{2.57}$$

The latter contribution is non-analytic since it has no unique limit for $\mathbf{q} \to \mathbf{0}$ but depends on the direction $\vec{q}$ in which the limit is taken. This is due to the last term in Eq. (2.54) depending on the angle between the macroscopic electric field and the dipole moment $\mathbf{p}$ of the vibrating lattice. Therefore, in Eq. (2.54) the "purely mechanical" contribution follows from the regular part of the dynamical matrix:[14]

$$C(\kappa\kappa') := \frac{\sqrt{M_\kappa M_{\kappa'}}}{V} \boldsymbol{\mathcal{D}}^{rg} \begin{pmatrix} \mathbf{q} \to \mathbf{0} \\ \kappa \kappa' \end{pmatrix} = \frac{1}{V} \sum_{l''} \boldsymbol{\Phi} \begin{pmatrix} 0 \; l'' \\ \kappa \kappa' \end{pmatrix}. \tag{2.58}$$

The non-analytic part of the dynamical matrix is determined as follows. The total macroscopic polarization contains contributions arising from the electric field (independent of the atomic displacement) and, vice versa, from the atomic displacement (independent of the field):

$$\mathbf{P} = \varepsilon_0 (\boldsymbol{\varepsilon}_\infty - \mathbb{1}) \cdot \mathbf{E} + \frac{e}{V} \sum_\kappa \mathbf{Z}_B(\kappa) \cdot \mathbf{u}(\kappa), \tag{2.59}$$

This allows to relate the electric field directly to the atomic displacements:

$$\begin{aligned} \mathbf{E} &= -\vec{q}\varepsilon_0^{-1}\vec{q} \cdot \mathbf{P} \\ &= -\frac{e}{\varepsilon_0 V} \left[\mathbb{1} + \vec{q}\vec{q} \cdot (\boldsymbol{\varepsilon}_\infty - \mathbb{1}) \right]^{-1} \cdot \vec{q}\vec{q} \cdot \sum_\kappa \mathbf{Z}_B(\kappa) \cdot \mathbf{u}(\kappa), \end{aligned} \tag{2.60}$$

which can be shown to result in [*Ven75*; Eq. (4.108)]

$$\mathbf{E} = -\frac{e}{\varepsilon_0 V} \vec{q} \frac{1}{\vec{q} \cdot \boldsymbol{\varepsilon}_\infty \cdot \vec{q}} \vec{q} \cdot \sum_\kappa \mathbf{Z}_B(\kappa) \cdot \mathbf{u}(\kappa). \tag{2.61}$$

---

[13] Note that here the transpose of $\mathbf{Z}_B$ appears since compared to Eq. (2.54) the ordering in the multiplication with $\mathbf{E}$ has been interchanged.

[14] As normalization volume, here the volume of the primitive cell appears, since the l' summation in Eq. (2.43) is taken up by the dynamical matrix, Eq. (2.48), whereas the l summation leads to a factor of N_{pc}, the number of primitive cells in the periodicity volume considered by the periodic boundary conditions. However, this factor cancels with the one appearing in the normalization of the energy density $\phi = \Phi/(N_{pc} V)$.

Inserting the electric field, Eq. (2.61), into the equation for the force, Eq. (2.56), finally leads to the following expression for the non-analytic part of the dynamical matrix:[15]

$$
\mathcal{D}_{\alpha\beta}^{\mathrm{n.a.}}\!\left(\begin{smallmatrix} \mathbf{q}\to\mathbf{0} \\ \kappa\;\kappa' \end{smallmatrix}\right) = \frac{e^2}{\varepsilon_0 V \sqrt{M_\kappa M_{\kappa'}}} \; \frac{\left(\mathbf{Z}_{\mathrm{B}}^{\mathrm{tr}}(\kappa)\cdot\vec{q}\right)_\alpha \left(\vec{q}\cdot\mathbf{Z}_{\mathrm{B}}(\kappa')\right)_\beta}{\vec{q}\cdot\boldsymbol{\varepsilon}_\infty\cdot\vec{q}} \; .
\tag{2.62}
$$

Equation (2.62) shows that all the information necessary to deal with the non-analytic part of the dynamical matrix is contained in the macroscopic dielectric constant $\boldsymbol{\varepsilon}_\infty$ of the system and in the Born effective charges $\mathbf{Z}_{\mathrm{B}}$. According to Eq. (2.59), the Born effective charge tensor of the κth atom equals the partial derivative of the macroscopic polarization with respect to a (long-wavelength) displacement of the κth atom at zero macroscopic field,

$$
\left(Z_{\mathrm{B}}(\kappa)\right)_{\alpha\beta} = \frac{V}{e} \left.\frac{\partial P_\alpha}{\partial u_\beta(\kappa)}\right|_{\mathbf{E}=\mathbf{0}} ,
\tag{2.63}
$$

whereas the tensor of the electronic dielectric constant equals the partial derivative of the macroscopic polarization with respect to the macroscopic electric field at zero atomic displacement:

$$
(\varepsilon_\infty)_{\alpha\beta} = \delta_{\alpha\beta} + \frac{1}{\varepsilon_0}\left.\frac{\partial P_\alpha}{\partial E_\beta}\right|_{\mathbf{u}=\mathbf{0}} .
\tag{2.64}
$$

The last two equations are used to calculate $\mathbf{Z}_{\mathrm{B}}(\kappa)$ and $\boldsymbol{\varepsilon}_\infty$ from first principles (see Sect. 2.4). In these calculations, no need arises to deal explicitly with the macroscopic electric field, therefore the periodic boundary conditions are not violated. Once these quantities are determined, the full dynamical matrix in the long-wavelength limit is set up according to Eqs. (2.57) and (2.62). Due to the non-analytic part, its diagonalization is possible only after choosing a specific direction $\vec{q}$. As result, one obtains the complete phonon spectrum (at the Γ point) corresponding to the chosen $\vec{q}$.

2.3.3.2 LO–TO Splitting and Static Dielectric Constant

The influence of the non-analytic part of the dynamical matrix is to modify the frequencies of those phonon modes exhibiting a nonzero dynamical dipole moment $\mathbf{p}$ [cf. Eq. (2.55)]. Such modes are termed infra-red (IR) active since according to Eq. (2.61) they can couple to the electric field. The latter equation also shows that the field is always directed along the propagation direction $\vec{q}$, and that modes with a dipole moment perpendicular to the propagation direction are not influenced by the field. The latter vibrations are called transverse optical (TO) modes. Correspondingly, vibrations with $\mathbf{p}$ along $\vec{q}$ are called longitudinal optical (LO) modes. Equation (2.61) shows that in order for the electric field to have an influence on the lattice vibrations, a longitudinal component in the mode polarization suffices. Therefore, the field does not only influence those modes that are LO modes in the strict sense explained above (which occur only for special directions that depend on the crystal symmetry) but also those having a polarization neither perpendicular nor parallel to $\mathbf{q}$. In general, the polarization direction of a mode is given

---

[15] Note the different treatment of the atomic masses in [*Ven75*; Eq. (4.141)]. Note further that in the literature, sometimes the transpose of $\mathbf{Z}_{\mathrm{B}}$ is used as "apparent charge" [*Coc62*]. This makes a difference since $\mathbf{Z}_{\mathrm{B}}$ is not symmetric.

by the direction of its atomic displacements, regardless whether or not its dipole moment is nonzero. For an IR-active mode, the polarization corresponds to its dynamical dipole moment.

The effect of the macroscopic electric field (or, equivalently, the non-analytic part of the dynamical matrix) can be seen from the generalized LO–TO splitting, given by the difference of the sum of all eigenvalues of the full dynamical matrix and of its regular part. This is obtained by taking the trace of the respective matrices: $\mathrm{trace}\big[\boldsymbol{\mathcal{D}}\big(\begin{smallmatrix}\mathbf{q}\to\mathbf{0}\\\kappa\,\kappa'\end{smallmatrix}\big) - \boldsymbol{\mathcal{D}}^{\mathrm{rg}}\big(\begin{smallmatrix}\mathbf{q}\to\mathbf{0}\\\kappa\,\kappa'\end{smallmatrix}\big)\big] = \mathrm{trace}\big[\boldsymbol{\mathcal{D}}^{\mathrm{n.a.}}\big(\begin{smallmatrix}\mathbf{q}\to\mathbf{0}\\\kappa\,\kappa'\end{smallmatrix}\big)\big]$. Since only the IR-active modes contribute to the difference, one has that

$$\sum_{j=1}^{r}\big[\omega_j^2(\vec{q}) - \omega_j^2(0)\big] = \frac{e^2}{\varepsilon_0 V}\sum_{\kappa}\frac{1}{M_\kappa}\frac{|\vec{q}\cdot\mathbf{Z}_{\mathrm{B}}(\kappa)|^2}{\vec{q}\cdot\boldsymbol{\varepsilon}_\infty\cdot\vec{q}}\,. \tag{2.65}$$

Here r is the number of IR-active modes, $\omega_j(\vec{q})$ is the frequency of a vibrational mode determined from the full dynamical matrix, Eq. (2.57), and $\omega_j(0)$ is a frequency determined from the regular part of the dynamical matrix only, where the electric field is explicitly excluded. The latter frequencies are known as the dielectric dispersion frequencies; they mark the poles of the dielectric function in the infrared spectral region. Since the macroscopic electric field is not involved, in this work we denote the corresponding vibrational modes as "purely mechanical." As can be seen from Eq. (2.65), in general, the LO–TO splitting may depend on the propagation direction $\vec{q}$. Usually, for uniaxial crystals this direction is expresssed by the angle $\theta(\vec{q}, c)$ between $\vec{q}$ and the crystal's c axis. In this work, the angular dependence of the phonon frequencies will be studied in detail for the superlattices, since it helps to identify different modes. In Sect. 3.2.3, an explicit expression for the LO–TO splitting in a wurtzite crystal is given.

Finally, the tensor components of the static dielectric constant, $\boldsymbol{\varepsilon}_{\mathrm{s}}$, are derived from a generalized [*Coc62*] Lyddane–Sachs–Teller (LST) relation, valid for any crystal symmetry [*Ven75*; Sect. 4.3.5]:

$$\frac{\displaystyle\prod_{j=1}^{r}\omega_j^2(\vec{q})}{\displaystyle\prod_{j=1}^{r}\omega_j^2(0)} = \frac{\vec{q}\cdot\boldsymbol{\varepsilon}_{\mathrm{s}}\cdot\vec{q}}{\vec{q}\cdot\boldsymbol{\varepsilon}_\infty\cdot\vec{q}}\,. \tag{2.66}$$

For crystals of orthorhombic symmetry or higher, a system of mutually perpendicular axes exist which allows to identify modes polarized along each of these axes. These modes can be further distinguished according to their propagation direction: Modes polarized in the α direction and propagating in the α direction are called longitudinal (L) modes, whereas modes polarized in the α direction but propagating in a direction $\beta \neq \alpha$ are called transverse (T) modes. The former ones are denoted as $\omega_{\mathrm{L},j}^{(\alpha)}$, the latter as $\omega_{\mathrm{T},j}^{(\alpha)}$. It follows from simple symmetry considerations that there are in each case $N_{\mathrm{b}} - 1$ modes fulfilling this condition. Moreover, for orthorhombic symmetry or higher, the static and high-frequency dielectric tensor are diagonal [*Ven75*; Table 4.2]. Based on these considerations, Cochran and Cowley gave an expression for the LST relation that connects these diagonal elements with *all* optic modes polarized in the corresponding direction [*Coc62*]:

$$\prod_{j=1}^{N_{\mathrm{b}}-1}\left(\frac{\omega_{\mathrm{L},j}^{(\alpha)}}{\omega_{\mathrm{T},j}^{(\alpha)}}\right)^2 = \frac{(\varepsilon_{\mathrm{s}})_{\alpha\alpha}}{(\varepsilon_\infty)_{\alpha\alpha}}\,. \tag{2.67}$$

Note again that here the L modes propagate along the α direction, whereas the T modes propagate in a perpendicular direction. In Sect. 3.2.3, an explicit expression is given for the LST relation for the case of wurtzite symmetry.

2.4   Density-Functional Perturbation Theory

Since phonon frequencies are obtained as eigenvalues of the dynamical matrix, the latter has to be calculated from first principles in order to obtain a full ab-initio description of a crystal. In the harmonic approximation, the dynamical matrix is directly related to the atomic force constants of second order, Eqs. (2.41) and (2.48). Considering the Hellmann-Feynman theorem for the frozen-lattice Hamiltonian, Eq. (2.4), it follows that the desired force constants can be obtained from the linear response of the electron density. Therefore, in principle, one has to apply first-order perturbation theory to the DFT. The general theory is elaborated in [*Bar01*]. As perturbations, atomic displacements as well as a macroscopic electric field have to be taken into account in order to determine both the regular and the singular (i. e., the analytic and non-analytic) part of the dynamical matrix.

The self-consistent Kohn–Sham scheme can be extended to explicitly calculate the linear response of the electrons. The basic steps proceed as follows. Let $^{(0)}V^{\text{ext}}$ be the unperturbed external potential and $^{(1)}V^{\text{ext}}$ the first-order perturbation, to which the system responds by a change of the electron density from its unperturbed distribution $^{(0)}n$ (supposed to be known) to $(^{(0)}n + {}^{(1)}n)$. From Eq. (2.21) one can see that the KS potential will change accordingly and will act back on the density, and so forth until self-consistency. Explicitly, the perturbation terms have to be calculated from the following set of equations [*Kar93*, *Ple98*]:

$$^{(1)}E_i^{\text{KS}} = \left\langle {}^{(0)}\varphi_i \,\middle|\, {}^{(1)}V^{\text{KS}\,(0)}\varphi_i \right\rangle, \tag{2.68a}$$

$$\left(-\frac{\hbar^2}{2m}\nabla_{\mathbf{r}}^2 + {}^{(0)}V^{\text{KS}} - {}^{(0)}E_i^{\text{KS}} \right) {}^{(1)}\varphi_i(\mathbf{r}) = -\left({}^{(1)}V^{\text{KS}} - {}^{(1)}E_i^{\text{KS}} \right) {}^{(0)}\varphi_i(\mathbf{r}), \tag{2.68b}$$

$$^{(0)}V^{\text{KS}}(\mathbf{r}) = V_{[^{(0)}n,\,^{(0)}V^{\text{ext}}]}^{\text{KS}}(\mathbf{r}), \tag{2.68c}$$

$$^{(1)}V^{\text{KS}}(\mathbf{r}) = {}^{(1)}V^{\text{ext}}(\mathbf{r}) + V_{[^{(1)}n]}^{\text{H}} + {}^{(1)}n(\mathbf{r}) \left. \frac{\delta V_{[n]}^{\text{XC}}(\mathbf{r})}{\delta n} \right|_{n = {}^{(0)}n}, \tag{2.68d}$$

$$^{(1)}n(\mathbf{r}) = \sum_i \left({}^{(0)}\varphi_i^*(\mathbf{r})\, {}^{(1)}\varphi_i(\mathbf{r}) + {}^{(1)}\varphi_i^*(\mathbf{r})\, {}^{(0)}\varphi_i(\mathbf{r}) \right). \tag{2.68e}$$

Additional terms arise if a pseudopotential is used that includes the NLCC, since then also in the calculation of the XC energy the actual position of the corresponding atom has to be taken into account [*Dal93*]. In principle, the numerical effort to solve this system of equations is comparable to that needed for solving the unperturbed KS equation. However, to obtain all necessary data, several different perturbations have to be treated, their number scaling (to leading order) as N_{b}^2. Therefore, the practical application of the DFPT method is limited to a rather small number of basis atoms — unless ultrasoft non-normconserving pseudopotentials are used which enormously reduce the numerical effort; the corresponding modification of DFPT is outlined in [*Bar01*].

The dynamical matrix is calculated in the following way [*Pav91*, *Bar01*]. According to Eq. (2.8), its regular (analytic) part has an ionic and an electronic contribution, $\boldsymbol{\mathcal{D}}^{\mathrm{rg}} = \boldsymbol{\mathcal{D}}^{\mathrm{ion}} + \boldsymbol{\mathcal{D}}^{\mathrm{el}}$. The ionic contribution stems from the second derivative of the Ewald energy and can be calculated analytically. The electronic contribution is calculated from the following expression (the factor 2 accounts for spin degeneracy):

$$
\mathcal{D}_{\alpha\beta}^{\mathrm{el}}\left(\substack{\mathbf{q} \\ \kappa\kappa'}\right) = \frac{2}{N_{\mathrm{c}}} \frac{\delta_{\kappa\kappa'}}{M_\kappa} \sum_{\nu\mathbf{k}} \langle {}^{(0)}\varphi_{\nu\mathbf{k}} \mid \frac{\partial^2 V^{\mathrm{ext}}}{\partial u_\alpha^*\left(\substack{\mathbf{q} \\ \kappa}\right)\partial u_\beta\left(\substack{\mathbf{q} \\ \kappa}\right)} {}^{(0)}\varphi_{\nu\mathbf{k}}\rangle
$$
$$
+ \frac{2}{N_{\mathrm{c}}} \frac{1}{\sqrt{M_\kappa M_{\kappa'}}} \left(\sum_{\nu\mathbf{k}} \langle \frac{\partial\varphi_{\nu\mathbf{k}}}{\partial u_\alpha\left(\substack{\mathbf{q} \\ \kappa}\right)} \mid \frac{\partial V^{\mathrm{ext}}}{\partial u_\beta\left(\substack{\mathbf{q} \\ \kappa'}\right)} {}^{(0)}\varphi_{\nu\mathbf{k}}\rangle + \mathrm{c.\,c.} \right)
$$

(2.69)

where N_{c} is the number of primitive cells in the considered periodicity volume and $\partial\varphi_{\nu\mathbf{k}}/\partial u_\alpha\left(\substack{\mathbf{q} \\ \kappa}\right)$ is the first-order perturbed KS orbital ${}^{(1)}\varphi_i$ for the case of a "monochromatic" perturbation given by $\mathbf{u}\left(\substack{l \\ \kappa}\right) = \mathbf{u}\left(\substack{\mathbf{q} \\ \kappa}\right)e^{i\mathbf{q}\cdot\mathbf{R}(l)}$, cf. Eq. (2.46). For the singular (non-analytic) part of the dynamical matrix, Eq. (2.62), the tensors of the electronic dielectric constant and of the Born effective charge are needed. They are obtained as follows [*Pav91*, *Gia91*]. The total macroscopic polarization, Eq. (2.59), is — in a microscopic sense — composed of a purely ionic term, $\mathbf{P}^{\mathrm{ion}} = \frac{e}{V} \sum_\kappa Z_\kappa^{\mathrm{val}}\mathbf{u}(\kappa)$, with the number of valence electrons Z_κ^{val} contributed by the κth atom, and an electronic term, which encompasses both the (static) dielectric screening (present for clamped ions) and the dynamical effects that cause $\mathbf{Z}_{\mathrm{B}}(\kappa)$ to differ from Z_κ^{val}. For spin degeneracy, the electronic polarization can be written as $\mathbf{P}^{\mathrm{el}} = \frac{4}{N_{\mathrm{c}}V} \sum_{\nu\mathbf{k}} \langle {}^{(0)}\varphi_{\nu\mathbf{k}} \mid \mathbf{r}\,{}^{(1)}\varphi_{\nu\mathbf{k}}\rangle$, cf. [*Kar93*]. The perturbation in this case can be either a lattice vibration (as above) or an electric field; the latter is discussed below. According to Eq. (2.63) one has for the tensor of the Born effective charge:

$$
\left(Z_{\mathrm{B}}(\kappa)\right)_{\alpha\beta} = Z_\kappa^{\mathrm{val}}\delta_{\alpha\beta} + \frac{V}{e} \frac{\partial P_\alpha^{\mathrm{el}}}{\partial u_\beta(\kappa)} = Z_\kappa^{\mathrm{val}}\delta_{\alpha\beta} + \frac{4}{eN_{\mathrm{c}}} \sum_{\nu\mathbf{k}} \langle {}^{(0)}\varphi_{\nu\mathbf{k}} \mid r_\alpha \frac{\partial\varphi_{\nu\mathbf{k}}}{\partial u_\beta(\kappa)}\rangle. \qquad (2.70)
$$

According to Eq. (2.64), the dielectric tensor is given by

$$
(\varepsilon_\infty)_{\alpha\beta} = \delta_{\alpha\beta} + \frac{1}{\varepsilon_0} \frac{\partial P_\alpha^{\mathrm{el}}}{\partial E_\beta}\bigg|_{\mathbf{u}=\mathbf{0}} = \delta_{\alpha\beta} + \frac{4}{\varepsilon_0 N_{\mathrm{c}}V} \sum_{\nu\mathbf{k}} \langle {}^{(0)}\varphi_{\nu\mathbf{k}} \mid r_\alpha \frac{\partial\varphi_{\nu\mathbf{k}}}{\partial E_\beta}\rangle. \qquad (2.71)
$$

Here, $\partial\varphi_{\nu\mathbf{k}}/E_\beta$ is the linear response caused by an electric field. It is determined from the following set of equations [*Kar93*]:

$$
\left(-\frac{\hbar^2}{2m}\nabla_{\mathbf{r}}^2 + {}^{(0)}V^{\mathrm{KS}} - {}^{(0)}E_i^{\mathrm{KS}}\right) \frac{\partial\varphi_{\nu\mathbf{k}}}{\partial E_\beta} = -\frac{\partial V^{\mathrm{KS}}}{\partial E_\beta} {}^{(0)}\varphi_{\nu\kappa}(\mathbf{r}), \qquad (2.72\mathrm{a})
$$

$$
\frac{\partial V^{\mathrm{KS}}(\mathbf{r})}{\partial E_\beta} = -r_\beta + \int \frac{\partial n(\mathbf{r}')/\partial E_\beta}{|\mathbf{r}-\mathbf{r}'|}\,\mathrm{d}\mathbf{r}' + \frac{\partial n(\mathbf{r})}{\partial E_\beta} \frac{\mathrm{d}V_{[n]}^{\mathrm{XC}}(\mathbf{r})}{\mathrm{d}n}\bigg|_{n={}^{(0)}n}, \qquad (2.72\mathrm{b})
$$

$$
\frac{\partial n(\mathbf{r})}{\partial E_\beta} = 2 \sum_{\nu\kappa} {}^{(0)}\varphi_{\nu\kappa}^*(\mathbf{r}) \frac{\partial\varphi_{\nu\mathbf{k}}}{\partial E_\beta}(\mathbf{r}). \qquad (2.72\mathrm{c})
$$

Some care has to be taken when dealing with the matrix elements of the position operator in a system with periodic boundary conditions; this problem is discussed (and solved) in [*Gia91*].

2.5   Frozen-Phonon Calculations

In a frozen-phonon calculation, the frequency of a specific vibration is determined from the change in total energy that occurs when the atoms are displaced according to the phonon mode under consideration. This requires the knowledge of the respective eigenvector, which for some modes can be obtained from symmetry considerations and group-theoretic methods. This technique, using DFT-LDA calculations, was first applied to silicon [*Wen78*, *Yin80*]. It has the advantage that it is not restricted to harmonic effects. However, for arbitrary $\mathbf{q}$ one has to use a supercell of dimension $2\pi/|\mathbf{q}|$ in order to accommodate a full period of the lattice wave. Moreover, due to the macroscopic electric field associated with LO(Γ) modes, the latter cannot be calculated in this direct manner. Instead, one has to calculate the dynamical effective charge and apply Eq. (2.65) to determine the LO frequency from the TO one. The effective charge can be obtained from a supercell calculation, as was demonstrated for GaAs [*Kun81*]. In this work, using the frozen-phonon method we will study only TO modes and non-polar vibrations.

In general terms [i. e., ignoring the technical subtleties previously indicated by a tilde (LDA) and a ring (Coulomb singularity removed) as well as suppressing the arguments], the total energy of the interacting system of (valence) electrons and (classical) ion cores is given by the following contributions [cf. Sect. 2.2.6, Eqs. (2.38) and (2.39)]:

$$E^{\text{tot}} = E^{\text{Ew}} + E^{\text{bs}} - E^{\text{H}} + E^{\Delta\text{XC}}. \tag{2.73}$$

Let $\mathbf{y}$ be the (formal) vector whose components are the (one-dimensional) displacements y_κ of the basis atoms from their equilibrium position when they oscillate according to a (Γ-point) phonon mode (i. e., the number of components of $\mathbf{y}$ equals the number of basis atoms.). The frozen-phonon energy $E_{\text{ph}}^{\cdots}$ that corresponds to each of the above total-energy contributions (i. e., "$\cdots$" stands either for "tot," "Ew," "bs," "H," or "ΔXC") is obtained as the difference of the respective energy relative to its equilibrium value,

$$E_{\text{ph}}^{\cdots}(\mathbf{y}) := E^{\cdots}|_{\mathbf{y}} - E^{\cdots}|_{\mathbf{y}=\mathbf{0}}. \tag{2.74}$$

From the total energy, the phonon frequency is obtained using the following harmonic fit function [*Sri90*; Eq. (3.48)]:

$$E_{\text{fit}}(\mathbf{y}) = \frac{1}{2}\omega^2 \sum_\kappa M_\kappa y_\kappa^2, \tag{2.75}$$

where the sum runs over all basis atoms. The actual displacements y_κ of the atoms with masses M_κ are chosen according to the total displacement $\eta = |\mathbf{y}|$ and the corresponding components of the normalized mode eigenvector $\mathbf{e}$ (which we take from the DFPT calculation) as $y_\kappa = e_\kappa \eta$, so that

$$E_{\text{fit}}(\eta) = \frac{1}{2}\omega^2 \left(\sum_\kappa M_\kappa e_\kappa^2 \right) \eta^2, \tag{2.76}$$

which allows to determine the frequency ω from plotting the total energy vs the total displacement η. Provided that the harmonic approximation is appropriate, this frequency should be (nearly) identical to the one resulting from the DFPT calculation.

The purpose of the frozen-phonon calculation is the following: Equation (2.76) shows that by referring to η the results obtained for different materials and different lattice constants (i. e., varying under the influence of pressure or stress) can be compared with each other. This not only holds for the frozen-phonon total energy itself but also for its contributions [cf. Eqs. (2.73) and (2.74)], which can be plotted in exactly the same way. Thereby, an interpretation of the observed frequency shifts is possible, since one can study in detail the influence of the different contributions to the total energy. In this way, the frozen-phonon calculation provides information not accessible by a DFPT calculation. On the other hand, only a DFPT calculation can provide an exact eigenvector: Even if the crystal symmetry does not change if the lattice constant is varied, the eigenvector may change, but this cannot be obtained from a symmetry consideration alone.

## 2.6 Modeling of Strains and Stresses

Under the influence of external forces, electric fields or due to a change in temperature, a solid undergoes a deformation. These effects are known, respectively, as purely mechanical behavior (which can be classified as [visco]elastic or [visco]plastic [*Hau00*]), converse piezoelectric effect and thermal expansion. The mechanical and piezoelectric properties are treated explicitly by ab-initio calculations. For an externally imposed deformation, the structural response of the lattice is obtained by minimizing the total energy with respect to the remaining degrees of freedom of the ionic positions. This will be described in detail in Sects. 3.1 and 4.1. The results thereby obtained are interpreted by assuming an ideal linear elastic behavior, taking into account the (converse) piezoelectric effect as will be discussed below. As discussed before, the ab-initio calculations employed being valid only for $T = 0$ K imply that thermal effects are completely neglected.

Experimentally, a given external stress results in a macroscopic strain. In the calculations, however, the atomic positions are chosen first, and the accompanying forces are obtained numerically. Therefore, unless a strain is given in the experimental situation, each stress case has to be modeled by appropriate strains. This will be described in the following. However, as a general classification, the different situations are identified according to the (symmetry of the) stress present in each case.

2.6.1 Strained Bulk Crystal Structures

In this work, homogeneously strained wurtzite (space group: C_{6v}^4) and zinc-blende (space group T_d^2) crystals are investigated that exhibit no shear deformation. Three different physical situations are envisaged giving rise to such a homogeneous strain: (i) hydrostatic pressure, (ii) lattice misfit in pseudomorphic growth on a substrate or of a superlattice, and (iii) uniaxially applied stress. Additionally, in case (ii) a biaxial stress may arise due to thermal misfit if the growth takes place at high temperatures.

As long as no phase transitions occur, hydrostatic pressure preserves the symmetry of a crystal structure. For wurtzite, the stresses of (ii) and (iii) lead to symmetry-conserving strains if the basal plane is stressed isotropically or if uniaxial stress is present along the symmetry axis,
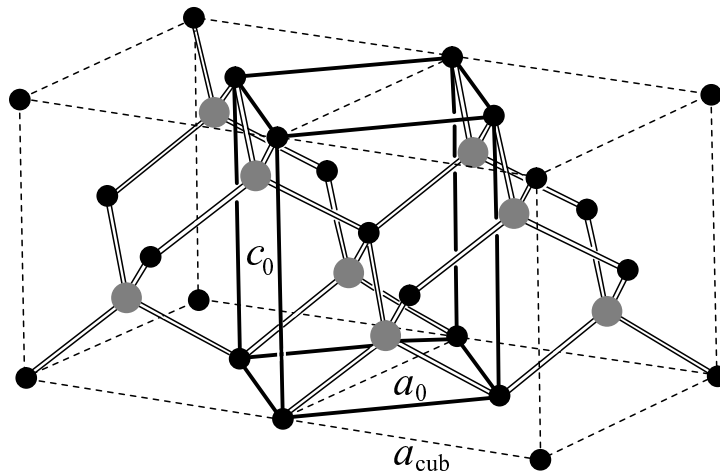
Figure 2.1 Schematic representation of the tetragonal unit cell (thick solid lines) and its lattice constants in the zinc-blende crystal structure.

[0001]. For zinc-blende materials, isotropic biaxial stress in a plane perpendicular to or unixial stress along one of the cubic axes ([001], say) leads to a tetragonal unit cell and the point-group symmetry is reduced from T_d (class $\overline{4}3m$) to D_{2d} (class $\overline{4}2m$).

From a macroscopic point of view, for these specific situations both the resulting strained cubic (i.e., tetragonal) and wurtzite structures are transversely isotropic and, therefore, with respect to their elastic properties, can be treated on equal footing. In fact, as long as no shear strains are involved, the elastic properties of hexagonal and tetragonal crystals are characterized by elastic compliance (and stiffness) matrices having the same form with respect to nonvanishing as well as equal-valued elements [*Nye85*]. For both kinds of structures, the symmetry axis is taken as the z axis and one always has to distinguish between the c lattice constant along this axis and the one in the xy plane, a. The equilibrium tetragonal lattice constants are related to the cubic one as $a_0 = a_{cub}/\sqrt{2}$ and $c_0 = a_{cub}$ (see Fig. 2.1).

In this work, a uniaxial stress will be considered that preserves the transversely isotropic elasticity. It is described by a diagonal stress tensor $\boldsymbol{\sigma} = \mathrm{diag}(0, 0, \sigma_{\parallel})$ and modeled by a certain strain of the c lattice constant, which is given by $\epsilon_{zz} = (c - c_0)/c_0$ and, only for this special case of uniaxial stress, labeled as uniaxial strain $\epsilon_{\parallel}$. Correspondingly, isotropic biaxial stress in the basal plane is given by $\boldsymbol{\sigma} = \mathrm{diag}(\sigma_{\perp}, \sigma_{\perp}, 0)$ and modeled by a strain of the a lattice constant, $\epsilon_{xx} = (a - a_0)/a_0$, which for this special case of isotropic biaxial stress is labeled as biaxial strain $\epsilon_{\perp}$.

2.6.2 Pyroelectricity, Piezoelectricity and Macroscopic Elasticity

Since a polar lattice that lacks inversion symmetry is piezoelectric, both the wurtzite and zinc-blende phase of the nitrides exhibit piezoelectricity. Due to its symmetry, there is no spontaneous polarization in the zinc-blende structure and for the tetragonal distortion discussed above, no piezoelectric polarization is created. On the other hand, the wurtzite structure exhibits a spontaneous polarization (pyroelectricity) and the strength of the polarization changes with strain. Therefore, one has to take pyroelectric and piezoelectric effects into account when

relating stress and strain of the wurtzite structure. To linear order, this relation is given by Hooke's law, which here is written as to contain the converse piezoelectric effect:

$$\sigma_{xx} = (C_{11} + C_{12})\epsilon_{xx} + C_{13}\epsilon_{zz} - e_{31}E_z, \tag{2.77a}$$

$$\sigma_{zz} = 2C_{13}\epsilon_{xx} + C_{33}\epsilon_{zz} - e_{33}E_z. \tag{2.77b}$$

Here and in the following, isothermal elastic constants C_{ij} are assumed and the Voigt notation (for abbreviated tensor indices) is also used for the isothermal piezoelectric constants e_{31} and e_{33}. The electric field inside the crystal is supposed to have only a z component, E_z (corresponding to the nonvanishing component of the spontaneous and/or piezoelectric polarization), since any field component in the xy plane would give rise to shear stress.

However, for an unstrained bulk crystal the pyroelectric effects can be completely neglected in Eq. (2.77) if the electric field is suppressed because of a screening due to surface charges. In the ab-initio calculation of a bulk crystal, the electric field is suppressed due to periodic boundary conditions. Then, one may use Eq. (2.77) without the terms containing the piezoelectric constants, which is done in the following. Moreover, this also holds for strained bulk crystals and crystalline layers. The corrections of the elastic properties are negligible studying atomic positions [*Gle01, Bec02b*].

As discussed in the previous section, both the tetragonally strained cubic and the wurtzite structure are transversely isotropic and can be treated on equal footing. Since in this work, elasticity theory is merely used to interpret the ab-initio results in the linear regime around equilibrium, from the tetragonally strained cubic structures only the cubic elastic constants can be obtained. Due to the higher symmetry of the cubic structure, there are more equal-valued elements in the corresponding stiffness matrix than in a stiffness matrix of a wurtzite or a tetragonal crystal. Therefore, as the results for the cubic structure can be obtained as a special case (i. e., exhibiting some degeneracies) of uniaxial symmetry (such as wurtzite), in the following subsections the equations are first given for wurtzite symmetry with a subsequent specialization of the final results for (tetragonally strained) cubic symmetry.

2.6.2.1 Wurtzite Symmetry

Without taking into account pyroelectric and piezoelectric effects, Hooke's law reads

$$\sigma_{xx} = (C_{11} + C_{12})\epsilon_{xx} + C_{13}\epsilon_{zz}, \tag{2.78a}$$

$$\sigma_{zz} = 2C_{13}\epsilon_{xx} + C_{33}\epsilon_{zz}. \tag{2.78b}$$

For a uniaxial stress $\sigma_{zz} = \sigma_\parallel \neq 0$ along the z axis (i. e., in the direction of the c lattice constant), $\sigma_{xx} = \sigma_{yy} = 0$ holds and Eq. (2.78a) leads to the relation

$$\epsilon_{xx} = -\nu_c\epsilon_{zz} \ (= -\nu_c\epsilon_\parallel) \tag{2.79}$$

between the strain components, with the coefficient

$$\nu_c = \frac{C_{13}}{C_{11} + C_{12}} \tag{2.80}$$

being the Poisson ratio for this case. By definition, the uniaxial stress is linearly related to the strain along the direction of the stress by the Young modulus (elasticity modulus) E, which obviously is direction-dependent. Here, this reads

$$\sigma_{\parallel} = E_c \epsilon_{\parallel} \tag{2.81}$$

and the Young modulus in the c-axis direction is given by

$$E_c = C_{33} - \frac{2C_{13}^2}{C_{11} + C_{12}} = C_{33} - 2\nu_c C_{13}. \tag{2.82}$$

The last expression permits an intuitive physical interpretation: The stress in the c-axis direction is proportional to the axial stiffness but is weakened by the relaxation that takes place in the two perpendicular directions.

   An isotropic biaxial stress $\sigma_{\perp}$ in the xy plane implies vanishing forces along the c axis, $\sigma_{zz} = 0$. Then, Eq. (2.78b) gives the relation

$$\epsilon_{zz} = -R_c^{\mathrm{b}} \epsilon_{xx} \ (= -R_c^{\mathrm{b}} \epsilon_{\perp}), \tag{2.83}$$

with the biaxial relaxation coefficient of the c lattice constant,

$$R_c^{\mathrm{b}} = 2\frac{C_{13}}{C_{33}}. \tag{2.84}$$

For transversely isotropic crystals, the isotropic biaxial stress is linearly related to the homogeneous biaxial (i. e., in-plane) strain by the biaxial modulus Y. Here this reads

$$\sigma_{\perp} = Y_c \epsilon_{\perp} \tag{2.85}$$

and the biaxial modulus for the plane perpendicular to the c axis follows as

$$Y_c = C_{11} + C_{12} - \frac{2C_{13}^2}{C_{33}} = C_{11} + C_{12} - R_c^{\mathrm{b}} C_{13}. \tag{2.86}$$

Also here, an intuitive physical interpretation is possible: The in-plane stress is proportional to the sum $C_{11} + C_{12}$ expressing the in-plane stiffness and is weakened by the relaxation taking place in c-axis direction.

   The Young modulus E_c is related to the biaxial modulus Y_c according to

$$E_c = \frac{C_{33} Y_c}{C_{11} + C_{12}} = \frac{2\nu_c}{R_c^{\mathrm{b}}} Y_c. \tag{2.87}$$

This allows to express the biaxial stress, Eq. (2.85), in terms of the c-axis strain, Eq. (2.83), as

$$\sigma_{\perp} = -\frac{Y_c}{R_c^{\mathrm{b}}} \epsilon_{zz} = -\frac{E_c}{2\nu_c} \epsilon_{zz}. \tag{2.88}$$

The last equation is generally known to hold for cubic and elastically isotropic media [*Nye85*]. Nevertheless, it is not restricted to that case, since here it also holds for wurtzite symmetry due to the special strain cases under consideration. It has to be emphasized that, although the

coefficient $E_c/(2\nu_c)$ on the right-hand side of Eq. (2.88) is made up of quantities that refer to the case of uniaxial stress, this equation describes (and is only valid for) the case of biaxial stress.

For given hydrostatic pressure p the diagonal components of the stress tensor are equal, $\sigma_{xx} = \sigma_{yy} = \sigma_{zz} = -p$, and from Hooke's law, Eqs. (2.78), it follows that

$$\epsilon_{zz} = R_c^{\mathrm{h}}\epsilon_{xx}, \tag{2.89}$$

with the hydrostatic relaxation coefficient of the c lattice constant,

$$R_c^{\mathrm{h}} = \frac{C_{11} + C_{12} - 2C_{13}}{C_{33} - C_{13}}. \tag{2.90}$$

To linear order, the bulk modulus B_0 relates the change in volume $\Delta V = V - V_0$ (where V_0 is the equilibrium volume) to the pressure variation Δp (around $p = 0$ GPa) according to

$$\frac{\Delta V}{V_0} = -\frac{\Delta p}{B_0}. \tag{2.91}$$

The fractional volume variation is given by $\Delta V/V_0 = 2\epsilon_{xx} + \epsilon_{zz}$, which for hydrostatic pressure leads to the relation

$$(2 + R_c^{\mathrm{h}})\epsilon_{xx} = -\frac{\Delta p}{B_0}. \tag{2.92}$$

From Eqs. (2.89), (2.90) and either (2.78a) or (2.78b) (with $\sigma_{\alpha\alpha} = -\Delta p$) another relation between ϵ_{xx} and Δp can be obtained and be used to substitute ϵ_{xx} in Eq. (2.92), leading to an expression for the bulk modulus in terms of the elastic stiffness constants:

$$B_0 = \frac{(C_{11} + C_{12})C_{33} - 2C_{13}^2}{C_{11} + C_{12} + 2C_{33} - 4C_{13}}. \tag{2.93}$$

Since it follows from Eqs. (2.93) and (2.86) that, respectively,

$$Y_c = \left[2 + (\nu_c^{-1} - 4)R_c^{\mathrm{b}}/2\right] B_0 \quad \text{and} \tag{2.94}$$

$$C_{13} = Y_c/(\nu_c^{-1} - R_c^{\mathrm{b}}), \tag{2.95}$$

the values of the elastic stiffness constants[16] can be determined as a by-product of the relaxation calculation if the ab-initio results are interpreted in terms of linear elasticity theory as described above.

2.6.2.2 Cubic Symmetry

To distinguish between wurtzite and zinc-blende elastic stiffness constants, lower-case characters are used for the latter. The relations obtained above for wurtzite symmetry can be specialized to (tetragonally strained) cubic symmetry if the following substitutions are made: C_{11} and C_{33} are replaced by c_{11}, whereas C_{12} and C_{13} are replaced by c_{12}. It has to be noticed, however, that these substitutions are *not* related to a transformation of the stiffness constants

---

[16] Due to the (unchanged) wurtzite symmetry, only the value of the sum $C_{11} + C_{12}$ can be obtained.

of a zinc-blende material into wurtzite symmetry, which is also known as Martin's transfomation [*Mar72*]. Instead, here only the analogy between both (strained) crystal symmetries is used which is given by the transversally isotropic elasticity.

For cubic crystals that are subjected to a (small) tetragonal deformation as described above (where $\epsilon_{xx} = \epsilon_{yy}$ and $\sigma_{xx} = \sigma_{yy}$), no piezoelectric polarization occurs, and the relations between stress and strain (i. e., Hooke's law) read

$$\sigma_{xx} = (c_{11} + c_{12})\epsilon_{xx} + c_{12}\epsilon_{zz}, \tag{2.96a}$$

$$\sigma_{zz} = c_{11}\epsilon_{zz} + 2c_{12}\epsilon_{xx}. \tag{2.96b}$$

The Poisson ratio and the Young modulus for a uniaxial stress along the direction of the c lattice constant are given by

$$\nu_c = \frac{c_{12}}{c_{11} + c_{12}} \quad \text{and} \tag{2.97}$$

$$E_c = c_{11} - \frac{2c_{12}^2}{c_{11} + c_{12}} = c_{11} - 2\nu_c c_{12}. \tag{2.98}$$

The biaxial relaxation coefficient of the c lattice constant and the (corresponding) biaxial modulus read

$$R_c^{\mathrm{b}} = \frac{2c_{12}}{c_{11}} \quad \text{and} \tag{2.99}$$

$$Y_c = c_{11} + c_{12} - \frac{2c_{12}^2}{c_{11}} = c_{11} + c_{12} - R_c^{\mathrm{b}}c_{12}. \tag{2.100}$$

As for the wurtzite structure, the latter are related to the Young modulus and the Poisson ratio according to $E_c = c_{11}Y_c/(c_{11} + c_{12}) = 2\nu_c Y_c/R_c^{\mathrm{b}}$, which implies that, as already mentioned, also for the (tetragonally strained) cubic structure the biaxial stress can be expressed in terms of the c-axis strain by Eq. (2.88).

Additionally, since $c_{11}/(c_{11} + c_{12}) = 1 - \nu_c$, one has that

$$E_c = (1 - \nu_c)Y_c \quad \text{and} \tag{2.101}$$

$$R_c^{\mathrm{b}} = \frac{2\nu_c}{1 - \nu_c}. \tag{2.102}$$

The last equation is equivalent to

$$\nu_c = \frac{R_c^{\mathrm{b}}}{2 + R_c^{\mathrm{b}}}. \tag{2.103}$$

Equations (2.102) and (2.103) only hold for cubic crystals and elastically isotropic media; due to their symmetry, the Poisson ratio and the biaxial relaxation coefficient are not independent.

As it must be, for the hydrostatic relaxation coefficient one has $R_c^{\mathrm{h}} \equiv 1$. The bulk modulus is related to the elastic stiffness constants according to

$$B_0 = \frac{1}{3}(c_{11} + 2c_{12}). \tag{2.104}$$

It holds that $E_c = 3(1 - 2\nu_c)B_0$. The values of the elastic constants can be determined from

$$c_{11} = 3B_0(\nu_c^{-1} - 2)/(\nu_c^{-1} - R_c^{\mathrm{b}}) \quad \text{and} \tag{2.105}$$

$$c_{12} = c_{11}R_c^{\mathrm{b}}/2. \tag{2.106}$$

2.6.3 Elastic Energy of a Strained Hexagonal Superlattice

A superlattice of alternating layers of two materials having slightly different in-plane lattice constants is considered. Each layer heigth h_i is assumed to be smaller than the critical thickness of material $i = 1, 2$ so that the superlattice layers are formed coherently on top of each other. If no substrate is present, the common in-plane lattice constant a_{SL} is determined by the elastic properties of the layers. An expression for this lattice constant in terms of the elastic constants is known for cubic materials and arbitrary stacking direction [*Ana91*]. In the following, based on linear elasticity theory, it shall be determined for a superlattice composed of hexagonal layers stacked in [0001] direction.

In the absence of shear strains, the density of the elastic energy of material i is given by (using Voigt notation for the indices)

$$u^{(i)} = \frac{1}{2} \sum_{\alpha=1}^{3} \sigma_\alpha^{(i)} \epsilon_\alpha^{(i)}. \tag{2.107}$$

Since here one has that $\sigma_{zz}^{(i)} = 0$, $\sigma_{xx}^{(i)} = \sigma_{yy}^{(i)}$, $\epsilon_{xx}^{(i)} = \epsilon_{yy}^{(i)}$, and $\sigma_{xx}^{(i)} = Y_c^{(i)} \epsilon_{xx}^{(i)}$, this reduces to

$$u^{(i)} = Y_c^{(i)} \epsilon_{xx}^{(i)2}. \tag{2.108}$$

To lowest order in the strain, the elastic energy of a column with base area of a hexagonal cell is given by multiplying Eq. (2.108) with the volume of the unstrained column. Neglecting the change in heigth of each layer due to elastic relaxation, this is taken approximately as $V_i = \frac{\sqrt{3}}{2} a_0^{(i)2} h_i$, thereby cancelling the normalizing factor $a_0^{(i)}$ in the strain. The elastic energy of a column extending over two adjacent layers having the same in-plane lattice constant a_{SL} therefore is

$$U = \frac{\sqrt{3}}{2} \sum_{i=1}^{2} h_i Y_c^{(i)} \left(a_{\mathrm{SL}} - a_0^{(i)}\right)^2. \tag{2.109}$$

For elastic relaxation, a_{SL} is determined by the minimum of U, which follows from

$$0 = \sum_{i=1}^{2} h_i Y_c^{(i)} \left(a_{\mathrm{SL}} - a_0^{(i)}\right) \tag{2.110}$$

as

$$a_{\mathrm{SL}} = \frac{\sum_{i=1}^{2} h_i Y_c^{(i)} a_0^{(i)}}{\sum_{i=1}^{2} h_i Y_c^{(i)}}, \tag{2.111}$$

i. e., an expression very similar to the one long since known for the case of cubic layers stacked in [001] direction [*Mat77*]. Here, however, in place of the shear moduli $G^{(i)}$, the biaxial moduli $Y_c^{(i)}$ appear.

2.7   Strain- and Stress-Related Phonon Frequency Shifts

In general, the phonon frequencies of a strained wurtzite isotropic crystal are shifted or splitted with respect to the strain-free values. In the linear strain limit these shifts and splittings are related to the strain tensor, ϵ, by

$$\Delta\omega(A_1) = a(A_1)(\epsilon_{xx} + \epsilon_{yy}) + b(A_1)\epsilon_{zz}, \tag{2.112a}$$

$$\Delta\omega(E_{1/2}) = a(E_{1/2})(\epsilon_{xx} + \epsilon_{yy}) + b(E_{1,2})\epsilon_{zz}$$
$$\pm c(E_{1/2})\sqrt{(\epsilon_{xx} - \epsilon_{yy})^2 + 4\epsilon_{xy}^2} \tag{2.112b}$$

in dependence on the mode symmetry $j = A_1$ or $E_{1/2}$. The non-Raman-active B_1 modes follow a similar relation as the A_1 modes. The same relations hold for tetragonally-strained cubic crystals. Due to the lowering of the symmetry, one has to distinguish between modes polarized along the tetragonal axis and those polarized in the perpendicular direction. The former ones possess B_2 symmetry and they follow Eq. (2.112a), whereas the latter ones have E symmtry and they follow Eq. (2.112b).

The coefficients $a(j)$, $b(j)$, and $c(j)$ are the corresponding phonon deformation potentials per unit strain. Since here we are considering symmetry-conserving strains, the tensor ϵ is diagonal and only the deformation potentials $a(j)$ and $b(j)$ are involved. The latter ones are determined directly from the ab-initio calculations by the following "artificial" deformation. While keeping one lattice constant fixed at its equilibrium value, the other one is slightly strained, and the internal parameter u is determined from energy minimization. For this artificial strain state, the phonon frequencies are calculated, and the differences to the ground-state values immediately give the respective deformation potentials as linear coefficients.

For the considered cases of biaxial and uniaxial strain, where the diagonal elements of the strain tensor, ϵ_{xx} and ϵ_{zz}, are related to each other by the ratios R_c^b (biaxial strain) or ν_c (uniaxial strain), one can introduce new deformation potentials $K_{\perp/\parallel}(j)$ which relate the linear frequency shift directly to the given biaxial strain, $\epsilon_\perp$, or uniaxial strain, $\epsilon_\parallel$. The shift is written as

$$\Delta\omega(j) = K_{\perp/\parallel}(j)\epsilon_{\perp/\parallel}. \tag{2.113}$$

The strain coefficients, $K_{\perp/\parallel}(j)$, are related to the deformation potentials by $K_\perp(j) = 2a(j) - R_c^b b(j)$ and $K_\parallel(j) = -2\nu_c a(j) + b(j)$. However, the values of the strain coefficients are directly determined from the calculated phonon frequency shifts under biaxial and uniaxial strain, respectively. Furthermore, using the respective stress-strain relation the frequency shifts (2.113) can be related to the corresponding uniaxial, $\sigma_\parallel$, or biaxial, $\sigma_\perp$, stress parameter. Thereby, in the linear stress limit one obtains the coefficients $\widetilde{K}_{\perp/\parallel}(j)$ giving the frequency change per unit stress as $\widetilde{K}_\perp(j) = K_\perp(j)/Y_c$ and $\widetilde{K}_\parallel(j) = K_\parallel(j)/E_c$.

Chapter 3

Ground-State Determination and Properties of Unstrained Polytypes

In this work, to determine the equilibrium structural parameters for GaN and AlN both in the hexagonal wurtzite (2*H*) as well as in the cubic zinc-blende (3*C*) structure, total-energy calculations for *fixed atomic positions* are performed. For the 2*H* structure, this requires a deliberate relaxation procedure. Also, careful considerations of numerical influences on the results and of the accuracy requirements are given before convergency tests and structural, dielectric, and vibrational properties are presented and discussed.

3.1   Relaxation Procedure for the 3*C* and 2*H* Structures

The structural ground-state properties are obtained from the universal equation-of-state (EOS) by Vinet and coworkers [*Vin86*]. The explicit expression for the volume dependence of the total energy, $E^{\text{tot}}(V)$, is fitted to calculated values at different volumes V_j of the primitive cell, $E_j = E^{\text{tot}}(V_j)$. For 3*C* there is only one structural parameter, the lattice constant $a_{\text{cub}} = \sqrt[3]{4V}$, and the EOS can also be determined as $E^{\text{tot}}(a_{\text{cub}})$. On the contrary, for 2*H* there are three parameters: a, c (lattice constants) and u (internal parameter); hence for a given volume V_j firstly one has to determine the ratio c/a and the value of u before the corresponding E^{tot} can be obtained. In order to handle these calculations correctly, the following has to be considered:

The internal parameter u always adjusts itself for given "external parameters" a, c (or $V, c/a$) according to a minimization of the total energy (internal relaxation), leading to either $u(a, c)$ or $u(V, c/a)$. Therefore, the total energy macroscopically accessible is a function of only two parameters, $E^{\text{tot}}(a, c)$ or $E^{\text{tot}}(V, c/a)$, resp., in contrast to the numerically available result $E_{\text{calc}}(a, c, u)$ which renders the total energy also for atomic positions that are not physically realized. It holds that $E^{\text{tot}}(a, c) = \min_u E_{\text{calc}}(a, c, u) = E_{\text{calc}}(a, c, u(a, c))$.

If only the volume is fixed by external conditions, also the ratio c/a adjusts itself by energy minimization. This results in a considerable expense for the relaxation of the 2*H* structure by means of total-energy calculations for fixed atomic positions: In order to minimize E^{tot} at a given volume V_j with respect to the lattice constants, it has to be calculated for a set of suitable values of c/a. For each of these, the corresponding internal parameter u has to be determined

first. This results in an "optimized" $(c/a)_j$ and, finally, the value of $u_j = u(V_j, (c/a)_j)$ has to be calculated.

In this work, the total-energy minimizations are handled using polynomial fits. With a set of five different u and seven values for c/a this amounts to 40 total-energy calculations and nine fits[1] *for each volume V_j*, in contrast to just one calculation for the $3C$ structure. The EOS is fitted to results calculated at 5 (8) different volumes for the $2H$ ($3C$) structure. For $3C$, the EOS already yields the final result. For $2H$, on the other hand, it only gives the ground-state volume, thus one still has to determine the appropriate c/a and u values.

For $2H$, the number of seven c/a values is found to be necessary in order to obtain the desired accuracy for the structural parameters. A simplification of the $2H$ relaxation would be to firstly determine just one u_0 (at one c/a), which is kept fixed for all c/a, and then determine a new one for the final c/a. However, neither is it clear at which c/a this u_0 should be determined, nor is there a justification for this procedure, which would have to be based on arguments that the lattice parameters vary slowly — instead, their behavior is *a priori* unknown. Such a simplified procedure cannot be expected to yield more than a rough estimate.

The main task of this work is to determine the influence of various types of stress (as, e. g., hydrostatic pressure) on the lattice parameters; all other properties are calculated for the resulting strained structures. Due to the nitrides' hardness it can be expected that changes in the lattice constants are rather small. Therefore, the wurtzite structure needs to be calculated most precisely, and it is not reasonable to use the simplified relaxation procedure. Moreover, the accuracy of the final results is given by the convergency of the *differences* of the lattice parameters and of the physical properties with respect to the deformation. To resolve typical structural changes of the order of one hundredth of the lattice parameters to a precision of a few percent, the lattice parameters themselves have to be determined to a precision of 10^{-4} (which indeed can be achieved using the polynomial fits; see below). As a consequence, these accuracy requirements have to be taken into account already for the ground-state calculations.

However, a technical problem arises for the fitting: In order to numerically solve the Kohn-Sham (KS) equation using plane waves one has to introduce a kinetic cutoff energy E_{cut}. At a given volume V of the primitive cell, E_{cut} determines the number N_{pw} of plane waves forming the basis for the expansion of the KS wavefunction. It holds that $N_{\text{pw}} \sim V(E_{\text{cut}})^{3/2}$. This leads to a possible numerical influence on the calculated results when the volume is varied, since the calculations can be performed with either constant E_{cut} or constant N_{pw}. For the determination of the equilibrium volume it was shown that using a constant E_{cut} leads to a result which is closer to the fully converged one than when using a constant N_{pw} [*Gom86*]. The arguments given in the latter work indicate that this not only holds for the determination of the equilibrium volume but for non-hydrostatic deformations as well. Therefore, in general it is be difficult to accurately find the total-energy minimum, since for calculations performed with constant E_{cut}, the total energy shows systematic discontinuities when the lattice parameters are varied due to changes of N_{pw} [*Gom86*]. These systematic fluctuations are most pronounced in the region of the minimum of E^{tot}.

In order to overcome the problem of the discontinuities while maintaining the benefit of better convergence when using $E_{\text{cut}} = \text{const}$, one can fit the resulting variation of total energy

---

[1] $5 \times 7 + 5$ calculations for the final u determination; seven fits to obtain the u's for the chosen c/a, one for optimizing c/a, and one for optimizing the final u.

using appropriate functions. Then, the desired result is obtained as the minimum of the fitting function. For the determination of the equation of state, this function is an analytical EOS, and the atoms are shifted as to simulate hydrostatic pressure. Now, general cases of structural relaxation shall be considered where, by changing the atomic arrangement, discontinuities in the variation of total energy occur due to varying numbers of plane waves. Then, other functions (e. g., polynomials) are used for fitting, which for not too complicated structures also allow for systematically treating internal degrees of freedom [*Zia03*].

In general, this deserves two comments. First, the fitting itself can be questionable since one is not dealing with data that exhibit stochastical noise but systematic variations due to the described effect of varying N_{pw}. Therefore, a systematic deviation from the true result can occur in the fitting. However, if the amplitude of these systematic variations is sufficiently small, also the systematic error of the fitting is small. By increasing the cutoff energy and/or the number of special **k** points, the necessary accuracy can, in principle, be reached. This means that, as usual, careful convergency tests have to be made.

Second, mostly it is not clear what to choose as an "appropriate fitting function," since the total-energy variation depends (at least) on the atomic species involved and on the deformation studied. Obviously, the correctness of the result — i. e., to end up neiher with an artificial nor (in case it existst) a satellite total-energy minimum but with the true one — depends on the choice of both the sampling of the atomic positions and the function used for fitting. However, in case that the equilibrium positions can be roughly determined, it suffices to perform only small shifts of the atoms about these positions, so that the total energy might exhibit a nearly symmetric behavior, which can be fitted rather precisely.

The accuracy of the result, then, depends on the quality of the fit: The smaller the deviations of the fitted curve from the calculated data, the less the uncertainty in the position of the minimum. Therefore, a smoother total-energy curve allows a better fit. This leads to the same requirement as does the need to avoid systematic errors involved in the fitting, since a smoother total-energy curve is obtained for higher E_{cut} and/or larger **k**-point set. On the other hand, this means that the quality of the fit might serve as sign for the degree of convergency reached — at least in the (negative) sense as to indicate that it can still be improved.

It has to be noticed that the requirement of a sufficiently smooth total-energy curve also applies to the calculation of the c/a ratio of the $2H$ structure. Even though in this case the volume does not change, the total energy shows some fluctuations since the *shape* of the Brillouin zone changes as c/a varies and, therefore, different sets of plane waves contribute in the total-energy expansion. The consequences for the nitrides will be discussed in section 3.2.1.2.

3.2 Convergency Tests and Discussion of Results

3.2.1 Structural Properties

3.2.1.1 Zinc-Blende Phase

For cubic AlN and GaN, the Vinet EOS is used to determine E^{tot}, a_{cub}, B_0, and B_0' from calculations using sets of 5 and 8 sampling points (lattice constants), meshes of 10, 19, 28, and 44 Chadi-Cohen **k**-points, and varying cutoff energy. The variation of the results with these

Table 3.1 Ground-state structural properties of AlN and GaN in zinc-blende phase: lattice constant a_{cub} (Å), bulk modulus B_0 (GPa) and its pressure derivative B_0' at zero pressure, as well as the total-energy difference per cation-N pair between the $3C$ and the $2H$ structure $\Delta E^{\text{tot}} = E^{\text{tot}}(3C) - E^{\text{tot}}(2H)$ (meV). Where available, experimental values are given for comparison [*PGN94*; except noticed otherwise].

		a_{cub}	B_0	B_0'	ΔE^{tot}
$3C$-AlN	calc.	4.334	210.2	3.5	+48.2
	exper.	4.38	$(202)^{\text{a,b}}$		—
$3C$-GaN	calc.	4.443	206.5	4.0	+20.2
	exper.	4.49–4.55	$(185)^{\text{a}}$		—

[a] estimated from transformed wurtzite elastic constants
[b] [*She91*]

numerical parameters shows that, independent of the number of special **k**-points, at least a cutoff energy of 70 Ry is required for converged results. The structural parameters are already converged while the total energy is not; converging the latter requires $E_{\text{cut}} \geqq 85$ Ry. Then, independent of the number of special **k**-points, the same value of E^{tot} is obtained. Furthermore, for $E_{\text{cut}} \geqq 70$ Ry the results are practically independent of the numer of sampling points (5 or 8). For lower cutoff energies, this holds only for larger **k**-point sets, however, these conforming results do not equal the ones obtained for higher cutoff energy. Therefore, obtaining identical fits of the EOS to different numbers of sampling points is only a necessary criterion for convergency (with respect to E_{cut}), not a sufficient one.

The results given in Table 3.1 are obtained for $E_{\text{cut}} = 75$ Ry and 19 Chadi-Cohen points for $3C$-AlN (28 points for $3C$-GaN). In comparison with the experimental data, the calculated lattice constants are approximately 1 % (2 %) smaller, which is due to the enhanced bonding caused by the LDA.

Comparing the lattice constants of different cubic nitrides one sees that AlN has a slightly smaller one. On the other hand, it has a slightly higher bulk modulus. This corresponds to a trend which is to be expected due to the ionic radii of the constituent atoms. Nevertheless, the nitrogen atom dominates the bonding properties in both cases. This manifests itself in the nearly equal and rather high value of the charge-asymmetry coefficient g as defined by Garcia and Cohen [*Gar93a*], which is $g = 0.794$ for $3C$-AlN and $g = 0.780$ for $3C$-GaN.

3.2.1.2 Wurtzite Phase

For hexagonal nitrides one has to determine not only the ground-state volume but also the inner geometry as given by c/a and u. This requires a separate convergency test for these parameters at a fixed volume, V_0. Here, an equilibrium volume was used that was determined in a preparatory work based on a cutoff energy of $E_{\text{cut}} = 50$ Ry. With respect to the accuracy requirements of the present work, it is found that the internal parameter u is nearly converged using this cutoff, but c/a is not. For a converged result of the latter, at least $E_{\text{cut}} = 75$ Ry

Table 3.2 Convergence of the ratio of the lattice constants, c/a, of 2H-AlN and -GaN with respect to the numerical cutoff energy, E_{cut} (in Ry).

E_{cut}	2H-AlN	2H-GaN
50	$1.597,5 \pm 0.001,5$	(no result)
60	$1.597,4 \pm 0.000,4$	$1.624,5 \pm 0.000,8$
70	$1.598,43 \pm 0.000,19$	$1.625,02 \pm 0.000,08$
75	$1.598,27 \pm 0.000,04$	$1.625,16 \pm 0.000,05$
80	$1.598,28 \pm 0.000,09$	$1.625,16 \pm 0.000,04$

is required; cf. Table 3.2. In the case of $E_{cut} = 50$ Ry the discontinuities of E^{tot} caused by varying N_{pw} inhibited the fitting for GaN. Only if the cutoff energy is chosen large enough, the fit becomes smooth and allows to determine c/a with sufficient accuracy. The computational difference in determining c/a and u is that a variation of u alone does not change the plane-wave basis, since c/a is kept fixed. Therefore a lower cutoff energy is sufficient for the determination of u.

More in detail, the c/a data given in Table 3.2 are obtained as follows: For the least-squares fits based on Chebyshev-series representations of the polynomial approximations of various degrees,[2] seven c/a sampling points are used. In order to take into account the influence of the particular choice of these sampling points, several fits are performed, either using all of these points or using only six of them, leaving either the first or the last one aside. Altogether, this provides 10 different results. Since the fluctuations of the total energy curve being due to varying N_{pw}, they represent a systematic error and are not due to a stochastic noise, thus a statistical treatment of these results (mean average and standard deviation) does not yield a "final result" but merely an indication about the spreading of the different fits. Comparing both the mean averages and the standard deviations for different cutoff energies helps to follow the convergence. It is with these restrictions in mind that we show the statistically treated data in Table 3.2. As the final result of the fitting, we take the c/a value of the fit that comes closest to the original data, i. e., whose fit curve shows the least deviation from the calculated energies. It was observed that in nearly all cases this result was found inside the tolerance interval determined by the statistical treatment.

Always, 12 Chadi-Cohen points have been used as special **k**-point set. The influence of the choice of the number of these points has been tested for 2H-GaN. It was found that u does not change when using 24 **k**-points instead, and c/a varies less than 3×10^{-5}, which is not a relevant amount. Since the calculational effort for the wurtzite structure is much higher than for the zinc-blende one, extensive convergency tests are abstained from. Instead, based on the results of the fits for c/a calculated at five different volumes (with $E_{cut} = 75$ Ry), the EOS is fitted to total energies directly calculated for these structures using $E_{cut} = 70, 75,$ and 80 Ry.[3] The

---

[2] Explicitly, the NAG routines E02ADF and E02AKF are used.

[3] Here, the calculation using $E_{cut} = 75$ Ry is necessary since the total energy of the resulting structure is needed. From the fits for c/a one reliably obtains only the position of the minimum of E^{tot} with respect to c/a, but not the corresponding value of E^{tot} itself.

Table 3.3 Ground-state structural properties of AlN and GaN in wurtzite phase: lattice constant a (Å), ratio c/a, internal parameter u, and bulk modulus B_0 (GPa) as well as its pressure derivative B_0' at zero pressure. Experimental values are given for comparison [*PGN94*; except noticed otherwise].

		a	c/a	u	B_0	B_0'
2*H*-AlN	calc.	3.084	1.5983	0.3825	210.0	3.6
	exper.	3.110–3.113	1.600–1.602	0.3821[a]	208[b]	6.3[b]
2*H*-GaN	calc.	3.145	1.6252	0.3775	205.7	4.3
	exper.	3.1892	1.6258		245	4
		3.168–3.187[c]	1.625–1.628[c]	0.377[a]	188–245[d–f]	3.2–4.3[d–f]
		3.188[g]	1.6264[g]		202.4[h]	4.5[h]

[a] [*Sch77*]	[c] [*Lag79*]	[e] [*Sav78*]	[g] [*Les96*]
[b] [*Uen92*]	[d] [*Xia93*]	[f] [*Per92*]	[h] [*Tsu02*]

resulting ground-state volume is practically identical in all cases; it shows a relative uncertainty of $\Delta V/V = 3 \times 10^{-5}$, which is better than the accuracy desired. In this work, $E_{\text{cut}} = 75$ Ry is used for determining c/a and $E_{\text{cut}} = 60$ Ry for calculating u.

The results are presented in Table 3.3. As for the cubic nitrides, the calculated lattice constants are about 1 % smaller than the experimental ones. However, for 2*H*-GaN c/a is only 0.04 % smaller than found experimentally (0.17 % for 2*H*-AlN), which is a very good result. Unfortunately, the experimental value of the internal parameter u of GaN ist not known with sufficient accuracy, so that the deviation is 0.13 % (0.10 % for AlN). The lattice parameters c/a and u of GaN are rather close to the ones of the ideal wurtzite structure, $(c/a)_{\text{id}} = \sqrt{8/3} \approx 1.633$ and $u_{\text{id}} = 3/8 = 0.375$, whereas AlN shows significant deviations from these.

These comparisons show that the results obtained for GaN using the NLCC (in order to partially account for the influence of the Ga $3d$ electrons) are of the same quality as those obtained for AlN, where there are no d electrons. This shows — at least for the properties studied here — that the NLCC is a successful approach.

3.2.1.3 Relative Phase Stability

As can be seen from Fig. 3.1, for both nitrides the total energy (per cation–N pair) of the wurtzite phase is lower than that of the cubic phase. This is consistent with the experimental finding that the wurtzite structure is the equilibrium one for AlN and GaN at ambient conditions. However, the growth of the metastable zinc-blende polytype has also been achieved. For energetical comparison, all calculations are performed using $E_{\text{cut}} = 75$ Ry and different numbers of special **k**-points. Here, convergency is reached if the energy difference $\Delta E^{\text{tot}}(3C-2H)$ does not change anymore when increasing the set of special **k**-points.

According to Lawaetz, a general trend can be observed [*Law72*]: Due to differences in the ionicity, the stability of the wurtzite lattice in comparison to zinc blende is closely related to deviations of the c/a ratio from the ideal value. For a stable wurtzite structure, $c/a \lesssim 1.633$ is found, and the energetical difference to the zinc-blende structure is larger for a material with a
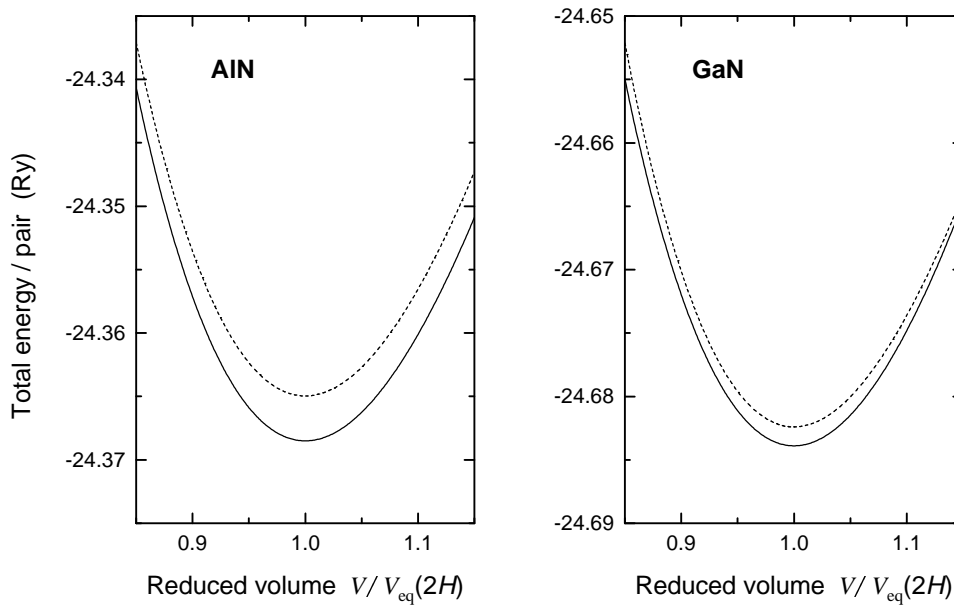
Figure 3.1 Comparison of total energies between the $3C$ (dotted line) and the $2H$ (solid line) phase of AlN and GaN (per cation–N pair).

larger deviation. Here, this trend is found to be fulfilled for the nitrides; cf. Table 3.3 for their values of c/a.

3.2.2 Electronic Dielectric Constant and Born Effective Charge

To determine quantities derived from perturbation theory one only needs to know the lattice parameters. To obtain a converged result of a DFPT calculation, it is not necessary to choose the same cutoff energy and **k**-point set as for the determination of the structural properties, since E_{cut} and **k** points are only numerical tools for the calculation of the physical properties of interest. Therefore, once the lattice geometry has been determined, for calculating the electronic dielectric constant, the Born effective charge, and the phonon frequencies — all of which are obtained from the same DFPT calculation —, a separate convergency test has to be made. The physical property which is most sensitive to the numerical parameters will determine the computational requirements.

For the cubic nitrides, ε_∞ and Z_B are found to be converged using $E_{cut} = 50$ Ry and 10 Chadi-Cohen points for AlN (28 for GaN). For the hexagonal nitrides, one has to distinguish between the xx and the zz component of the respective tensors. Due to the screw-axis symmetry and the charge neutrality condition, for the four atoms forming the basis of the wurtzite structure there is only one independent tensor Z_B. Here, the difference between as well as the ordering of the xx and zz tensor components are important. To reach convergency $E_{cut} = 60$ Ry and 12 Chadi-Cohen points have to be used for both AlN and GaN. In Table 3.4 the results obtained are given and compared with experimental data. In general, there is good agreement among the data. Most important, the ordering of the magnitude of the tensor components is determined

Table 3.4 Dielectric properties of unstrained AlN and GaN: electronic dielectric constant ε_∞, Born effective charge Z_B of the cation (in units of the elementary charge e), and screened Born charge $Z_B^* = Z_B/\sqrt{\varepsilon_\infty}$ for the zinc-blende as well as respective tensor components $(\varepsilon_\infty)_{xx}$, $(\varepsilon_\infty)_{zz}$, $(Z_B)_{xx}$, $(Z_B)_{zz}$, $(Z_B^*)_{xx} = (Z_B)_{xx}/\sqrt{(\varepsilon_\infty)_{xx}}$, and $(Z_B^*)_{zz} = (Z_B)_{zz}/\sqrt{(\varepsilon_\infty)_{zz}}$ for the wurtzite structure. Experimental values are given for comparison.

		ε_∞	Z_B	Z_B^*	$(\varepsilon_\infty)_{xx}$	$(\varepsilon_\infty)_{zz}$	$(Z_B)_{xx}$	$(Z_B)_{zz}$	$(Z_B^*)_{xx}$	$(Z_B^*)_{zz}$
AlN	calc.	4.46	2.56	1.21	4.30	4.52	2.54	2.70	1.23	1.27
	exper.	(4.4)[a]	—	—	(4.68)[b]		(2.57)[c]			
					4.4[d]	4.8[d]				
GaN	calc.	5.40	2.65	1.14	5.20	5.39	2.60	2.74	1.14	1.18
	exper.	—	—	—	(5.29)[e]		2.65[f]	2.82[f]		
					5.2[g], 5.14[h]	5.31[h]				

[a] *[Tho01]*, estimated from refractive-index measurement on 3*C*-AlN

[b] *[Aka67]*, from IR reflection on polycrystalline sample

[c] *[San83]*, no symmetry-related difference mentioned

[d] *[Pik81]*

[e] *[Azu95]*, assuming $(\varepsilon_\infty)_{xx} = (\varepsilon_\infty)_{zz}$ [g] *[Ejd71]*

[f] *[Bar73]*   [h] *[Yu97]*

correctly. Also, the quality of the results (compared to the experimental data) is similar for GaN and AlN. Therefore, here the NLCC proves to be a successful approximation as well.

3.2.3 Phonons and Static Dielectric Constant

3.2.3.1 Zinc-Blende Phase

For the cubic nitrides, the phonon frequencies at the center of the Brillouin zone (Γ point) are given in Table 3.5, in comparison to experimental data. The static dielectric constant is derived from the electronic dielectric constant and the phonon frequencies, using the Lyddane-Sachs-Teller (LST) relation $\varepsilon_s/\varepsilon_\infty = \omega_{LO}^2/\omega_{TO}^2$. The agreement of the calculated results with the experimental data is rather good, the phonon frequencies are overestimated by about 1 %. Compared to other III-V semiconductors, the phonon frequencies are rather large. This is due to both the small nitrogen mass and, as a consequence of the shorter bond length, the larger force constants. Also, the static dielectric constants are rather large, especially when compared to the electronic ones. The ratio $\varepsilon_s/\varepsilon_\infty$ shows values of 1.88 (1.79) for 3*C*-AlN (3*C*-GaN). This is, of course, related to the same physical origin as is the large LO–TO splitting, which is the high ionicity established by a high density of polarizable atomic bonds. This can be seen as follows: For cubic materials, the LO–TO splitting is given by

$$\omega_{LO}^2 - \omega_{TO}^2 = \frac{e^2 Z_B^2}{\varepsilon_0 \varepsilon_\infty V \mu} \,, \tag{3.1}$$

Table 3.5 Phonons and static dielectric constant of unstrained AlN and GaN in zinc-blende phase: Zone-center TO and LO frequencies (cm^{-1}), the LO–TO splitting (cm^{-1}), and the (resulting) static dielectric constant ε_s. Experimental values are given for comparison.

		TO	LO	LO–TO	ε_s
3C-AlN	calc.	662	907	245	8.37
	exper.[a]	655	902	247	
3C-GaN	calc.	560	750	190	9.69
	exper.[b]	553	743	190	

[a] cf. [*Har99*] [b] cf. [*Goñ01*]

where μ is the reduced mass of a cation-nitrogen pair and V is the volume of the primitive cell.[4] Obviously, the LST relation then becomes

$$\frac{\varepsilon_s}{\varepsilon_\infty} = 1 + \frac{\omega_{LO}^2 - \omega_{TO}^2}{\omega_{TO}^2} = 1 + \frac{e^2 Z_B^2}{\varepsilon_0 \varepsilon_\infty V \mu \omega_{TO}^2} \ . \tag{3.2}$$

As for the zone-boundary modes, in Table 3.6 the values of the L- and X-point frequencies are given. The former ones are related to the additional modes found in the wurtzite structure (see the following subsection). The latter ones are of interest in conjuction with the cubic [001] superlattices (cf. Sect. 5.2).

Table 3.6 Phonons of unstrained AlN and GaN in zinc-blende phase: Frequencies of zone-boundary modes at the L and X points (cm^{-1}).

		TA(L)	LA(L)	TO(L)	LO(L)	TA(X)	LA(X)	TO(X)	LO(X)
3C-AlN	calc.	139	345	584	720	195	353	627	708
3C-GaN	calc.	230	583	656	750	340	590	674	734

3.2.3.2 Wurtzite Phase

In comparison to zinc-blende materials, for phonons in wurtzite-structure compounds two important differences occur: (i) Due to the approximately doubled elementary cell, the Brillouin zone is nearly half in size, with the branches at the (former) L point being folded back to the Γ point, because the cubic [111] direction corresponds to the hexagonal [0001] one. Therefore, four additional phonon modes occur. The former longitudinal ones become (nondegenerate) B_1 modes and the former transversal ones become (twofold degenerate) E_2 modes. (ii) Due to the axial symmetry-related anisotropy of the wurtzite lattice, the "original" Γ-point TO and LO eigenmodes are split according to the symmetry of their vibrational pattern, which can be of A_1

---

[4] This also explains why the LO–TO splitting is larger for AlN than for GaN: the screening, the cell volume, and the reduced mass are all smaller in AlN.
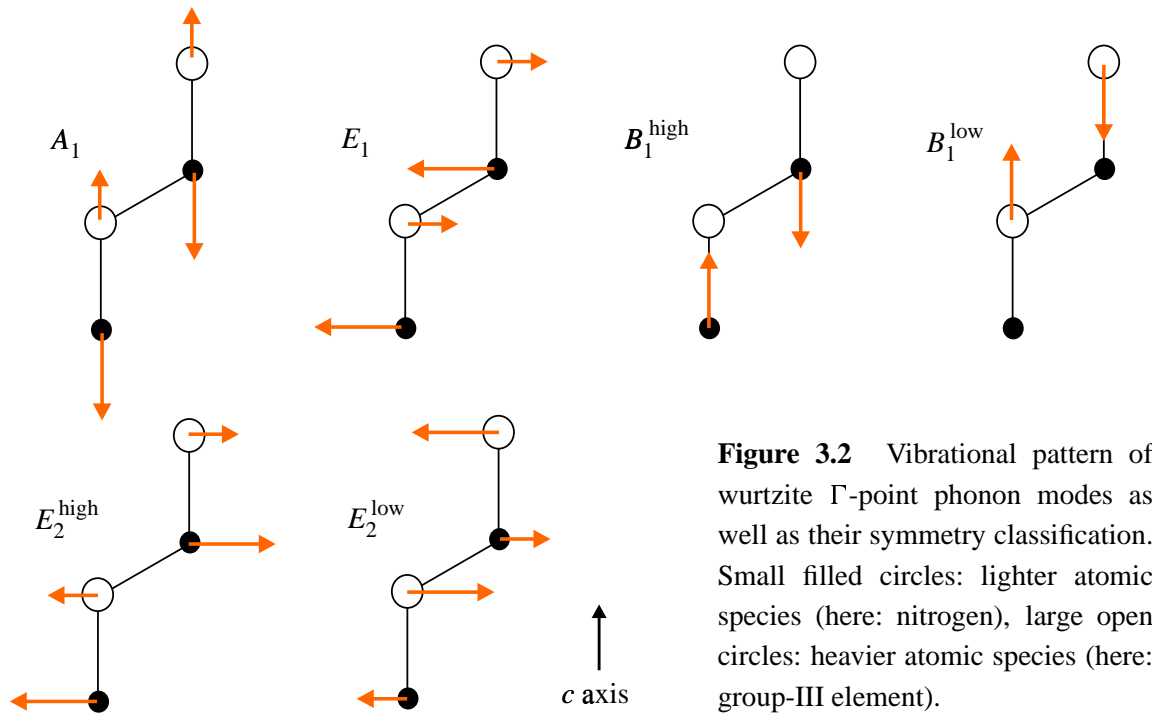
Figure 3.2 Vibrational pattern of wurtzite Γ-point phonon modes as well as their symmetry classification. Small filled circles: lighter atomic species (here: nitrogen), large open circles: heavier atomic species (here: group-III element).

Table 3.7 Phonons of unstrained AlN and GaN in wurtzite phase: Zone-center mode frequencies (cm^{-1}). Experimental data are given for comparison.

		E_2^{low}	B_1^{low}	A_1(TO)	E_1(TO)	E_2^{high}	B_1^{high}	A_1(LO)	E_1(LO)
2H-AlN	calc.	241	552	618	677	667	738	898	924
	exper.[a]	248		609	669	656		891	910
2H-GaN	calc.	142	337	540	568	576	712	748	757
	exper.[a]	144		532	558	567		734	742
	exper.[b]	144		533	561	569		735	743

[a] [Goñ01]   [b] [Azu95]

or E_1 type (cf. Fig. 3.2). The results are given in Table 3.7. The frequencies of the B_1 modes depend sensitively on the numerical parameters and, therefore, indicate the degree of convergency. Within the accuracy reached here, the phonon frequencies are converged to $\pm 1\,cm^{-1}$.

Only the A_1 and E_1 modes are both IR and Raman active, since the dipole moments associated with the displacements of anion-cation pairs do not cancel each other. However, this cancellation occurs for the B_1 and E_2 modes due to the symmetry of their vibrational pattern (cf. Fig. 3.2). Therefore, the latter modes do not interact with macroscopic electric fields. Moreover, due to the fractionary translation of the nonsymmorphic space group C_{6v}^4, for each of the B_1 modes the displacements of the two atoms moving are equivalent in the following sense: The "upward" movement of an atom along the c axis is undistinguishable from the "downward" movement of the same atom that occurs half an oscillation period later. Therefore, these modes do not contribute to first-order Raman scattering.
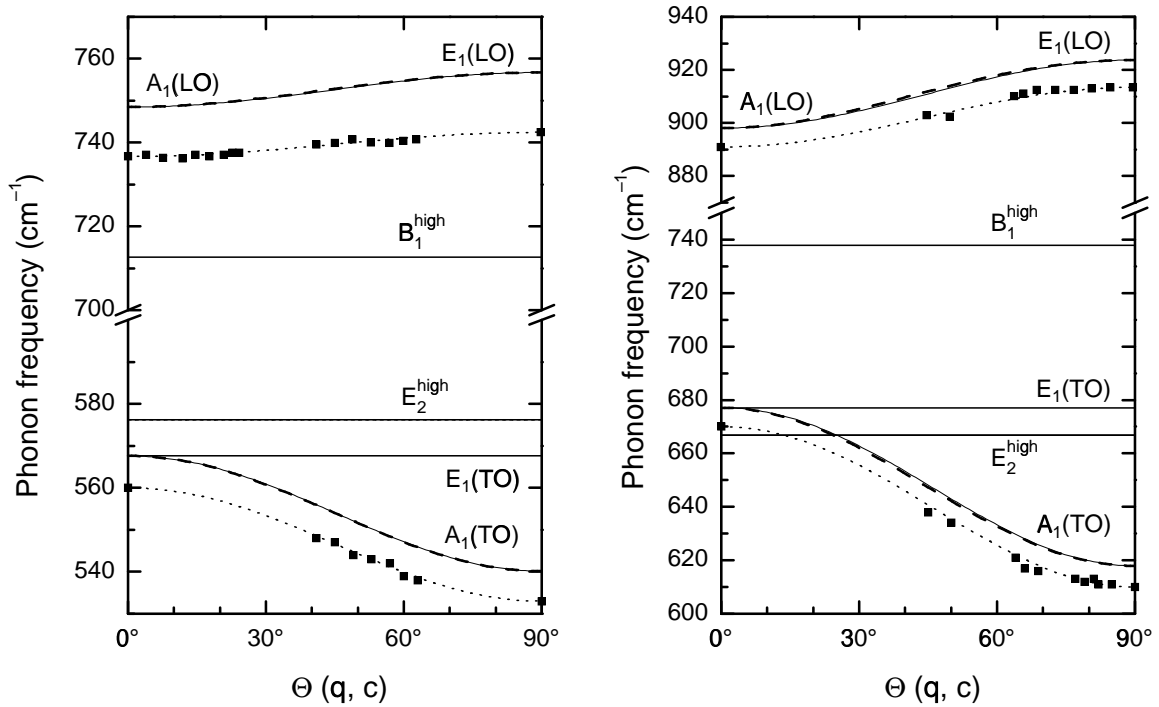
Figure 3.3 Angular dependence of calculated optical modes of 2*H*-GaN (left panel) and 2*H*-AlN (right panel). Θ is the angle between the phonon propagation direction $\vec{q}$ and the c axis. The angular-dependent modes are plotted as dashed lines. Also shown are experimental values (squares) for comparison [*Fil96*, *Sie98*]. The approximation according to [*Lou63*] is applied both to the calculated and measured data, and it is shown as thin and as dotted line, respectively.

The limiting cases of the angular dependence of the phonon frequencies shown in Fig. 3.3 can be understood as follows. For propagation parallel to the c axis, the A_1 mode obviously is an LO phonon and the E_1 mode is a (twofold degenerate) TO phonon. For propagation perpendicular to the c axis, the A_1 mode and one of the E_1 modes are TO phonons, whereas the second E_1 mode is an LO phonon. In an intermediate direction, the macroscopic electric field produces a mixing of the IR-active modes, resulting in so-called quasi-LO and quasi-TO modes having neither a distinct symmetry nor a proper polarization. Their frequency depends on the angle between the phonon propagation direction and the c axis. The nonpolar B_1 and E_2 modes as well as the E_1(TO) phonon do not depend on the propagation direction.

Since the respective longitudinal and transversal A_1 and E_1 mode frequencies are relatively close to each other, according to Loudon it can be expected that the angular variation of the (quasi-) LO and TO modes can be described by simple trigonometric functions [*Lou63*]. As can be seen from Fig. 3.3, this approximation works very well, both for the calculated and the measured data.

Similar to the cubic crystals, the ionicity of the wurtzite structure reveals itself in the splitting of the LO and TO modes. Because of the uniaxial crystal symmetry, one has to take into

Table 3.8 LO–TO splittings of zone-center phonons of the same symmetry, ΔA_1 and ΔE_1 (cm^{-1}), tensor components of the static dielectric constant, $(\varepsilon_s)_{xx}$ and $(\varepsilon_s)_{zz}$, as well as angle-averaged values for the TO and LO frequencies, $\omega_{\overline{TO}}$ and $\omega_{\overline{LO}}$ (cm^{-1}), for AlN and GaN in wurtzite phase. Experimental data are given for comparison.

		ΔA_1	ΔE_1	$(\varepsilon_s)_{xx}$	$(\varepsilon_s)_{zz}$	$\omega_{\overline{TO}}$	$\omega_{\overline{LO}}$
2H-AlN	calc.	280	247	8.16	9.73	658	915
	exper.[a]	282	241	8.14[b]	10.27[b]	650	904
	exper.[c]			7.98	9.18		
2H-GaN	calc.	208	189	9.24	10.36	559	754
	exper.[a]	202	184	9.09[d]	10.11[d]	549	739
	exper.[e]	202	182	9.02[d]	10.10[d]	552	740
	exper.[f]			9.5	10.4		

[a] [*Goñ01*] [d] using $\boldsymbol{\varepsilon}_\infty$ from [*Yu97*]

[b] using $\boldsymbol{\varepsilon}_\infty$ from [*Pik81*] [e] [*Azu95*]

[c] [*Mal97*] [f] [*Bar73*]

account the different mode symmetries. From Eq. (2.65) it follows that for the corresponding displacement directions holds ($\alpha = x, z$)

$$\omega_{LO}^2(\alpha) - \omega_{TO}^2(\alpha) = \frac{2e^2(Z_B)_{\alpha\alpha}^2}{\varepsilon_0(\varepsilon_\infty)_{\alpha\alpha}V\mu}, \tag{3.3}$$

with μ and V as above [Eq. (3.1)]. The values of the LO–TO splittings are rather sensitive to the numerical parameters used in the calculations; they are given in Table 3.8.

For the wurtzite nitrides, the tensor components of the static dielectric constant are derived from a generalized LST relation (cf. Sect. 2.3.3.2). From Eq. (2.67) it follows that for the relation beweeen the xx (zz) components of the dielectric tensors one has to use the frequency values of the E_1 (A_1) modes (indicated here according to the respective elongation direction α of the vibration, cf. Fig. 3.2):

$$\frac{(\varepsilon_s)_{\alpha\alpha}}{(\varepsilon_\infty)_{\alpha\alpha}} = \frac{\omega_{LO}^2(\alpha)}{\omega_{TO}^2(\alpha)} . \tag{3.4}$$

From Table 3.8 it can be seen that the anisotropy of $\boldsymbol{\varepsilon}_s$ is larger than that of $\boldsymbol{\varepsilon}_\infty$. This is due to the different LO–TO splitting of the A_1 compared to the E_1 modes.

According to Table 3.7, the E_1–A_1 splitting, being due to the anisotropy of the short-range forces in the wurtzite lattice (and being larger for AlN than for GaN), is smaller than the LO–TO splitting, being caused by the long-range electric fields. This suggests that the angle-averaged values of the LO and TO frequencies, determined as $(\omega_{\overline{TO}})^2 = \left(\omega_{A_1(TO)}^2 + 2\omega_{E_1(TO)}^2\right)/3$ (and similarly for $\omega_{\overline{LO}}$, cf. [*Luc71*]), should approach those of the respective modes in the zinc-blende structure. As can be seen from Tables 3.5 and 3.8, this is indeed the case. It holds especially well for the TO modes, which is not surprising due to the additional influence of the electric field in the case of the LO modes.

Chapter 4

Influence of Strain on Bulk GaN and AlN

In this chapter, we investigate the influence of macroscopic strains on structural, dielectric, and vibrational properties of the bulk GaN and AlN polytypes under the influence of hydrostatic pressure and uniaxial as well as biaxial stress. Thereby, fundamental material parameters are obtained. As a consequence, this allows for the converse process of deducing the strain state from measured properties.

From the case of hydrostatic pressure, we determine the mode Grüneisen parameters of the phonons. The scaling of the interatomic forces and other properties with the varying atomic distances allows to compare the nitrides with other materials having already revealed interesting behavior due to comprerssion. By investigating uniaxial and biaxial stress, we obtain the phonon deformation potentials as well as some of the elastic constants.

These studies are also useful regarding the investigation of superlattices (cf. the following chapter) with at least one kind of layers being strained due to the different lattice constants of GaN and AlN.

4.1 Relaxation Procedure for the Strained Structures

The strain resulting from a uniaxial or biaxial stress is correspondingly denoted as uniaxial or biaxial. Here, for the cubic nitrides uniaxial stress is assumed to act along one of the cubic axes (as, e. g., [001]), which is taken as the z axis, and for the wurtzite nitrides along the symmetry axis, [0001]. Biaxial stress is assumed to act within the respective perpendicular plane, where it is taken to be isotropic. Under these stress conditions, the resulting strains conserve the wurtzite symmetry but change the cubic lattice into a tetragonal one, so that one always has to distinguish between the in-plane lattice constant, a, and the one along the resulting symmetry axis, c. For the cubic nitrides, the equilibrium tetragonal lattice constants are $a_0 = a_{\mathrm{cub}}/\sqrt{2}$ and $c_0 = a_{\mathrm{cub}}$ (cf. Fig. 2.1).

In general, uniaxial [biaxial] stress is given by a diagonal tensor $\boldsymbol{\sigma} = \mathrm{diag}(0, 0, \sigma_{\parallel})$ [$\boldsymbol{\sigma} = \mathrm{diag}(\sigma_{\perp}, \sigma_{\perp}, 0)$]. It is modeled by a certain strain of the c [a] lattice constant, which is given by $\epsilon_{zz} = (c - c_0)/c_0$ [$\epsilon_{xx} = (a - a_0)/a_0$] and labeled as uniaxial [biaxial] strain $\epsilon_{\parallel}$ [$\epsilon_{\perp}$]. The other lattice constant adjusts itself according to the condition of vanishing stress along its direction. For the tetragonal lattice, this is the only remaining degree of freedom, whereas for the wurtzite structure, also an internal strain $(u - u_0)/u_0$ occurs. In uor calculations, both relax-
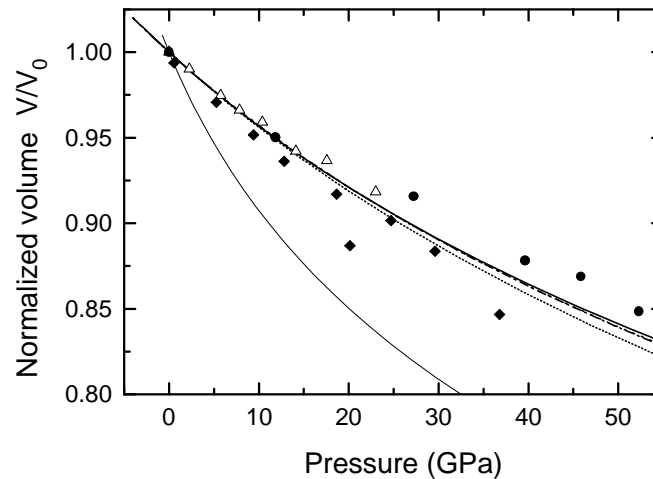
Figure 4.1 Normalized volume versus hydrostatic pressure according to the Vinet equation of state for GaN and AlN in the wurtzite (2*H*) and zinc-blende (3*C*) structures. The respective cell volume V_0 at zero pressure is used for normalization. For comparison, results for zinc-blende GaAs are also given. Solid line: 3*C*-GaN, short-dotted line: 2*H*-GaN, dashed line: 3*C*-AlN, dotted line: 2*H*-AlN, thin solid line: GaAs. Experimental results are plotted for 2*H*-AlN (open triangles [*Uen92*]) and for 2*H*-GaN (filled diamonds [*Xia93*], filled circles [*Uen94*]).

ations are obtained by minimizing the total energy of the strained lattice, as will be described in the following chapter.

4.2   Structural Properties

4.2.1   Hydrostatic Pressure

Results of the total-energy minimizations for GaN and AlN under hydrostatic pressure are presented in Figs. 4.1 and 4.3. Using the Vinet EOS, the relation between the normalized volume and hydrostatic pressure (at zero temperature) is plotted in Fig. 4.1, together with some experimental results [*Uen92*, *Xia93*, *Uen94*]. It is well known that for GaN and AlN these phases change into the cubic rocksalt structure ($O_h^5 = Fm3m$ space group) at remarkably different transition volumes and, hence, pressures. Here, only the low-pressure 2*H* and 3*C* structures are considered and, for comparison, the theoretical EOS is plotted for the whole pressure range considered. The calculated EOS for the two phases of AlN and zinc-blende GaN are nearly identical. To obtain the same volume contraction, a slightly lower hydrostatic pressure has to be applied for wurtzite GaN since it possesses a slightly lower bulk modulus (206 GPa) in comparison to AlN (210 GPa). There is an excellent agreement with the experimental data, which show rather large deviations among themselves. The low-pressure structures of the considered nitrides behave very similarly with respect to their EOS. Moreover, the difference in the EOS of the nitrides is much smaller than the discrepancy in the volumes for a given pressure when the group-III nitrides are compared with a more common III-V compound, e. g. GaAs. The stronger variation of the latter one's volume with hydrostatic pressure is in agreement with its
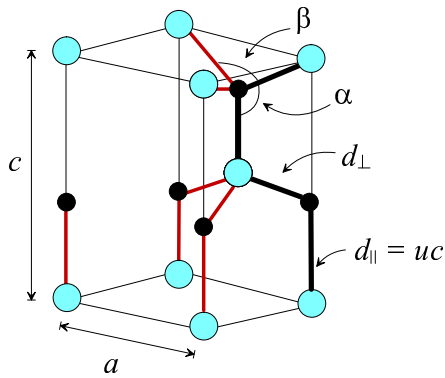
Figure 4.2 Geometry elements (bond lengths and bond angles) of the wurtzite structure. $d_\parallel$: bond length along the c axis; $d_\perp$: bond length nearly perpendicular to the c axis; α: angle between the c axis and the bond nearly perpendicular to it; β: angle between two bonds nearly perpendicular to the c axis.
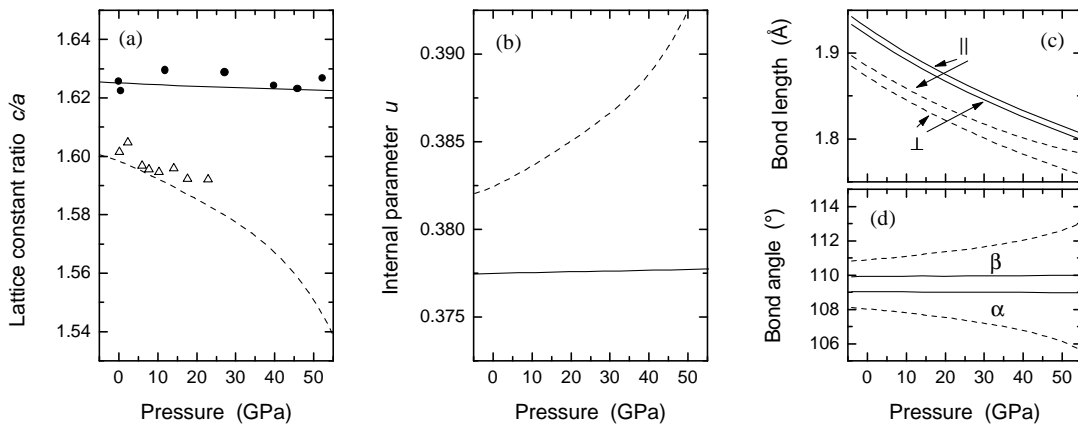

Figure 4.3 Structural parameters of wurtzite GaN and AlN under hydrostatic pressure. Solid lines: GaN, dashed lines: AlN. (a) Ratio of the lattice constants c/a versus pressure. Experimental results are plotted for 2H-AlN (open triangles [*Uen92*]) and for 2H-GaN (filled circles [*Uen94*]). (b) Internal parameter u versus pressure. (c) Lengths of the two inequivalent bonds versus pressure. (d) Bond angles versus pressure. For the labeling, see the corresponding symbols of Fig. 4.2.

weaker chemical bonding, since the cohesive energy per bond, 1.63 eV, is much smaller than the corresponding values of GaN (2.24 eV) and AlN (2.88 eV) [*Har89*].

In contrast to the similarity in the EOS, the crystal lattices of wurtzite GaN and AlN behave quite differently. The calculated ratio of the two lattice constants c/a and the internal parameter u are plotted versus hydrostatic pressure in Figs. 4.3(a) and (b). For GaN the two quantities are quite close to the ideal values. Their pressure dependence is negligible, with linear pressure coefficients of $[\partial(\frac{c}{a})/\partial p]_{p=0} = -4.7 \times 10^{-5}\,\mathrm{GPa}^{-1}$ and $(\partial u/\partial p)_{p=0} = 5 \times 10^{-6}\,\mathrm{GPa}^{-1}$. For AlN, the situation is completely different. The values c/a (u) are remarkably smaller (larger) than the ideal values and decrease (increase) with rising hydrostatic pressure, with coefficients of $[\partial(\frac{c}{a})/\partial p]_{p=0} = -5.6 \times 10^{-4}\,\mathrm{GPa}^{-1}$ and $(\partial u/\partial p)_{p=0} = 1.08 \times 10^{-4}\,\mathrm{GPa}^{-1}$.

The results are in reasonable agreement with experimental studies of the lattice constants under pressure [*Uen92, Uen94*]. For GaN, the nearly constant ratio c/a was infered also from optical measurements of the crystal-field splitting for compressed samples [*Liu98*]. The pres-
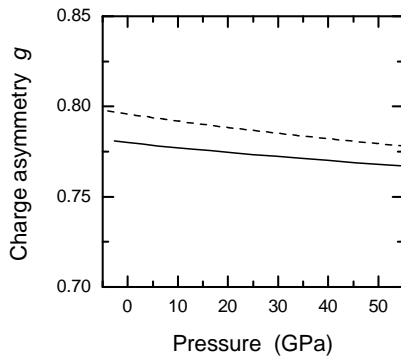
Figure 4.4 Charge asymmetry coefficient g of cubic nitrides versus hydrostatic pressure. Solid line: $3C$-GaN, dashed line: $3C$-AlN.

sure behavior of u is consistent with that of c/a: Assuming nearly equal bond lengths parallel and perpendicular to the c axis [which is justified, cf. Fig. 4.3(c)], the resulting relation $u \approx \frac{1}{4} + \frac{1}{3}\left(\frac{a}{c}\right)^2$ leads to an internal parameter $u > \frac{3}{8}$, which increases as c/a decreases.

As a consequence of the different variations of c/a and u in GaN and AlN, one finds different lattice deformations under pressure. In Figs. 4.3(c) and (d) the lengths of the inequivalent bonds and the angles between them are plotted versus hydrostatic pressure. As can be expected from Figs. 4.3(a) and (b), for GaN these quantities are close to those in an ideal tetrahedron (equal bond lengths, identical bond angles of 109.47°). With rising hydrostatic pressure, indeed the bond angles remain almost constant, i.e., besides shrinking bond lengths no remarkable change occurs in the shape of the tetrahedral structure. Now, for AlN the significant deviations from the ideal wurtzite structure are further enlarged under pressure. Especially the difference between the bond angles increases in such a way that the zig-zag chains perpendicular to the c axis are flattened, i.e., the bonding tetrahedra are compressed along the c axis by shrinking the vertical distance $\left(\frac{1}{2} - u\right)c$ of the Al–N layers. This implies a tendency for dehybridization from ideal sp^3 bonds towards sp^2 and p_z orbitals.

The trend of crystallizing within wurtzite structure and, in particular, to exhibit bond angles different from the ideal tetrahedron ones has often been related to the large ionicity of the chemical bonds. The bond ionicity can be characterized by the charge asymmetry coefficient g according to Garcia and Cohen [*Gar93a*]. It is plotted in Fig. 4.4 versus pressure for the zinc-blende phase of GaN and AlN. A weak decrease of g with rising pressure is observed (slopes: $-3 \times 10^{-4}\,\mathrm{GPa}^{-1}$ for GaN, $-4 \times 10^{-4}\,\mathrm{GPa}^{-1}$ for AlN). This means that the logarithmic derivative of g with respect to the volume is positive. At least for AlN, this behavior is seemingly in contrast to the increase of the deviations of c/a and u from the values of the ideal wurtzite structure, since this is usually related to an increasing bond ionicity. However, this argument stems from the comparison of different materials exhibiting different ionicities at their equilibrium. On the other hand, with rising pressure and decreasing bond lengths the overlap of the valence electron wave functions increases. Consequently, the increasing probability of finding an electron closer to the cation, too, results in smaller values of the bond ionicity.

4.2.2 Uniaxial and Biaxial Strain

Structural results of the total-energy optimizations for the nominally cubic nitrides are presented in Figs. 4.5 and 4.6 for biaxial and uniaxial strain, respectively. There is no significant difference
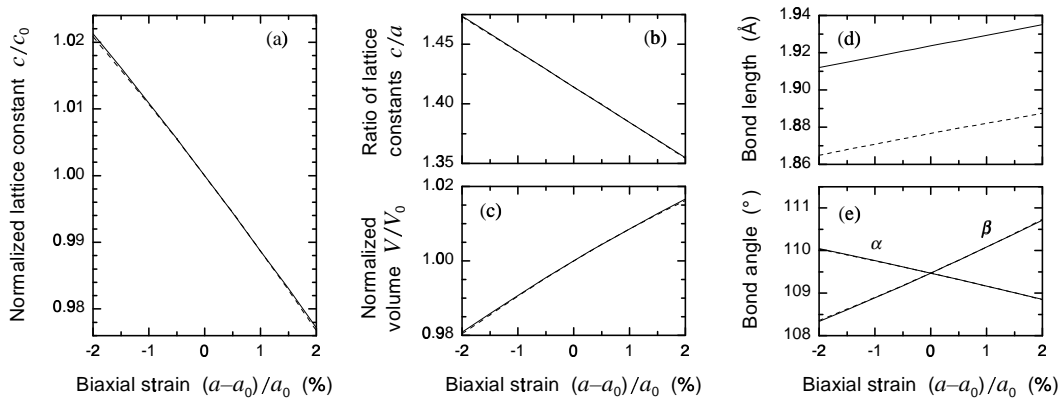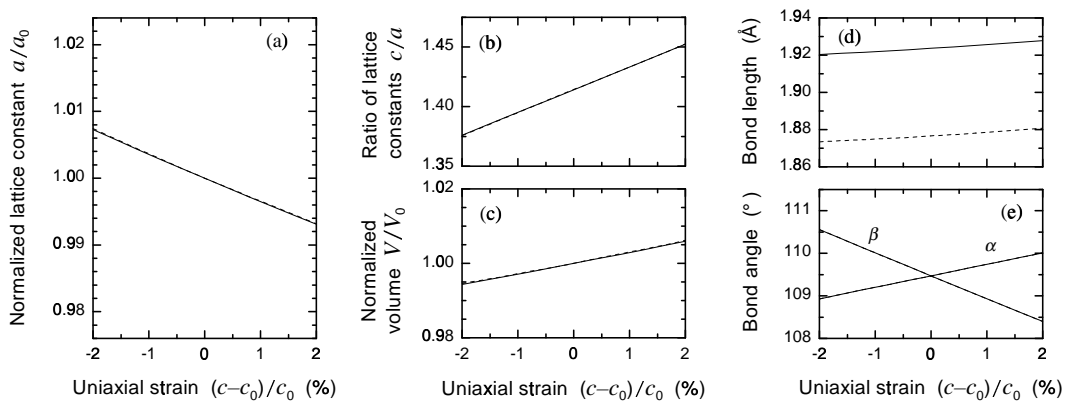
Figure 4.5 Parameters of the tetragonally distorted atomic geometry of cubic nitrides versus biaxial strain: (a) normalized lattice constant c/c_0, (b) ratio of lattice constants c/a, (c) normalized volume V/V_0, (d) bond length, and (e) bond angles; solid line: $3C$-GaN, dashed line: $3C$-AlN. The label α (β) denotes the angle between bonds pointing along opposite directions with respect to their z component (pointing along the same direction with respect to their z component), similar to the wurtzite case.

between $3C$-GaN and $3C$-AlN with respect to their strain behavior. The decrease of the c lattice constant with increasing tensile biaxial strain is about three times of the a lattice constant for tensile uniaxial strain. For large strains, slight nonlinearities are found. The linear strain coefficients are given in Table 4.1.

Both for increasing tensile biaxial and tensile uniaxial strain the cell volume increases, since the relaxation of the stress-free lattice constant does not completely compensate for the change of the strained one. This is due to the stiffness of the lattice, here resulting from an interplay of the changes of bond length and bond angles; it is described in the following.

Picture the lattice deformation as a two-step process: First, imagine the atoms being clamped in the stress-free direction so that they can be shifted only along the direction of the macroscopic

Figure 4.6 Parameters of the tetragonally distorted atomic geometry of cubic nitrides versus uniaxial strain. Same as Fig. 4.5, but instead of c the lattice constant a is shown in (a).

Table 4.1 Strain-free values X_0 and linear strain coefficients $\frac{1}{X_0}\left(\frac{\partial X}{\partial \epsilon_{\perp/\parallel}}\right)_0$ of parameters of atomic geometry ($X = c, a, c/a$, and d) of the tetragonally strained cubic nitrides (absolute lengths in Å).

param.	3C-GaN			3C-AlN		
X	X_0	$(\epsilon_\perp)$	$(\epsilon_\parallel)$	X_0	$(\epsilon_\perp)$	$(\epsilon_\parallel)$
c	4.443	−1.109	1.000	4.334	−1.097	1.000
a	3.141	1.000	−0.355	3.064	1.000	−0.353
c/a	$\sqrt{2}$	−2.98	1.91	$\sqrt{2}$	−2.97	1.91
d	1.924	0.572	0.186	1.877	0.565	0.183

stress, and second, the atoms being "released" and shifted along the perpendicular direction due to the lattice relaxation. The difference in the behavior of bond length and bond angles ist that the latter undergo similar changes in both steps, whereas the bond-length variations are of opposite sign. This means if in the first step an angle increases, it also increases in the second step, but if a bond gets stretched in the first step, it will shorten again in the second step (and vice versa). Therefore, in the second (i. e., the relaxation) step a balance is established between the angular forces that govern the further distortion of the bond angles and the central forces that tend to recover the bond length.

As one can see from Figs. 4.5 and 4.6, the bond length varies only weakly compared to the bond angle β. This shows the tendency of the nitrides' lattice to be more resistant to changes of its bond lengths than to changes of its bond angles. The bond length varies less for uniaxial strain, which is ultimately due to the lattice relaxation taking place in two dimensions. The bond angles behave very similar for biaxial and uniaxial strain, because β depends on the ratio c/c_0 only, and the c lattice constant exhibits similar variations for uniaxial and biaxial strain, as can be seen from Table 4.1.

Table 4.2 Strain-free values X_0 and linear strain coefficients $\frac{1}{X_0}\left(\frac{\partial X}{\partial \epsilon_{\perp/\parallel}}\right)_0$ of parameters of atomic geometry ($X = c, a, c/a, u, d_\parallel$, and $d_\perp$) of the wurtzite nitrides (absolute lengths in Å).

| param.	2H-GaN			2H-AlN		
X	X_0	$(\epsilon_\perp)$	$(\epsilon_\parallel)$	X_0	$(\epsilon_\perp)$	$(\epsilon_\parallel)$
c	5.111	−0.502	1.000	4.929	−0.611	1.000
a	3.145	1.000	−0.202	3.084	1.000	−0.210
c/a	1.6252	−1.507	1.199	1.5982	−1.621	1.209
u	0.3775	0.694	−0.551	0.3825	0.805	−0.633
$d_\parallel$	1.929	0.193	0.448	1.885	0.188	0.368
$d_\perp$	1.921	0.611	0.107	1.872	0.594	0.103
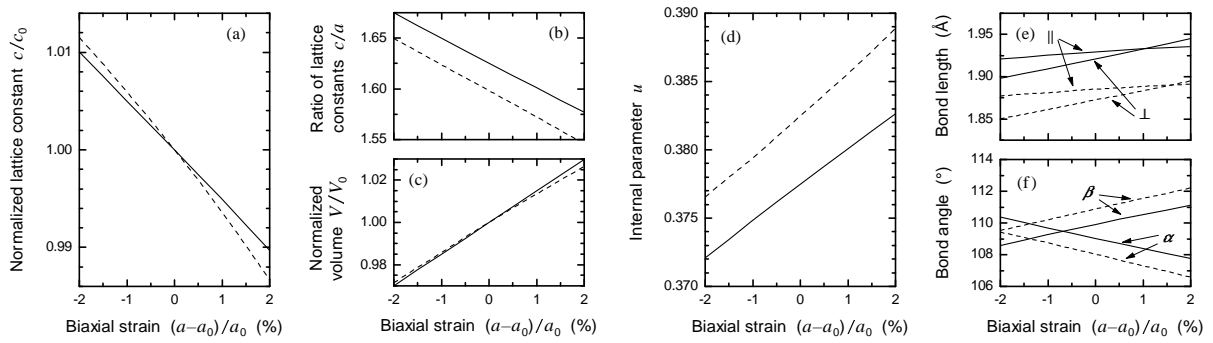
Figure 4.7 Parameters of the wurtzite atomic geometry versus biaxial strain: (a) normalized lattice constant c/c_0, (b) ratio of lattice constants c/a, (c) normalized volume V/V_0, (d) internal parameter u, (e) bond lengths, and (f) bond angles. Solid line: $2H$-GaN, dashed line: $2H$-AlN. For the labeling, see the corresponding symbols of Fig. 4.2.

Structural results of the total-energy optimizations for the wurtzite nitrides are presented in Figs. 4.7 and 4.8 for biaxial and uniaxial strain, respectively. As expected, due to the lattice relaxation (Poisson effect) one observes a decrease of the c (a) lattice constant with increasing tensile biaxial (uniaxial) strain. The corresponding linear strain coefficients are summarized in Table 4.2. As for the cubic structure, the volume increases in both cases for increasing tensile strain as a net effect. The internal parameter u and, hence, the internal strain $(u - u_0)/u_0$ obviously show a different strain behavior than the lattice constants, which is nevertheless systematic: They always change in the opposite way to the ratio of the lattice constants. As c/a shrinks, u increases (and vice versa), regardless of the strain type (uniaxial or biaxial). The same behavior was also found for hydrostatic pressure (cf. Fig. 4.3).

The rather strong internal strain effects dominate the variations of the bond lengths and bond angles [Figs. 4.7(e, f) and 4.8(e, f)]. Interestingly, the lengths $d_{\parallel} = uc$ of the bonds parallel to the c axis increase for both strains. The effect is stronger for uniaxial strain, following directly the increase of c. Moreover, even for biaxial strain the decrease of the c-lattice constant is accompanied by an increase in bond lengths parallel to the c axis. The lengths of the bonds
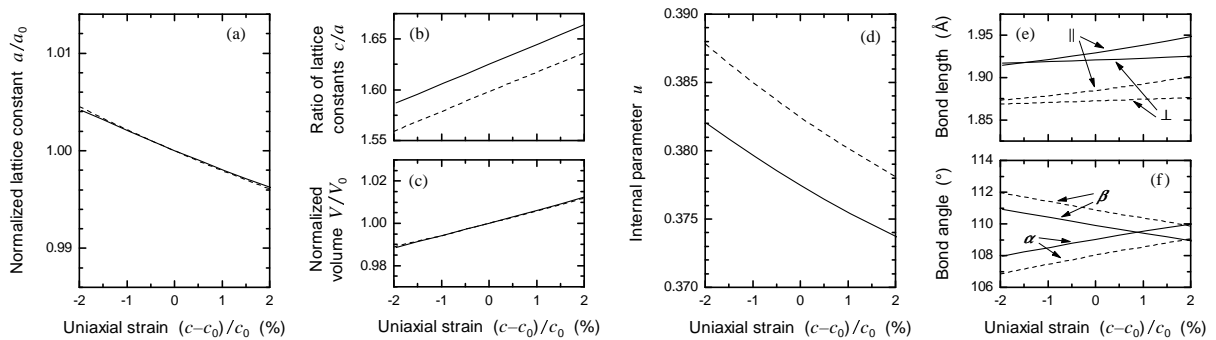
Figure 4.8 Parameters of the wurtzite atomic geometry versus uniaxial strain. Same as Fig. 4.7, but instead of c the lattice constant a is shown in (a).

nonparallel to the c axis, $d_\perp = \left[\frac{1}{3}a^2 + \left(\frac{1}{2} - u\right)^2 c^2\right]^{1/2}$, also increase with tensile biaxial strain, while in the uniaxial case, there is more or less a compensation of the variations of c, a, and u, resulting in almost constant bond lengths $d_\perp$. For certain strain values, all bond lengths of one material become equal. However, this does not result in ideal tetrahedra, since the bond angles remain different.

The opposite behavior of the bond angles α and β versus biaxial or uniaxial strain is particularly interesting, since it implies a tendency to reduce the deformation of the bonding tetrahedra for compressive biaxial strain or tensile uniaxial strain. The angles approach the value $109.47°$ of the ideal tetrahedron. However, because of unequal bond lengths, again the tetrahedra remain deformed. For the opposite case of tensile biaxial strain and compressive uniaxial strain, the bonding tetrahedra are compressed along the c axis and the angle α tends towards $90°$, whereas the angle β tends towards $120°$. As for $2H$-AlN under hydrostatic pressure, this implies a tendency for dehybridization from ideal sp^3 hybrids towards sp^2 and p_z orbitals also in this case.

4.3   Elastic Properties

4.3.1   Zinc-Blende Phase

The elastic constants, determined as a by-product of the relaxation (cf. Sect. 2.6.2), are given in Table 4.3, together with other theoretical results. Nearly all data show a pretty good overall agreement. Unfortunately, no experimental data are available.

It is a general property of cubic crystals (as well as of elastically isotropic materials) that the Poisson ratio and the biaxial relaxation coefficient are not independent, since it holds that $R_c^b = 2\nu_c/(1 - \nu_c)$ [or $\nu_c = R_c^b/(2 + R_c^b)$, respectively]. Here, however, R_c^b and ν_c have been obtained independently. Their consistency is tested using the above formulae, Table 4.3 shows a satisfactory agreement. Interestingly, from Table 4.3 it can be seen that even a perfect consistency between the values of R_c^b und ν_c does however not guarantee reliable results.

The fractional volume change $\Delta V/V_0 = 2\epsilon_{xx} + \epsilon_{zz}$ amounts to $(2 - R_c^b)\epsilon_\perp$ in the biaxial case and to $(1 - 2\nu_c)\epsilon_\parallel$ in the uniaxial one. The values of the prefactors are found as the slope of the curves in Figs. 4.5(c) and 4.6(c). In order for the volume to remain constant, the prefactors needed to vanish, which implies $R_c^b = 2$ and $\nu_c = \frac{1}{2}$. These values would only be reached if, in the relaxation step, the bond angles would change by a much larger amount than they actually do. Since the observed ν_c gets much closer to its respective "critical value" than R_c^b, the relative change in volume is significantly smaller for uniaxial than for biaxial strain.

4.3.2   Wurtzite Phase

From the data shown in Figs. 4.7(a) and 4.8(a) the coefficients R_c^b and ν_c are immediately obtained. They are shown and compared with other theoretical and experimental data (derived from elastic stiffness constants) in Table 4.4. In general, the behavior of $2H$-GaN and $2H$-AlN is rather similar. It can be noticed, however, that the effect of biaxial strain (as expressed by R_c^b) is larger than that of uniaxial strain (as expressed by ν_c) by a factor of about 2.6 for $2H$-GaN and 2.9 for $2H$-AlN. As for the cubic nitrides, the resulting change in volume is much larger for biaxial than for uniaxial strain.

Table 4.3 Elastic stiffness constants (in GPa) as well as related moduli and coefficients (see text) of zinc-blende GaN and AlN compared with results of other *ab initio* calculations[a–d].

		R_c^{b}	v_c	$\frac{2v_c}{1-v_c}$	$\frac{R_c^{\mathrm{b}}}{2+R_c^{\mathrm{b}}}$	B_0	c_{11}	c_{12}	E_c	Y_c
3*C*-GaN	present	1.109	0.355	1.101	0.357	206.5	296	164	179	278
	calc.[a]	1.085	0.352	1.086	0.352	204	293	159	181	279
	calc.[b]	1.130	0.361	1.130	0.361	203	285	161	169	264
	calc.[c]	0.848	0.298	0.848	0.298	183	297	126	222	316
	calc.[d]	1.041	0.342	1.041	0.342	201	296	154	191	290
3*C*-AlN	present	1.097	0.353	1.091	0.354	210.2	303	166	186	287
	calc.[a]	1.053	0.345	1.053	0.345	208	304	160	194	296
	calc.[b]	1.073	0.349	1.072	0.349	216	313	168	196	301
	calc.[c]	1.000	0.333	1.000	0.333	209	314	157	209	314
	calc.[d]	1.000	0.333	1.000	0.333	203	304	152	203	304

[a] [*Wri97*] [b] [*Shi98*] [c] [*Bec00*] [d] [*Kim96*]

Table 4.4 Elastic stiffness constants (in GPa) as well as related moduli and coefficients (see text) of wurtzite GaN and AlN, compared with results of other *ab initio* calculations[a,b] and measurements[c–g]. For all data sets, the hydrostatic relaxation coefficient is derived from the elastic constants via Eq. (2.90). Except for the present ones, the values of the bulk modulus are derived from the elastic constants using Eq. (2.93).

		R_c^{b}	v_c	$\frac{2v_c}{1-v_c}$	R_c^{h}	Y_c	E_c	B_0	$C_{11}+C_{12}$	C_{13}	C_{33}
2*H*-GaN	present	0.502	0.202	0.506	0.99	463	373	206	515	104	414
	calc.[a]	0.509	0.205	0.516	0.98	450	363	202	502	103	405
	calc.[b]	0.553	0.212	0.538	1.04	432	332	197	490	104	376
	exper.[c]	0.533	0.198	0.494	1.11	479	356	210	535	106	398
	exper.[e]	0.564	0.212	0.538	1.07	458	343	208	520	110	390
	exper.[f]	0.598	0.228	0.591	1.02	432	329	204	500	114	381
	exper.[g]	1.18	0.371	1.18	1.01	239	150	195	426	158	267
2*H*-AlN	present	0.611	0.210	0.532	1.21	469	322	210	538	113	370
	calc.[a]	0.579	0.203	0.509	1.20	470	329	207	533	108	373
	calc.[b]	0.585	0.207	0.522	1.17	474	337	212	540	112	383
	exper.[d]	0.509	0.177	0.430	1.25	510	354	210	560	99	389
	exper.[e]	0.513	0.182	0.445	1.21	499	354	209	550	100	390

[a] [*Wri97*] [c] [*Pol96*] [e] [*Deg98*] [g] [*Sav78*]
[b] [*Shi98*] [d] [*McN93*] [f] [*Yam97, Yam99*]

For cubic crystals and for elastically isotropic materials, $R_c^{\mathrm{b}} = \frac{2v_c}{1-v_c}$ holds. Due to their uniaxial crystal structure, the wurtzite nitrides may exhibit an anisotropic behavior. Compar-

ing the ratio $\frac{2\nu_c}{1-\nu_c}$ with the actual value of R_c^b provides information about the deviation of their elastic properties from isotropic behavior. It is obvious from Table 4.4 that for 2H-GaN $\frac{2\nu_c}{1-\nu_c}$ gets rather close to R_c^b, while for 2H-AlN there are significant differences. The deviating elastic properties of the two nitrides under consideration are also visible in the presence of hydrostatic pressure, where a characteristic behavior of the axial ratio c/a is observed. The latter can also be expressed by the hydrostatic relaxation coefficient which, in the hydrostatic-pressure calculation, is found to be 1.02 for 2H-GaN and 1.23 for 2H-AlN. These values have to be compared to those given in Table 4.4 which were derived from the elastic constants as obtained from the uniaxial and biaxial relaxation. Again this shows a very satisfactory agreement between the independent calculations.

From the R_c^h values of Table 4.4 it follows that only 2H-GaN exhibits a compression approximately homogeneous (i.e., a proportional contraction), since $R_c^h(\text{GaN}) \approx 1.0$, while for 2$H$-AlN the compression is anisotropic [$R_c^h(\text{AlN}) \approx 1.2$]. This has been observed directly in high-pressure X-ray-diffraction experiments [*Uen92, Uen94*] and was also found in other *ab initio* calculations for hydrostatic pressure [*Chr93, Ser00*]. Therefore, the quality of calculations and measurements of elastic stiffness constants of wurtzite GaN and AlN can be easily characterized by the dimensionless quantities R_c^b, ν_c, $\frac{2\nu_c}{1-\nu_c}$, and R_c^h. This is important, for there are many data published for the elastic constants exhibiting a broad range of values, and it is therefore desirable to have criteria at hand that help to choose reliable ones. For instance, for 2H-GaN it appears that reliable values are close to $R_c^b = 0.50 \ldots 0.56$, $\nu_c = 0.20 \ldots 0.21$, $\frac{2\nu}{1-\nu} = 0.49 \ldots 0.54$, and $R_c^h \approx 1.0$. The situation is somewhat less clear for 2H-AlN, since the deviations between the results are larger. Nevertheless, reliable values can be expected to fall in the range $R_c^b = 0.5 \ldots 0.6$, $\nu_c = 0.18 \ldots 0.21$, $\frac{2\nu_c}{1-\nu_c} = 0.45 \ldots 0.53$, and $R_c^h \gtrsim 1.2$.

The reason for the different elastic behavior of wurtzite GaN and AlN can be traced back to the elastic stiffness constants (cf. Table 4.4). The present results are in excellent agreement with other *ab initio* calculations [*Wri97*]. This holds in particular for AlN. For GaN, the stiffness constants calculated within our method are slightly larger, mainly due to the relatively small value of R_c^b. The agreement with measured values [*Pol96, Deg98, Yam97, McN93*] is reasonable for both nitrides. Therefore, since in our case all quantities stem from the same type of DFT calculations, the derived elastic constants represent a reliable basis for extracting phonon and electronic deformation potentials. For 2H-GaN there is one set of experimental results [*Sav78*] which should not be used any longer. Unfortunately, this particular set of values has been published in the Landolt-Börnstein series.

According to Table 4.4, the relation $C_{11} + C_{12} \approx C_{13} + C_{33}$ holds with good accuracy for 2H-GaN but not for 2H-AlN. This is in complete agreement with the relations $R_c^h \approx 1.0$ and $\frac{2\nu_c}{1-\nu_c} \approx R_c^b$, that are fulfilled for 2H-GaN and indicating a quasicubic behavior. The different elastic behavior of wurtzite GaN and AlN is mainly determined by the larger $C_{11} + C_{12}$ value of AlN, which also causes its larger biaxial modulus Y. The value of the ratio $R_c^b / \frac{2\nu_c}{1-\nu_c} = (C_{11} + C_{12} - C_{13})/C_{33}$ can serve as an estimate for a lower (upper) limit of R_c^h if it is larger (smaller) than 1.0. Due to the quasicubic behavior, the relations between the elastic moduli for 2H-GaN can be approximated by simplified expressions. The biaxial modulus and the Young modulus are related to the bulk modulus via $Y \approx 3B_0(1 - \frac{1}{2}R_c^b) = 3B_0(1 - 2\nu_c)/(1 - \nu_c)$ and $E \approx 3B_0(1 - \frac{1}{2}R_c^b)/(1 + \frac{1}{2}R_c^b) = 3B_0(1 - 2\nu_c)$. These two moduli are related to each other by

$E \approx Y/(1 + \frac{1}{2}R_c^b) = Y(1 - \nu_c)$. Obviously, in each of these equations the conversion factors between the elastic moduli can be expressed using either the biaxial relaxation coefficient or the Poisson ratio, which themselves are related to each other through $R_c^b = \frac{2\nu_c}{1-\nu_c}$ (as mentioned above). Table 4.4 shows that these relations are by no means valid for 2*H*-AlN.

In contrast to the experimentally and theoretically well-established results for the hydrostatic coefficient R_c^h, there are contradictory reports on *direct* experimental results for the biaxial strain ratio R_c^b of GaN. For AlN no values at all are reported. The measured values R_c^b(GaN), of 0.48 [*Dav97*], 0.43 [*Yam01*], and 0.38 [*Det92*] (sometimes the latter value has been cited to be the Poisson ratio) show significant deviations among themselves. Additionally, from the results obtained by Romano and coworkers [*Rom00*], a value of 0.386 can be extracted (which fits their data better than the one from the literature which they used), and from Fig. 1 of [*Ama88*], a value of 0.45 can be obtained, if the data from Leszczynski *et al.* [*Les96*] are used as strain-free reference for the lattice constants. Furthermore, values of 0.457 [*Maj96*] as well as 0.400 and 0.384 [*Zor01*] have been calculated by first-principles methods. Except for the largest ones, these data significantly underestimate the results listed in Table 4.4. The elastic constants that can be derived from these data (assuming quasicubic behavior and using an average value for the bulk modulus) show the general trend that C_{13} turns out too small and all the other ones too large. Unfortunately, there are no reports on directly measured values of ν_c in the literature.

The reasons for these deviations are not entirely clear, but some ideas can be suggested. To determine the strain, a reference value needs to be known corresponding to a fully relaxed crystal and therefore representing the strain-free case. In general, the lattice constants of 2*H*-GaN show unusually large fluctuations [*Lag79*], and it is difficult to determine the "true" unstrained values [*Les96*]. Now, strictly speaking, for the purpose of investigating elastic relaxation this reference value has to be understood as describing a crystal *free from external stress*. Internal strain effects due to defects, substituent atoms, and free carriers may still be present, and the equilibrium lattice constants may vary between different samples. Therefore, "the" pair of reference values a_0, c_0 of an ideal 2*H*-GaN crystal cannot be universally applicable. On the other hand, considering the *same* crystal in both the stressed and the stress-free state, the biaxial relaxation behavior manifests itself as the *slope* of the c versus the a lattice constant, independent of their equilibrium values. By definition, it holds

$$R_c^b = -\frac{\epsilon_{zz}}{\epsilon_{xx}} = -\frac{c - c_0}{c_0}\frac{a_0}{a - a_0} = -\frac{\Delta c}{\Delta a}\frac{a_0}{c_0}. \qquad (4.1)$$

In the last expression, Δc and Δa don't need to refer to the equilibrium values. Rather, their quotient represents the above-mentioned slope. Obviously, in extracting R_c^b from a measured slope, the equilibrium value of c/a is of minor numerical influence.

However, the above-mentioned experimental values R_c^b(GaN) were obtained from a comparison of different samples, not from one single crystal subjected to varying stress or strain states (as for hydrostatic pressure). In contrast, the elastic stiffness constants have been measured for only one sample and can therefore be expected to be more reliable in representing the elastic behavior of the wurtzite nitrides. To resolve this problem, combined X-ray and uniaxial-pressure experiments are necessary in order to directly observe the Poisson effect of wurtzite GaN and AlN single crystals.
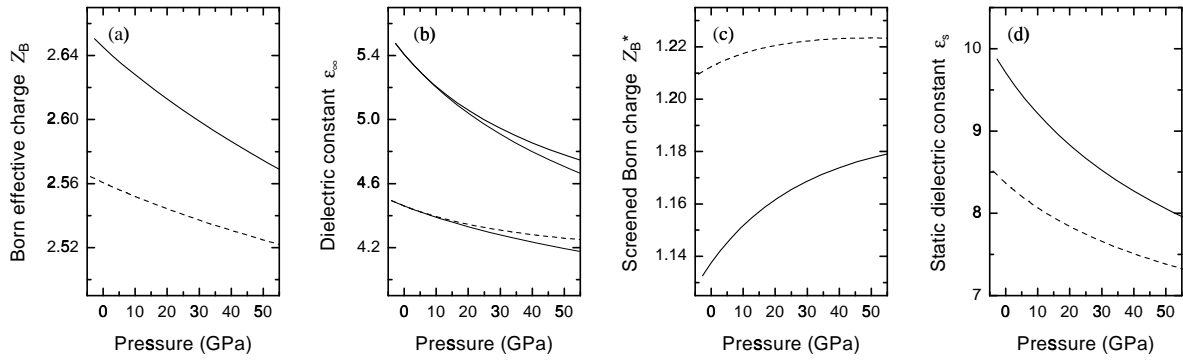
Figure 4.9 (a) Born effective charge and (b) high-frequency dielectric constant versus hydrostatic pressure for zinc-blende GaN (solid line) and AlN (dashed line). The thin lines [in (b)] represent expression (4.2). (c) Resulting screened effective ion charge. (d) Static dielectric constant as derived from the LST relation.

4.4　Dielectric Properties

4.4.1　Hydrostatic Pressure

In Figs. 4.9(a) and (b), the calculated pressure dependence of the Born effective charge Z_B and the high-frequency dielectric constant ε_∞ for the cubic phases is presented. For the wurtzite nitrides the pressure behavior of the respective tensor components is plotted in Figs. 4.10 and 4.11. Independent of the polytype and of the nitride, the quantities under consideration decrease monotonously with rising pressure, except for the $(Z_B)_{zz}$ component of $2H$-AlN. The latter exhibits a saturation between 10 and 20 GPa, followed by a significant increase. This is likely due to the mentioned dehybridization accompanying the tetrahedron deformation. In general, the pressure (and, hence, volume) dependence is more pronounced for GaN because of the stronger covalent bonding in AlN.

　　The numerical results for the initial slopes of the logarithmic volume as well as the pressure behavior of the Born effective charge are given in Table 4.5. The pressure-induced re-

Table 4.5 Logarithmic derivative $(\partial \ln Z_B / \partial \ln V)_{V=V_0}$ and pressure coefficients $(\partial Z_B / \partial p)_{p=0}$ $(10^{-3}\,\mathrm{GPa}^{-1})$ of the (tensor components of the) Born effective charge of zinc-blende (wurtzite) AlN and GaN. Available literature data are given for comparison.

|			AlN			GaN	
		Z_B	$(Z_B)_{xx}$	$(Z_B)_{zz}$	Z_B	$(Z_B)_{xx}$	$(Z_B)_{zz}$
$(\partial \ln Z_B / \partial \ln V)_{V=V_0}$	present	0.074	0.086	0.022	0.149	0.137	0.151
	calc.[a]				0.139		
$(\partial Z_B / \partial p)_{p=0}$	present	−0.9	−1.0	−0.3	−1.8	−1.7	−2.0
	exper.[b]						−2.4 ± 0.5

[a] [*Sen95*]　　　　　　　　　　　　　　　　[b] [*Per99*]
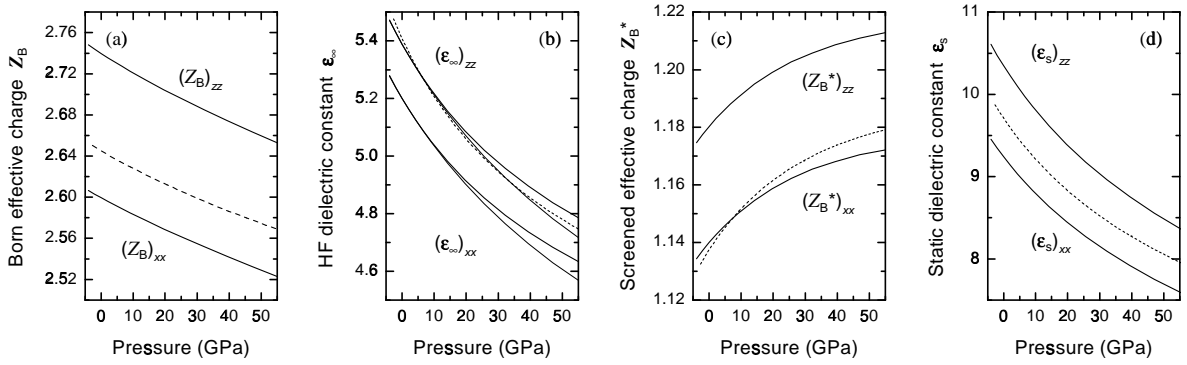
Figure 4.10 Pressure dependence of (a) the two independent tensor components of the Born effective charge, (b) the high-frequency dielectric constant, (c) the screened effective charge and (d) the static dielectric constant of $2H$-GaN. For comparison the $3C$ results are plotted as dashed lines. The thin lines in (b) represent expression (4.2).
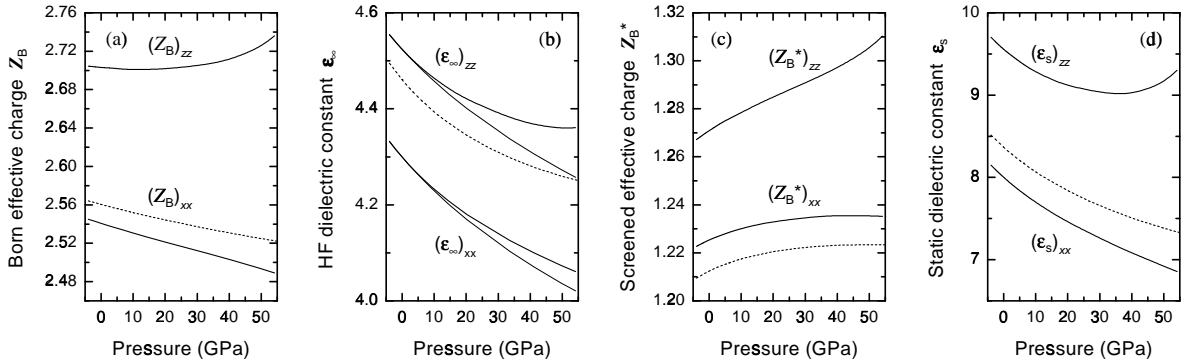
Figure 4.11 Same as Fig. 4.10, but for $2H$-AlN.

duction of these dynamical ion charges indicates a charge redistribution from the nitrogen atoms to the gallium or aluminium atoms compared to the pressure-free situation. Although this holds for atoms being displaced from their equilibrium positions, we find the same trend as already described for the static ionic charge defined by the charge asymmetry coefficient (cf. Fig. 4.4). The dynamic and the static charge of the cubic polytypes are compared in Fig. 4.12(a). The charge asymmetry coefficient takes similar values, while the Born effective charge differs for GaN and AlN and, in particular, covers different ranges of values. For AlN, which
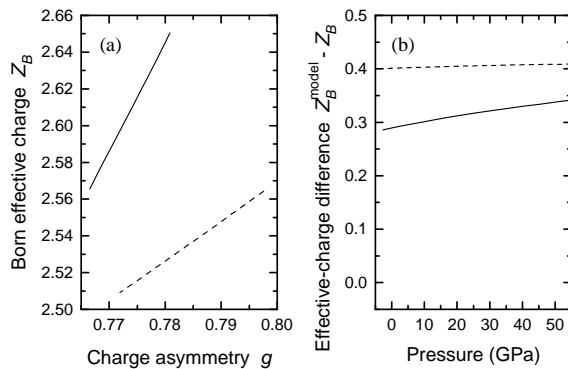
Figure 4.12 (a) Comparison of the Born effective charge with the static charge asymmetry coefficient (for the whole pressure range). (b) Difference of the model effective charge (see text) and the *ab initio* result for the Born effective charge versus hydrostatic pressure. Solid line: $3C$-GaN, dashed line: $3C$-AlN.

has a higher static ionicity, this range is smaller than for GaN. Interpreting the static charge asymmetry coefficient g as a bond polarizability, it can be related to the dynamic charge by $Z_B^{model} = -\frac{1}{2}\Delta Z + 4g + \frac{8}{3}g(1 - g^2)$, with $\Delta Z = 2$ as the difference between the number of valence electrons of group III and V elements [*Har89*]. For the nitrides considered here, the g values are rather large, and therefore the use of the model formula leads to an overestimation of the dynamic charge, as is shown in Fig. 4.12(b). For AlN, this difference is nearly constant, whereas for GaN it increases with pressure. Therefore, the pressure dependence obtained from the model, $\partial Z_B^{model}/\partial p = (20/3 - 8g^2)\partial g/\partial p$, gives correctly the one found for AlN, whereas it slightly overestimates the one for GaN. This justifies the use of the model pressure dependence having been used throughout the literature.

The variation of the high-frequency dielectric constants versus pressure, as shown in Figs. 4.9(b), 4.10(b) and 4.11(b), exhibits a significant nonlinear behavior already for not too large pressures. According to the bond-orbital model [*Har89*], the underlying volume dependence may be described by

$$\varepsilon_\infty(V) = 1 + [\varepsilon_\infty(V_0) - 1]\frac{(V_0/V)^{5/3}}{\left\{1 + C\left[(V_0/V)^{4/3} - 1\right]\right\}^{3/2}} \tag{4.2}$$

with a certain constant C. It is related by

$$C = \frac{1}{2}\left[\frac{B_0}{\varepsilon_\infty(V_0) - 1}\left(-\frac{\partial \varepsilon_\infty}{\partial p}\right)_{p=0} + \frac{5}{3}\right]$$

to the bulk modulus B_0 and the linear pressure coefficient $(\partial \varepsilon_\infty/\partial p)_{p=0}$. This constant takes the values $C = 1.39$ (3C-GaN) and 1.07 (3C-AlN); when applied to the tensor components of the wurtzite phase materials, one has $C = 1.29$ and 1.30 (2H-GaN, xx and zz component, respectively) as well as 1.08 and 1.05 (2H-AlN, analogously). With relation (4.2) the low-pressure range for AlN (i.e., below 10 GPa) is excellently reproduced, whereas for GaN the approximation is applicable even to slightly higher pressures (about 15 GPa).

Very interesting is the behavior of the screened charges $Z_B^* = Z_B/\sqrt{\varepsilon_\infty}$ under pressure as presented for the zinc-blende nitrides in Fig. 4.9(c). The pressure dependences of the dynamic ionic charge and of the dielectric constant nearly cancel each other. As a net effect, the screened charge increases slightly with increasing pressure. For AlN the screened charge varies only in the range $Z_B^* \approx 1.21 \dots 1.22$. Due to the weaker covalent bonds in GaN the net pressure effect on Z_B^* is more pronounced. There is a tendency for a saturation at rather large pressures. For the hexagonal polytypes one obtains an analogous behavior because of the similar pressure dependence, as can be seen from Figs. 4.10(c) and 4.11(c).

4.4.2   Uni- and Biaxial Strain

The Born and screened effective charges as well as the high-frequency and static dielectric constants of 3C-GaN and 3C-AlN are presented in Figs. 4.13 and 4.14, respectively. They show a markedly nonlinear behavior. Nevertheless, despite the easily noticeable differences between 3C-GaN and 3C-AlN, the basic trend is the same for the tensor components of the Born effective charge. However, opposite trends for the tensor components of the dielectric constants occur.
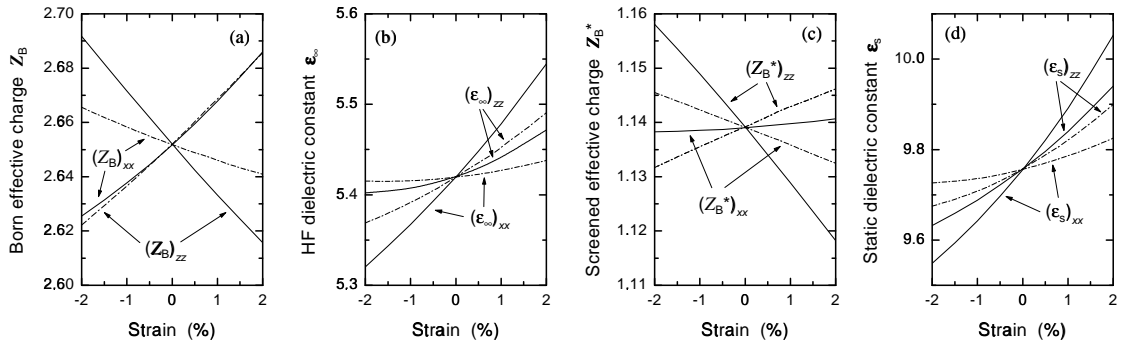
Figure 4.13 Tensor components (xx, zz) of (a) the Born effective charge Z_B, (b) the high-frequency dielectric constant ε_∞, (c) the screened effective charge Z_B^*, and (d) the static dielectric constant ε_s of 3C-GaN versus strain. Solid line: biaxial strain $\epsilon_\perp$, dot-dashed line: uniaxial strain $\epsilon_\parallel$.
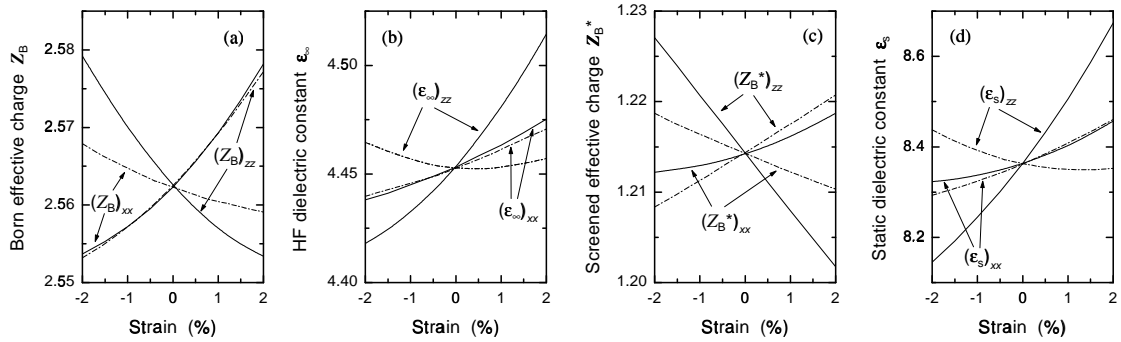

**Figure 4.14** Same as Fig. 4.13, but for 3C-AlN.

On the other hand, the variation with strain is smaller for AlN (note the different scales) and it turns out that the trend for the screened effective charge is nearly the same in 3C-GaN and -AlN. The difference remains, however, in the strain dependence of the static dielectric constant.

The Born and screened effective charges as well as the high-frequency and static dielectric constants behave rather similarly for 2H-GaN (as shown in Fig. 4.15) and 2H-AlN (as shown in Fig. 4.16), at least considering the sign of the linear strain coefficients for biaxial or uniaxial strain (cf. Table 4.6). The most significant exceptions concern the zz component both of the Born charge and of the static dielectric constant versus uniaxial strain. Both show a monotonous increase with strain for GaN, whereas a decrease is observed for AlN. For uniaxial strain, also the xx component of the Born charge behaves contrary in GaN and AlN.

Mostly, the quantities in Figs. 4.15 and 4.16 behave more or less different with respect to biaxial or uniaxial strain. The main reason is the opposite effect of the strains parallel and perpendicular to the c axis. For GaN, the components of the high-frequency (HF) dielectric constant nearly follow the behavior of the corresponding bond lengths (parallel as well as nearly perpendicular to the c axis). The same trend holds for AlN but is much less pronounced. The in-plane tensor components of the screened effective charges for both GaN and AlN are rather insensitive to both biaxial and uniaxial strain. On the other hand, the zz components show opposite trends with biaxial or uniaxial strain. For GaN this is due to the opposite trends of $(\varepsilon_\infty)_{zz}$, whereas for AlN this originates from the behavior of $(Z_B)_{zz}$.
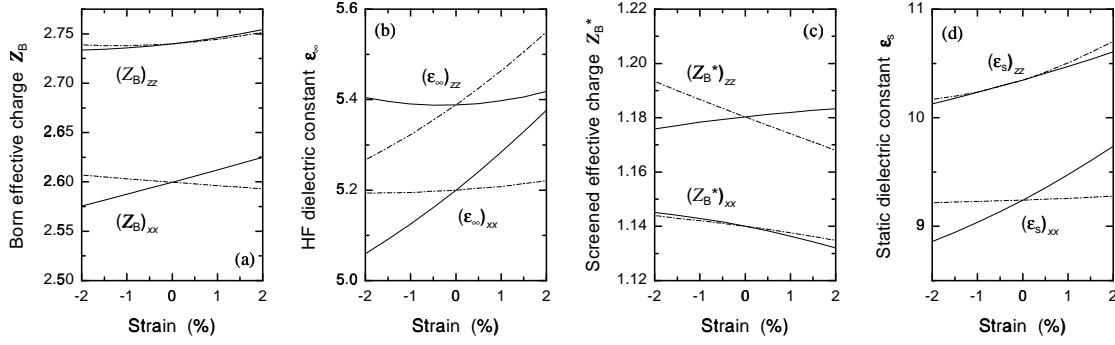
Figure 4.15 Tensor components (xx, zz) of (a) the Born effective charge $\mathbf{Z}_\mathrm{B}$, (b) the high-frequency dielectric constant $\boldsymbol{\varepsilon}_\infty$, (c) the screened effective charge $\mathbf{Z}_\mathrm{B}^*$, and (d) the static dielectric constant $\boldsymbol{\varepsilon}_\mathrm{s}$ of 2H-GaN versus strain. Solid line: biaxial strain $\epsilon_\perp$, dot-dashed line: uniaxial strain $\epsilon_\parallel$.
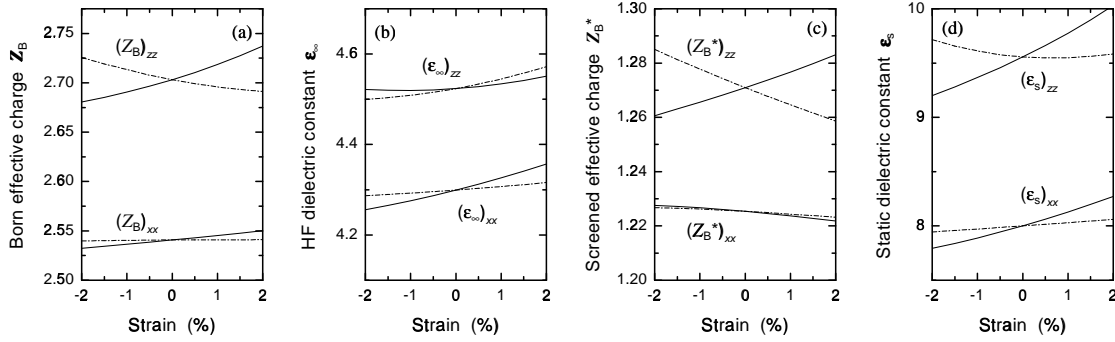
Figure 4.16 Same as Fig. 4.15, but for 2H-AlN.

Table 4.6 Calculated strain-free values X_0 as well as linear and quadratic strain coefficients $\frac{1}{X_0}\left(\frac{\partial X}{\partial \epsilon_{\perp/\parallel}}\right)_0$, $\frac{1}{X_0}\left(\frac{\partial^2 X}{\partial \epsilon_{\perp/\parallel}^2}\right)_0$ of tensor components of dielectric properties ($X = \mathbf{Z}_\mathrm{B}$, $\mathbf{Z}_\mathrm{B}^*$, $\boldsymbol{\varepsilon}_\infty$, $\boldsymbol{\varepsilon}_\mathrm{s}$, $\Delta\boldsymbol{\varepsilon}$) of the wurtzite nitrides. First value: linear coefficient, second value: quadratic coefficient.

property		2H-GaN					2H-AlN			
X	X_0	($\epsilon_\perp$)		($\epsilon_\parallel$)		X_0	($\epsilon_\perp$)		($\epsilon_\parallel$)	
$(Z_\mathrm{B})_{xx}$	2.60	0.474	0.011	-0.133	0.006	2.54	0.175	0.010	0.011	-0.005
$(Z_\mathrm{B})_{zz}$	2.74	0.189	0.076	0.125	0.096	2.70	0.521	0.106	-0.319	0.098
$(Z_\mathrm{B}^*)_{xx}$	1.14	-0.287	-0.065	-0.198	-0.027	1.23	-0.119	-0.028	-0.073	-0.017
$(Z_\mathrm{B}^*)_{zz}$	1.18	0.157	-0.031	-0.536	0.016	1.27	0.441	0.036	-0.519	0.034
$(\varepsilon_\infty)_{xx}$	5.20	1.525	0.176	0.129	0.068	4.30	0.588	0.081	0.170	0.025
$(\varepsilon_\infty)_{zz}$	5.39	0.062	0.214	1.309	0.184	4.52	0.160	0.140	0.399	0.134
$(\varepsilon_\mathrm{s})_{xx}$	9.24	2.371	0.308	0.161	0.031	8.00	1.493	0.194	0.363	0.007
$(\varepsilon_\mathrm{s})_{zz}$	10.35	1.158	0.093	1.287	0.432	9.56	2.159	0.308	-0.339	0.489
$(\Delta\varepsilon)_{xx}$	4.04	3.460	0.240	0.201	-0.008	3.70	2.544	0.162	0.588	-0.007
$(\Delta\varepsilon)_{zz}$	4.96	2.347	-0.019	1.262	0.351	5.04	3.956	0.229	-1.002	0.404

Apart from the in-plane components of the dielectric constants as functions of uniaxial strain, the other dielectric components in Figs. 4.15 and 4.16 (right panels) as well as in Table 4.6 (lower part) indicate remarkable changes induced by strain. Outstanding examples are the static dielectric constants and $(\varepsilon_\infty^{GaN})_{xx}$ versus biaxial strain. They possess the largest strain coefficients of all quantities considered. Apart from $(\varepsilon_s)_{zz}$ of AlN in the case of uniaxial distortions the strain coefficients in Table 4.6 are positive. However, some components exhibit a rather nonlinear behavior. This holds in particular for $(\varepsilon_\infty)_{zz}$ versus biaxial strain and $(\varepsilon_s)_{zz}$ versus uniaxial strain.

The lattice contributions to the static polarizabilities of the group-III nitrides are given by

$$(\Delta\varepsilon)_{\alpha\alpha} = (\varepsilon_s)_{\alpha\alpha} - (\varepsilon_\infty)_{\alpha\alpha} = \frac{2e^2(Z_B)^2_{\alpha\alpha}}{\varepsilon_0 V \mu \omega^2_{TO}(\alpha)}. \tag{4.3}$$

This expression follows from a combination of relations (3.4) and (3.3). For the nitrides the relative contribution of the lattice to ε_s is unusually large (approximately 50 %), being about 1.5 times stronger than for SiC. Furthermore, the difference between the xx and the zz components is strongly enhanced for the static one compared to the HF dielectric constant, i. e., the anisotropy is much larger for ε_s than for ε_∞. This is due to the different LO–TO splittings for the A_1 and the E_1 phonon modes (see next section). The variation of the lattice polarizability for both directions $\alpha = x$ and z is relatively weak for uniaxial strain (cf. Table 4.6). However, the linear coefficients for biaxial strain approach relatively large values as do already the coefficients of the dielectric constants themselves. That implies a remarkable increase of the lattice polarizability with rising values of tensile biaxial strain.

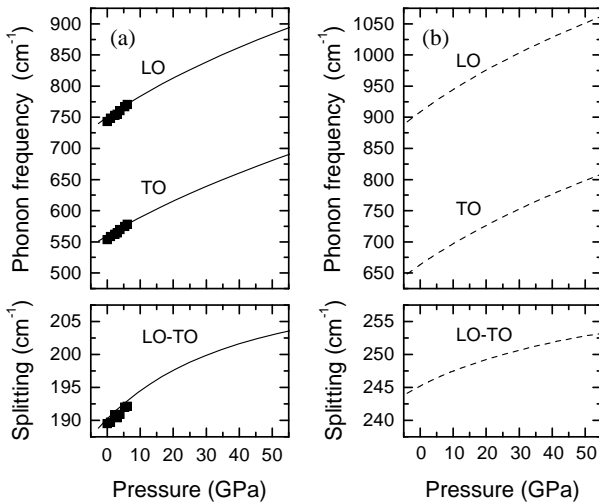## 4.5 Zone-Center Phonon Frequencies

4.5.1 Hydrostatic Pressure

The pressure dependence of the zone-center LO and TO phonon frequencies is shown in Fig. 4.17 for the cubic polytypes 3C-GaN (a) and 3C-AlN (b). In the lower part their differences are plotted. There is a monotonous increase from the zero-pressure values $\omega_{LO} = 750$ (907) cm^{-1}, $\omega_{TO} = 560$ (662) cm^{-1}, and $\omega_{LO} - \omega_{TO} = 190$ (245) cm^{-1} for GaN (AlN) with rising hydrostatic pressure. In the low-pressure region the calculations essentially reproduce the Raman measurements for 3C-GaN [*Sie97*, *Kar98*]. The physics of this behavior can be explained using a description with elastic bond-stretching and bond-bending forces within a Keating model [*Kea66*] and, respectively, of the Coulomb forces by an Ewald summation technique [*Sri90*]. The two characteristic zone-center frequencies follow within this model as [*Gri00*]

$$\omega^2_{LO/TO}(\Gamma) = \left(\frac{1}{M_c} + \frac{1}{M_N}\right)\left(4\alpha + 4\beta + c_{LO/TO}\hat{f}\right) \tag{4.4}$$

with the cation mass M_c, the nitrogen mass M_N, the radial (α) and angular (β) force constant of the Keating model, $c_{LO} = 2/3$, $c_{TO} = -1/3$, and the Coulomb force constant

$$\hat{f} = \frac{e^2 Z_B^2}{\varepsilon_0 \varepsilon_\infty V}. \tag{4.5}$$

Figure 4.17 Pressure dependence of the zone-center optical frequencies for the zinc-blende phase of (a) GaN and (b) AlN (upper panels). The difference of the optical phonon frequencies is plotted in the lower panels. The experimental results [*Sie97*] are indicated by filled squares.

The increase of ω_{LO} and ω_{TO} mainly follows the increase of the radial force constant $\alpha \sim 1/d^n$ with decreasing bond length d but is modified by the increase of the Coulomb force constant.

The increase of the LO–TO splittings of $3C$-GaN and $3C$-AlN in Fig. 4.17 is in contrast to the behavior of most of the other III-V semiconductors including BN [*San83*]. The reason is the net pressure effect discussed above for the screened ion charge. The effect of the increase of Z_{B}^* (cf. Fig. 4.9) is enhanced by the effect of the factor $1/V$ in the Coulomb force constant in Eq. (4.5). Therefore, although the LO–TO splitting of GaN and AlN increases, these materials become less ionic with pressure, in contrast to SiC [*Kar96*].

The pressure dependence of all zone-center modes in the wurtzite crystals is plotted in Fig. 4.18. Generally, with the exception of the lower E_2 modes, the phonon frequencies increase with rising pressure for reasons that have already been discussed in the zinc-blende case. The agreement with the pressure dependences found experimentally is reasonable. It is remarkably improved considering the LO–TO splittings in the lower panels of Fig. 4.18.

Over the whole pressure range plotted in Fig. 4.18, there is a remarkable difference between $2H$-GaN and $2H$-AlN concerning the A_1 and the B_1 modes. They show a significant drop in their pressure sensitivity for AlN, or even a saturation-like behavior. The excitation of these modes is accompanied by atomic displacements along the c axis. Consequently, the high-pressure behavior is related to the structural changes as discussed for the internal parameter u.

The increasing LO–TO splitting, which is observed theoretically and experimentally for both nitrides (cf. the lower parts of Fig. 4.18), is due to the pressure behavior of the corresponding components of the dynamic effective charge tensor and of the dielectric constant, respectively, where the zz components apply to the modes with A_1 symmetry and the xx components to those with E_1 symmetry. By comparison with the results for the zinc-blende case in Figs. 4.10 and 4.11, one derives the same interpretation also for the wurtzite case. The screening of the decreasing dynamic charge is reduced, and the increasing LO–TO splitting is not due to an increase in ionicity. The present results are in contrast to the experiments of Perlin et al. [*Per99*]. They found a decreasing splitting of the A_1 modes in $2H$-GaN. However, their LO and TO modes were measured independently from two different samples, whereas the experimental results cited here were obtained from the same sample [*Sie97*].
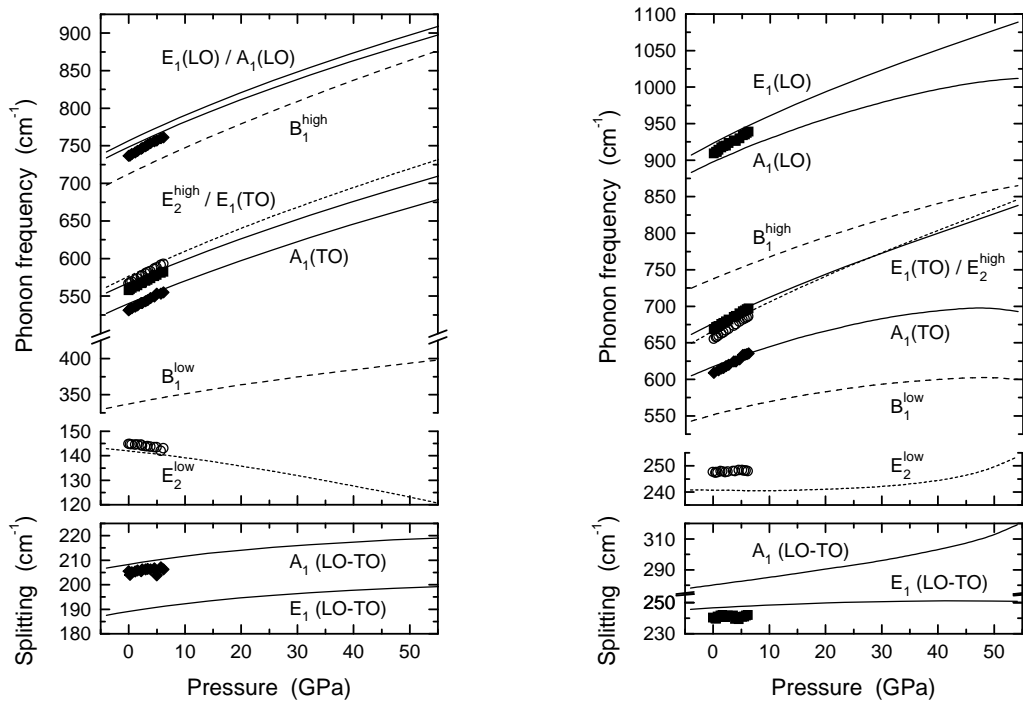
Figure 4.18 Pressure dependence of the zone-center optical frequencies for wurtzite GaN (left panels) and AlN (right panels). In addition, the difference of LO and TO phonon frequencies of the same symmetry are shown (lower parts). Experimental results [*Sie97*, *Sie98*] are included for comparison (filled diamonds – A_1 modes, open circles – E_2 modes, filled squares – E_1 modes).

The anomalous variation of the lower E_2 frequencies is a consequence of the interplay of the Ewald and the Hartree energy. Figure 4.19 shows that for the E_2^{high} mode, upon a displacement of the atoms, the Ewald energy causes the total energy to increase, whereas the Hartree contribution causes it to decrease; the opposite holds for the E_2^{low} mode, Fig. 4.20. This means that the high-frequency E_2 mode is stabilized by the Ewald energy and that the Hartree contribution destabilizes this mode. As a net effect, under hydrostatic pressure for the E_2^{high} mode the stabilizing influence increases more than the destabilizing one, so that the frequency increases.

For the E_2^{low} mode, Fig. 4.20 shows that the influence of E_{Hartree} and E_{Ewald} is reversed, so that now the Ewald contribution has a destabilizing influence. We note that the mode patterns shown in Fig. 3.2 exhibit a characteristic difference: For the high-frequency E_2 mode, the atoms of a cation-anion pair arranged parallel to the c axis are displaced to the same side, whereas for the low-frequency E_2 mode they are displaced in opposite directions. Since also for the E_2^{low} mode the pressure dependence of the Ewald energy is the most pronounced one, the phonon frequency of the E_2^{low} mode is reduced under pressure as much as this destabilization is not compensated for by the other energy contributions. In GaN one has only a partial compensation due to the band-structure energy and the Hartree contribution, and the frequency decreases under pressure. In AlN, first, the destabilizing influence of the Ewald energy is less marked than in GaN, and second, there is a net cancellation of all contributions, so that a very weak pressure dependence of this mode results.
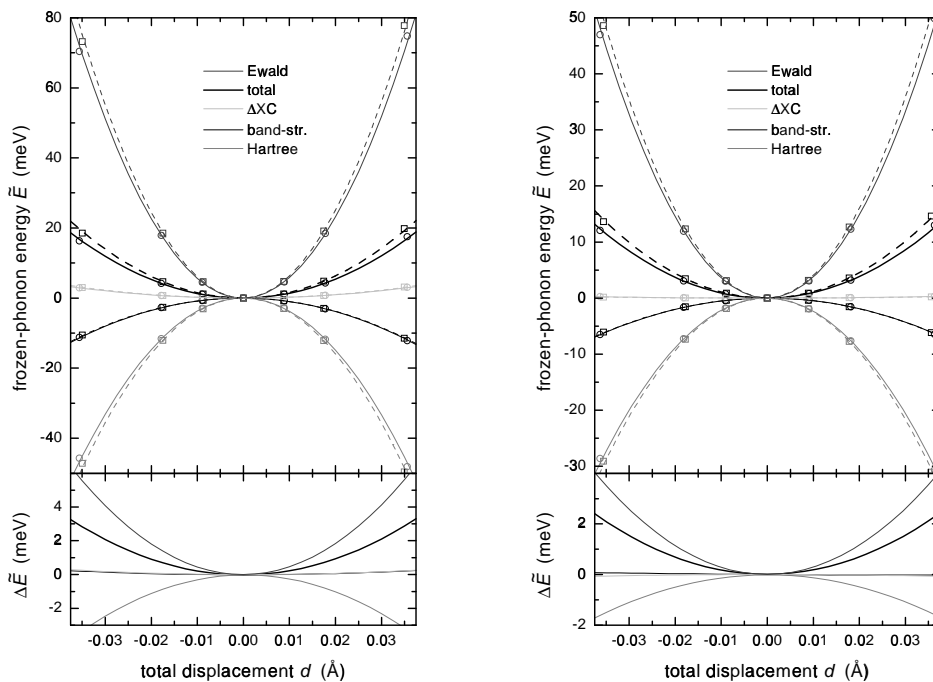
Figure 4.19 Frozen-phonon energy contributions vs total displacement for the E_2^{high} mode (upper parts). Left panel: GaN, right panel: AlN. The solid and dashed lines are fits [using Eq. (2.76)] to the five data points (circles and squares) close to $d = 0\,\text{Å}$. Solid lines and open circles: $p = 0\,\text{GPa}$, dashed lines and open squares: $p = 14\,\text{GPa}$. In the lower parts, the pressure-induced difference ΔE (of the fitting curves) is shown. Note the different scaling of the ordinates for GaN and AlN.
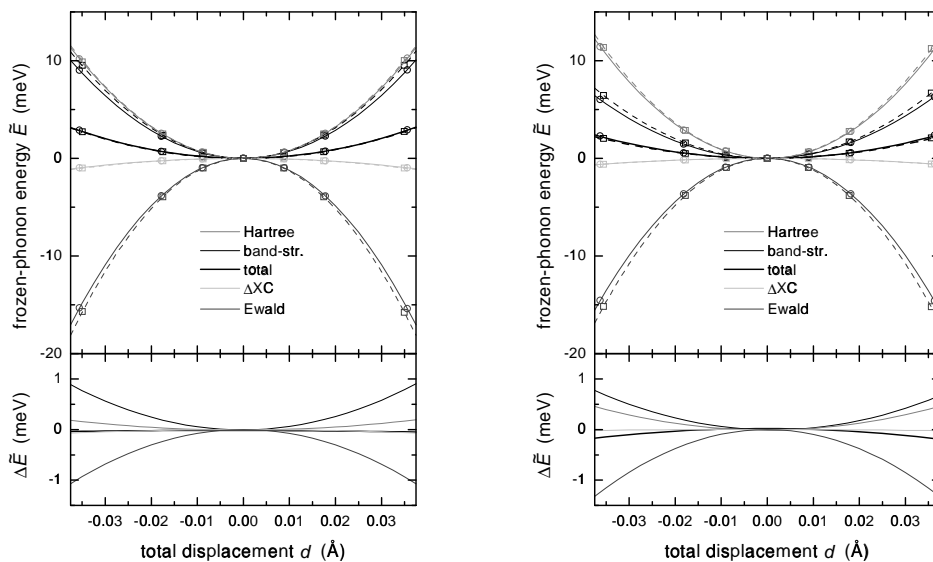
Figure 4.20 As in Fig. 4.19, but for the E_2^{low} mode. Here, the ordinates are scaled identically for GaN (left) and AlN (right).
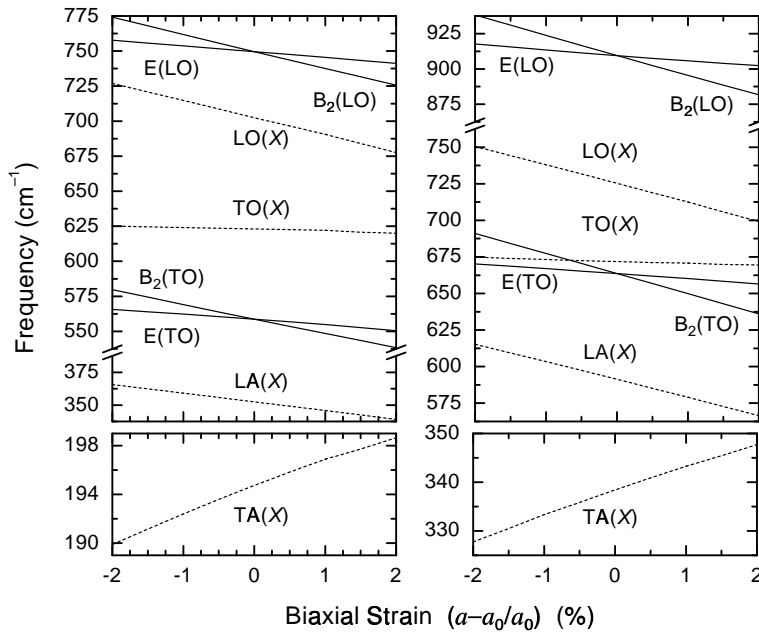
Figure 4.21 Phonon frequencies of 3C-GaN (left panels) and 3C-AlN (right panels) versus biaxial strain. Solid lines: zone-center modes; dotted lines: X-point modes.

4.5.2 Uni- and Biaxial Strain

The biaxial strain dependence of the zone-center phonon frequencies of 3C-GaN and 3C-AlN is plotted in Fig. 4.21, and the dependence on uniaxial strain is given in Fig. 4.22. Due to the tetragonal symmetry, the TO modes split into B_2 and E modes according to their polarization, with atomic displacements along the c axis for the B_2 modes and with those in the xy plane for the E modes.

The strain dependence of the zone-center phonon frequencies of 2H-GaN and 2H-AlN is plotted in Fig. 4.23. There is a general tendency in the strain dependence for all modes under consideration except from the lower E_2 modes. With rising *compressive* strain the mode frequencies increase as was already observed for hydrostatic pressure. Here, it occurs for biaxial
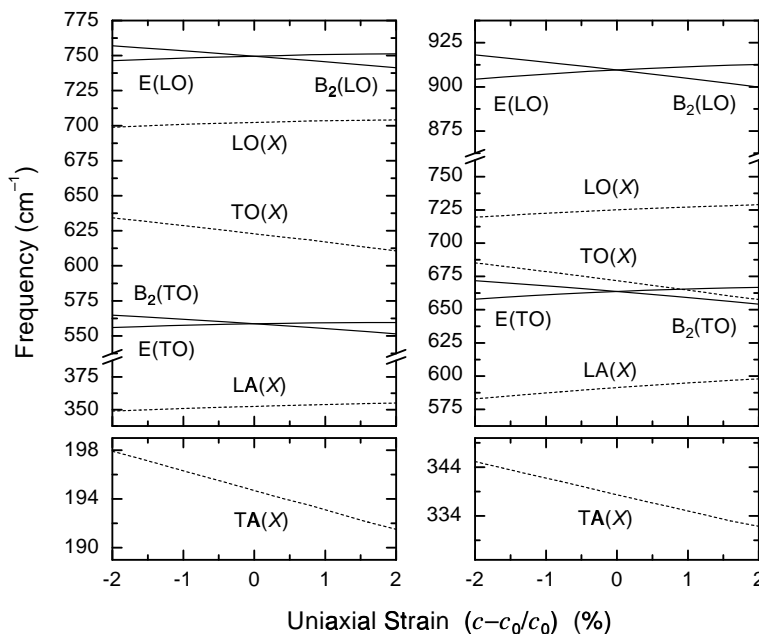

Figure 4.22 Phonon frequencies of 3C-GaN (left panels) and 3C-AlN (right panels) versus uniaxial strain. Solid lines: zone-center modes; dotted lines: X-point modes.

Figure 4.23 Zone-center phonon frequencies of 2*H*-GaN (left panels) and 2*H*-AlN (right panels) versus biaxial strain $\epsilon_\perp$ (solid line) and uniaxial strain $\epsilon_\parallel$ (dot-dashed line). In addition, the LO–TO and anisotropy-related splittings are given.

and uniaxial distortions, but with different strength. In general, the strain variations are larger in the biaxial case compared to the uniaxial one. However, the A_1(TO) and B_1^{low} modes in AlN remain nearly unaffected by uniaxial strain. Closer inspection reveals that they even show a weakly nonlinear behavior.

In the hydrostatic limit the effect can be explained by a general shortening of the bonds and, as a consequence thereof, an enlargement of the force constants. In the case of biaxial strain, i.e., a reduction of the *a*-lattice constant accompanied by a smaller increase of the *c*-lattice constant, this bond contraction happens mainly for the three bonds nonparallel to the *c* axis (cf. Fig. 4.7). Similarly, under compressive uniaxial strain the bonds are also shortened, but in particular the one parallel to the *c* axis (cf. Fig. 4.8). However, the change in unit cell volume that occurs along with these bond-length variations is much larger in the case of biaxial strain than for the uniaxial one, which partly accounts for the different magnitude of the frequency shifts.

The lower E_2 modes in Fig. 4.23 behave oppositely under biaxial and uniaxial strain. As under hydrostatic pressure, these modes are softened with rising *compressive* biaxial strain. For GaN, the experimentally determined phonon deformation potentials [*Dav97*] confirm the

positive sign of the biaxial mode coefficient, i. e., the mode softening. Recently, the shift of this mode to higher energy under tensile biaxial strain has been observed experimentally also for AlN [*Pro01*]. However, in the presence of uniaxial strain the behavior of the lower E_2 modes is "normal."

4.6 Phonon Mode Coefficients and Deformation Potentials

4.6.1 Hydrostatic Pressure

The low-pressure behavior of a phonon frequency is described by the mode Grüneisen parameter

$$\gamma_j = -\left.\frac{\partial \ln \omega_j}{\partial \ln V}\right|_{V=V_0} = B_0 \left.\frac{\partial \ln \omega_j}{\partial p}\right|_{p=0} \tag{4.6}$$

for a mode j with the frequency ω_j. Calculated and measured values are collected in Table 4.7 for the cubic crystals. The present calculation as well as the available linear-muffin-tin-orbital (LMTO) studies of the TO phonon [*Kim96*, *Gor95*] give larger Grüneisen parameters for GaN in comparison with AlN as a consequence of the stronger covalent bonding in AlN and, therefore, larger force constants $\alpha + \beta$ [cf. Eq. (4.4)]. Thereby, the present plane-wave results underestimate the experimental GaN values, whereas the LMTO treatments give too large a mode Grüneisen parameter γ_{TO}. A possible source for the discrepancy is the use of different bulk moduli B_0 in the determination of the Grüneisen parameters.

With the exception of those of the low-frequency E_2 modes, the mode Grüneisen parameters in Table 4.8 are positive. They are rather close to the value discussed in the zinc-blende case. This also holds for the larger GaN values, except for the high-frequency E_2 mode, where the Grüneisen parameter is slightly larger for AlN. One set of experimental values for 2H-AlN [*Per93a*] seems to fall off the common trend and should be used with care, especially since the authors do not confirm these results in a subsequent work [*Per93b*].

For the lower E_2 modes of 2H-GaN and 2H-AlN we find Grüneisen parameters that are negative or nearly zero in reliable agreement with the Raman measurements [*Sie97*, *Sie98*,

Table 4.7 Mode Grüneisen parameter γ_j for zinc-blende GaN and AlN. Other calculated and experimental values are also given. Besides values for zone-center modes also those of phonons at the zone-boundary (L point) are listed for comparison with zone-center wurtzite modes.

	Reference	LO(Γ)	TO(Γ)	LO(Γ)$-$TO(Γ)	LO(L)	TO(L)	LA(L)	TA(L)
3C-GaN	present	1.02	1.19	0.5	1.05	1.23	0.92	-0.49
	calc. [*Kim96*]		1.8					
	calc. [*Gor95*]		1.52					
	exper. [*Sie97*]	1.20	1.4	0.5				
3C-AlN	present	0.89	1.14	0.2	0.96	1.31	0.85	-0.29
	calc. [*Kim96*]		1.5					
	calc. [*Gor95*]		1.42					

Table 4.8 Mode Grüneisen parameter γ_j for the zone-center phonons in wurtzite GaN and AlN. Other calculated and experimental values are given for comparison.

	Reference	E_1(LO)	A_1(LO)	E_2^{high}	E_1(TO)	A_1(TO)	E_2^{low}
2*H*-GaN	present	0.99	0.98	1.28	1.19	1.21	−0.35
	calc. [*Gor95*]			1.60	1.48	1.52	−0.20
	exper. [*Sie97*]		1.20	1.50	1.41	1.51	−0.4
	exper. [*Per93a*]			1.80	1.61	1.18	−0.43
2*H*-AlN	present	0.91	0.82	1.34	1.18	1.02	−0.02
	calc. [*Gor95*]			1.66	1.48	1.50	−0.28
	exper. [*Sie98*]	1.06		1.58	1.41	1.51	0.1
	exper. [*San83*]	1.0	1.0		1.6	1.6	
	exper. [*Per93a*]	1.65		2.38		1.48	≈ 0
	exper. [*Per93b*]	0.38; 0.4		1.26; 1.34		1.58; 1.68	≈ 0

Per93a, *Per93b*]. According to the folding relationship between points in the zinc-blende and wurtzite Brillouin zones, the E_2^{low} modes at Γ in wurtzite correspond to TA(L) modes of the zinc-blende structure. This is reflected by the fact that the Grüneisen parameter of the TA(L) modes $\gamma_{\text{TA}(L)} = -0.5$ and -0.3 for 3*C*-GaN and 3*C*-AlN, respectively, have the same sign and ordering as those of the corresponding E_2 modes of the wurtzite structures.

4.6.2 Uni- and Biaxial Strain

The linear strain coefficients [cf. Eq. (2.113)] $K_{\perp/\parallel}(j)$ (in cm^{-1}) of the wurtzite nitrides are listed in Table 4.9. In addition, in this table the linear stress coefficients $\widetilde{K}_{\perp/\parallel}(j)$ per unit stress (i.e., in units of cm^{-1}/GPa) are given. They are obtained from the strain coefficients $K_{\perp/\parallel}(j)$ using the calculated elastic stiffness constants presented in Table 4.4. For GaN, these coefficients are compared with experimental results for $j = E_2^{\text{low}}$, A_1(TO), E_1(TO), E_2^{high}, and A_1(LO) [*Dav97*, *Dem96*, *Kis96*, *Klo98*, *Age98*, *Wie00*]. For GaN, several experimental deformation potentials and stress coefficients exist for the E_2^{high} mode. In general, very good agreement is obtained with the coefficients measured by Davydov *et al.* [*Dav97*]. This holds not only for the E_2^{high} but also for other modes, in particular for E_1(TO). For the stress coefficient of this mode, another experimental result [*Wie00*] shows very good agreement when a larger set of samples is used for fitting, which then covers a wider strain range.

It is important to notice that the originally published experimental biaxial mode coefficients only seldom are the directly measured data. Either the published values are already converted to stress coefficients via elastic stiffness constants [*Kis96*, *Age98*, *Pro01*, *Wie00*], or the mode coefficients were reconstructed from phonon deformation potentials [*Sar02*, *Gle03*] which have been obtained by means of additional mode pressure coefficients (or Grüneisen parameters), or both conversions have been made [*Dem96*, *Dav97*]. Due to these varying procedures, additional errors are introduced to the results. On the other hand, in [*Klo98*] no such conversions have been employed, and the strain coefficient is given only with respect to ϵ_{zz}, since the vari-

Table 4.9 Linear coefficients per unit strain, $K_{\perp/\parallel}(j)$ (in cm^{-1}), or per unit stress, $\widetilde{K}_{\perp/\parallel}(j)$ (in cm^{-1}/GPa), of the zone-center vibrational modes j of 2H-GaN and 2H-AlN. The last two columns give values for the LO-TO splittings. The obtained biaxial coefficients are compared with experimental results. [a–i] In some works the biaxial strain coefficient was obtained relative to the c-axis strain, ϵ_{zz}, and not to the in-plane strain, $\epsilon_\perp$. For clarity, here the originally measured data are listed and the necessary conversion is indicated by the additional factor R_c^b. Where appropriate, the experimental coefficients are recalculated to correct for a wrong conversion formula or deviating values of the elastic stiffness constants. The resulting numbers are given in parenthesis. The values in braces are obtained from a fit that covers a wider strain range.[c]

	E_2^{low}	B_1^{low}	$A_1(\text{TO})$	$E_1(\text{TO})$	E_2^{high}	B_1^{high}	$A_1(\text{LO})$	$E_1(\text{LO})$	LO$-$TO A_1	E_1
2H-GaN										
$K_\perp(j)$	154	-527	-931	-1139	-1115	-836	-885	-1198	46	-59
	240[a]		-671[a]	-1341[a]	-1293,[a]		$-191\,(-842)$[b]			
					$-693\,(-1214)$,[b]					
					$-2632\,R_c^b\,(-1395)$,[d]					
					$-2537\,R_c^b\,(-1345)$[e]					
$K_\parallel(j)$	-24	-149	-443	-300	-418	-696	-618	-389	-175	-89
$\widetilde{K}_\perp(j)$	0.33	-1.14	-2.01	-2.46	-2.41	-1.81	-1.91	-2.59	0.10	-0.13
	0.5[a]		-1.4,[a]	-2.8[a]	-2.7[a],		$-0.8\,(-1.8)$[b]			
			$-3.0\,\{-2.1\}$[c]		$-3.9\,\{-3.3\}$,[c]					
					$-2.9\,(-2.5)$,[b]					
					$-4.2\,(-2.9)$,[d]					
					$-4.8\,(-2.8)$,[e]					
					-2.4[f]					
$\widetilde{K}_\parallel(j)$	-0.06	-40	-1.19	-0.80	-1.12	-1.87	-1.67	-1.04	-0.47	-0.24
2H-AlN										
$K_\perp(j)$	439	-1047	-1330	-1208	-1198	-738	-1038	-1233	292	-25
					$-4398\,R_c^b\,(-2239)$,[g]					
			-1396[i]	-1502[i]	-1689[i]		-692[i]			
$K_\parallel(j)$	-288	40	-70	-391	-532	-516	-434	-442	-355	-51
$\widetilde{K}_\perp(j)$	0.94	-2.23	-2.84	-2.58	-2.55	-1.57	-2.21	-2.63	0.62	-0.05
					$-6.3\,(-4.4)$,[g]					
					-3[h]					
			-2.8[i]	-3.0[i]	-3.4[i]		-1.4[i]			
$\widetilde{K}_\parallel(j)$	-0.89	0.12	-0.22	-1.21	-1.65	-1.60	-1.35	-1.37	-1.10	-0.16

[a] cf. [*Dav97*]. [d] cf. [*Kis96*]. [g] cf. [*Pro01*].

[b] cf. [*Dem96*]. [e] cf. [*Klo98*]. [h] cf. [*Sar02*].

[c] cf. [*Wie97*] and [*Wie00*]. [f] cf. [*Age98*]. [i] cf. [*Gle03*].

ation of the lattice constant c is measured. For this result, a correction is necesssary due to another source of error that occasionally occurs in the published values for $\widetilde{K}_\perp$, which consists of the use of a wrong relation [*Rie96*] between $\sigma_\perp$ and ϵ_{zz}. Furthermore, in [*Kis96*] isotropic elastic moduli have unnecessarily been extracted from the stiffness constants according to the Voigt average [*Voi10*], which applies only to polycrystalline samples that consist of crystallites having arbitrary orientation. Therefore, it has to be noticed that the published values in several cases depend on the procedure and the parameter sets used for their extraction from the "raw" experimental data. For instance, the results for 2*H*-AlN [*Pro01*] were obtained using elastic constants [*Dav98*] that yield wrong values for the elastic relaxation coefficients. Instead, if one employs the results of McNeil *et al.* [*McN93*] for the elastic constants, the value of the mode coefficient for the high-frequency E_2 mode of AlN is considerably lowered [*Pro01*]. But still, the agreement between the experimental and the theoretical result is not complete.

In several papers the measured frequency shift versus the *c*-axis strain, $\Delta\omega/\epsilon_{zz}$, is given explicitly. Therefore, to minimize the influence of additional errors we prefer to list these original data in Table 4.9 where possible. They are identified by the necessary conversion factor R_c^{b}, which has been added for consistency. In order to avoid the influence of different formulas and elastic constants, the stress coefficients were partly recalculated from the originally measured data, using measured elastic stiffness constants for both GaN [*Pol96*] and AlN [*McN93*]. The reevaluation brings the experimental results rather close to the calculated ones. This holds especially for the biaxial strain coefficients and the accompanying stress coefficients for the E_2^{high} and A_1(LO) modes of GaN. For these modes the agreement can be considered to be excellent. In general, comparing the calculated and measured coefficients for GaN and considering the uncertainties of the experimental results and the variations among the different measurements, the agreement between theory and experiment in Table 4.9 is very satisfactory. The data confirm the weak dependence on the mode symmetry. The considerable lowering of the value of the stress coefficient of the E_2^{high} mode of GaN due to the recalculation implies that by using the Raman shift of this mode as a measure for the biaxial strain, up to now the accompanying stress has been underestimated.

Sometimes, in the case of a biaxially strained crystal a relation of the frequency shift to the relative volume change, $\Delta\omega(j) = -\omega_0(j)\gamma(j)\Delta V/V_0$, is used as an approximation, with the phonon frequency in the strain-free situation, $\omega_0(j)$, and the mode Grüneisen parameter, $\gamma(j)$. This relation is strictly valid only in the presence of hydrostatic pressure and, therefore, its application to the case of biaxial strain has to be justified. It simply means the use of $K'_\perp(j) = -\omega_0(j)\gamma(j)(2 - R_c^{\mathrm{b}})$ instead of $K_\perp(j) = 2a(j) - R_c^{\mathrm{b}}b(j)$. Since in terms of the phonon deformation potentials one has $K'_\perp(j) = [2a(j) + R_c^{\mathrm{h}}b(j)](2 - R_c^{\mathrm{b}})/(2 + R_c^{\mathrm{h}})$, for the nitrides under consideration, this "hydrostatic approximation" is only valid for those modes where the deformation potentials $a(j)$ and $b(j)$ are nearly equal. The calculated phonon frequency in the strain-free case and the deformation potentials are listed in Table 4.10. It can be seen that for GaN the criterion of nearly equal values for $a(j)$ and $b(j)$ is fulfilled only for the E_2^{high}, holds approximately for the A_1(TO) and E_1(LO), but fails for the E_2^{low}, E_1(TO), and A_1(LO) mode. From the experimentally determined mode Grüneisen parameter [*Goñ01*], $\gamma(E_2^{\mathrm{high}}) = 1.50$, the measured zero-pressure frequency [*Goñ01*], $\omega_0(E_2^{\mathrm{high}}) = 567.0\,\mathrm{cm}^{-1}$, and the relaxation coefficient resulting from the elastic constants of Polian *et al.* [*Pol96*], the numerical value of $K'_\perp(E_2^{\mathrm{high}}) = -1248\,\mathrm{cm}^{-1}$ is obtained. Using again the elastic constants from [*Pol96*], this

Table 4.10 Phonon deformation potentials $a(j)$ and $b(j)$ (in cm^{-1}) for wurtzite GaN and AlN. Additionally, the resulting isotropic and shear deformation potentials, $K^{\text{iso}}(j) = 2a(j) + b(j)$ and $K^{\text{sh}}(j) = 2[a(j) - b(j)]$, are given. The mode frequencies $\omega(j)$ (in cm^{-1}) calculated in the strain-free case are also listed.

		E_2^{low}	B_1^{low}	A_1(TO)	E_1(TO)	E_2^{high}	B_1^{high}	A_1(LO)	E_1(LO)
2H-GaN	$\omega(j)$	142	337	540	568	576	713	748	757
	$a(j)$	78	−335	−645	−715	−736	−666	−667	−774
	$b(j)$	2	−275	−679	−598	−720	−926	−870	−708
	$K^{\text{iso}}(j)$	158	−945	−1969	−2028	−2192	−2258	−2204	−2256
	$K^{\text{sh}}(j)$	151	−120	68	−234	−32	520	406	−132
2H-AlN	$\omega(j)$	241	552	618	677	667	738	898	924
	$a(j)$	148	−573	−765	−841	−886	−596	−731	−870
	$b(j)$	−221	−196	−393	−745	−906	−764	−737	−808
	$K^{\text{iso}}(j)$	75	−1342	−1923	−2427	−2678	−1956	−2199	−2548
	$K^{\text{sh}}(j)$	738	−754	−744	−192	40	336	12	−124

corresponds to a value of the stress coefficient of $-2.6\,\text{cm}^{-1}/\text{GPa}$, which indeed approaches the calculated value given in Table 4.9. Therefore it is surprising that by using this approximation, a value of $-3024\,\text{cm}^{-1}R_c^{\text{b}}$ has been obtained for the biaxial strain coefficient of this mode [*Gie89*]. This is probably due to a mode Grüneisen parameter which is too large, since it was derived using a bulk modulus of 245 GPa [*Per92*].

Chapter 5

Short-Period GaN/AlN Superlattices

In this chapter, we investigate the influence of composition and layered ordering on the structural and vibrational properties of short-period GaN/AlN superlattices (SLs), formed either in the cubic [001] or the hexagonal [0001] direction. The motivation for these studies is twofold: Basic information about the properties of these structures is needed to support the use of Raman and IR spectroscopy for material characterization, and short-period superlattices are chosen since their growth results in a homogeneously strained structure, making it suitable for various applications.

The focus of this chapter is on the general properties and the physical peculiarities of the phonons in the nitride SLs, since the numerically rather demanding calculations for the larger cells allow to draw mainly qualitative conclusions.

5.1 Structural Properties

5.1.1 Symmetry and Relaxation

In general, an $m \times n$ SL composed of two binary materials A and B consists of alternating layers containing m atomic bilayers of material A and n atomic bilayers of material B. Independent of the symmetry of the SL, this is denoted as $A_m B_n$. A pseudomorphic $m \times n$ SL based on zinc-blende bulk materials stacked along the [001] direction has tetragonal symmetry. More precisely, if $m + n$ is an even number, the symmetry is simple tetragonal with space group D_{2d}^5 ($P\bar{4}m2$), but if it is an odd number, the symmetry is body-centered tetragonal with space group D_{2d}^9 ($I\bar{4}m2$) [Sap83]. In both cases, the atomic basis of the SL, viewed as a bulk crystal, consists of $N_b = 2(m + n)$ atoms. For a pseudomorphic wurtzite-based $m \times n$ SL stacked along [0001], the situation is significantly different: If $m + n$ is an even number, the SL has hexagonal symmetry with the symmorphic space group C_{3v}^1 ($P3m1$), whereas if it is an odd number, the SL has hexagonal symmetry with the nonsymmorphic space group C_{6v}^4 ($P6_3mc$) [Kit98]. In the first case, the atomic basis of the SL consists of $N_b = 2(m + n)$ atoms, whereas in the second case, in order to have translational invariance along [0001], a fractional translation is needed, making the atomic basis twice as large, i.e., $N_b = 4(m + n)$. This already holds for the $2H$ structure of a binary compound like GaN or AlN with four atoms in the unit cell, since it corresponds to $m = 1$ and $n = 0$. As a consequence, the unit cell of, e.g., an h-(1×1)-[0001] SL contains four atoms, as does the corresponding one of a c-(1×1)-[001] SL (where, for clarity, "h" indicates
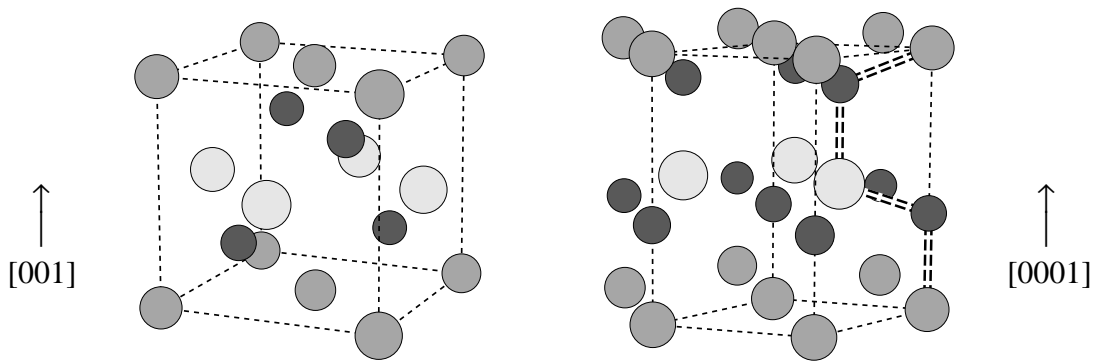
Figure 5.1 Atomic structure of $(AlN)_1(GaN)_1$ superlattices (schematic). Medium and light gray symbols: group-III atoms, dark gray symbols: nitrogen atoms. Left: cubic [001] stacking; the dashed lines indicate a conventional unit cube (cf. Fig. 2.1). Right: hexagonal [0001] stacking; the dashed lines indicate a conventional $2H$ cell, whereas the dashed double line connects the basis atoms belonging to the indicated cell (cf. Fig. 4.2). (By convention [*Amb98*], the [0001] direction is given by a vector pointing from a group-III atom to the nearest-neighbour N atom along the c axis.)

a hexagonal and "c" a cubic-derived SL). Yet for an h-$(AlN)_2(GaN)_1$-[0001] SL the unit cell contains six anion-cation layers, i.e., it is given by $2[(AlN)_2(GaN)_1]$, whereas in the unit cell of the corresponding c-(2×1)-[001] SL there are only three such layers.

Due to the lowered symmetry, there are more internal degrees of freedom in the atomic arrangement for the SLs than for the bulk crystals. These have to be taken into account in the relaxation of the lattice when minimizing the total energy for a given structure and a given in-plane lattice constant by varying the atomic positions along the stacking direction. For both cubic and hexagonal SLs studied here, the main internal degree of freedom is the relative height of the AlN and GaN parts of the SL cell. The atomic arrangement within each material layer, however, is much more strictly governed by symmetry for the cubic than for the hexagonal SLs. In the cubic 1×1 SL, there is no additional degree of freedom, since there is a symmetry along the stacking direction: The layers are symmetric by means of a C_2 operation with axes of rotation perpendicular to the side faces of the cube shown in the left part of Fig. 5.1, positioned at the center atom of the respective material layer (which here are the cations). This symmetry is present in all c-$(m \times n)$-[001] SLs, so that — as in the bulk — there is no difference between the "up" and "down" directions. In higher-order cubic SLs, due to this C_2 symmetry, the internal relaxation is symmetric to the center of the respective material layer. On the contrary, for the hexagonal SLs, there is no additional symmetry constraint except for the fractional translation that applies to those SLs where $m+n$ is odd. This means that already for the h-(1×1)-[0001] SL, the atomic positions of all four basis atoms are "free," i.e., there is no symmetry constraint for them. This makes a full relaxation of the hexagonal SLs rather demanding. Therefore, this full relaxation is only taken into account for the smallest SLs ($m = n = 1$), whereas for the larger ones only the relative layer height has been relaxed.

To study the influence of strain on the superlattices, we consider three different lattice constants in the layer planes perpendicular to the stacking direction. These are those of (zinc-

blende/wurtzite) AlN and GaN bulk materials as well as an intermediary one determined by macroscopic elasticity theory as described in Sect. 2.6.3. The former ones correspond to the case that the (pseudomorphically strained) short-period SL is grown on a substrate, so that the in-plane lattice constant is determined by that of the substrate, whereas the latter case corresponds to a free-standing SL. For each in-plane lattice constant, an atomic arrangement according to the macroscopic elastic constants (cf. Sect. 4.3) was chosen as starting configuration for the relaxation. After relaxation, both the total height of the SL cell (c_{SL}) as well as the relative thickness of the two material layers were found to have changed in the following way: The relaxed total cell height is identical to the macroscopically calculated value. However, there is a trend for an increase of the GaN layer thickness at the expense of a reduced AlN one. This becomes most pronounced for the ultrathin c-(1×1)-[001] SLs. For the hexagonal [0001] structures similar deviations from the macroscopic predictions were found, but to a somewhat lesser extent than for the cubic SLs. In addition, the internal structural degrees of freedom have been relaxed for the h-(1×1) SLs. It turns out that the respective internal parameters u_{Ga} and u_{Al} behave in the *opposite* way to the known dependence on biaxial strain (as shown in Chapter 3), i.e., for increasing length of the c lattice parameter also u increases (and vice versa). The effect is nearly twice as large for AlN as for GaN.

In hexagonal SLs, a macroscopic electric field is created if the constituent layers differ in their spontaneous polarization. This is the case for GaN and AlN. Therefore, this field has to be taken into account. From macroscopic elasticity theory that includes the converse piezoelectric effect it is known that the internal field changes the elastic behaviour of the layers. Especially, the layer heights differ from their relaxed values obtained for zero field: The field causes the AlN layers to increase and the GaN layers to shrink in height [*Gle01*]. However, here we find exactly the opposite behaviour of the layer heights.

Altogether, this means that, in general, the macroscopic elasticity theory cannot describe well the atomic positions in a short-period GaN/AlN SL. One rather has to consider these structures as a sort of bulk material of its own kind: They represent ordered $Al_m Ga_n N_{m+n}$ alloys. For larger layers, it has of course to be expected that the bulk character of each material layer will dominate and will lead to the predicted macroscopic behaviour. Since in our study we are limited to short-period SLs, we however cannot give an estimate for the critical number of atomic bilayers that marks the transition between a "conventional SL" and an "ordered alloy."

5.1.2 Stability

To determine of the stability of the superlattices (in the limit $T \to 0$ K), we compare the total energies of the layered structures with the ones of the correspondingly strained (and also the fully relaxed) bulk materials. Thereby, we obtain the enthalpy of formation [*Mar86*] in dependence on a_{SL} as the energy gain either with respect to pseudomorphically strained bulk layers (relevant for epitaxial growth with layer thicknesses below the critical value) or with respect to relaxed bulk material (with thicknesses larger than the critical one):

$$\Delta H_f^{str}(a_{SL}) = E_{SL}(a_{SL}) - E_{GaN}(a_{SL}) - E_{AlN}(a_{SL}), \tag{5.1}$$

$$\Delta H_f^{unstr}(a_{SL}) = E_{SL}(a_{SL}) - E_{GaN}(a_{GaN}) - E_{AlN}(a_{AlN}), \tag{5.2}$$

Table 5.1 Enthalpy of formation for various short-period superlattices (in meV per anion-cation pair). The first value is the enthalpy for the strained case ($\Delta H_{\mathrm{f}}^{\mathrm{str}}$), the value in parenthesis is the enthalpy with respect to the fully relaxed bulk-like layers ($\Delta H_{\mathrm{f}}^{\mathrm{unstr}}$).

Superlattice	on AlN	elast. strained	on GaN
1×1			
cubic	-111 (-100)	-110 (-104)	-110 (-100)
hexagonal	265 (273)	-3 (3)	260 (273)
2×2			
cubic	-1 (12)	-1 (6)	-1 (10)
hexagonal	5 (17)	5 (11)	6 (17)

The total energy of the SL, E_{SL}, is taken per cation-anion pair, whereas the total energies of bulk-like layers, $E_{X\mathrm{N}}$ ($X =$ Ga, Al), are taken per atom. The lattice constants a_{SL}, a_{GaN}, and a_{AlN} indicate the strain state. Positive formation enthalpies indicate an instability of the SL against decomposition into a system with thicker GaN and AlN layers.

There has been quite some controversy about the stability of short-period superlattices with respect to the case of GaAs/AlAs structures [*Byl86*, *Woo87*, *She88*]. For the GaN/AlN SLs we find that the energy differences are well resolved and depend sensitively on the given strain and the number of bilayers in the SL period. The results are listed in Table 5.1. Formally, the data indicate large differences in the stability between zinc-blende- and wurtzite-derived SLs. Cubic GaN/AlN [001] 1×1 SLs are stable independently of the strain situation. However, already for 2×2 SLs a change occurs. Decomposition in thick unstrained layers of the constituents is possible. In the hexagonal cases, the situation is different. Only the 1×1 SLs can be stabilized against decomposition into thick strained layers for an in-plane lattice constant close to the average one. In all other cases a 1×1 SL is not an equilibrium structure. For larger SLs, the instability dominates. However, independent of polytype and strain state the absolute values of the enthalpy of formation are smaller than the thermal energy $k_{\mathrm{B}}T \approx 25$ meV at room temperature. Consequently, equilibrium conditions (as done so far) cannot give a complete answer. The possibility to grow such short-period SLs will depend on kinetic effects.

5.2 Phonon Modes of Short-Period SLs

Compared to the well-studied case of a GaAs/AlAs SL, the physical situation is remarkably different for a GaN/AlN SL: first, the layers are mutually strained due to different lattice constants, second, there is a partial overlap of the optical-phonon dispersions of the bulk materials, and, third, the common anion is the lightest atom. In this section, we investigate the consequences of these conditions for the phonon modes of short-period GaN/AlN SLs, stacked along the cubic [001] and the hexagonal [0001] direction.
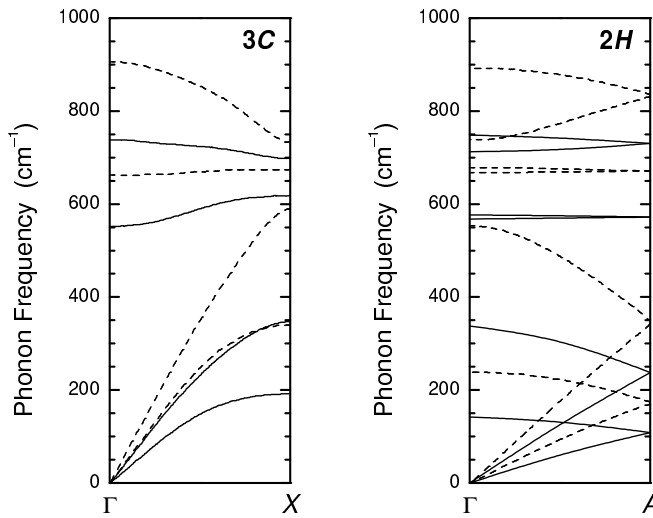
Figure 5.2 Phonon dispersions of bulk GaN (solid lines) and AlN (dashed lines). Left: Γ–X part for cubic polytypes. Right: Γ–A part for hexagonal polytypes.

5.2.1 General Aspects

The phonon modes of a short-period $m \times n$ SL can be viewed from two different perspectives: First, as for bulk materials, the number of phonon modes depends on the number of atoms that belong to the primitive cell, which depends on the symmetry of the SL as described in Sect. 5.1. Second, as for SLs with thicker layers, the phonons may be characterized as confined, propagating, and interface modes (as known for GaAs/AlAs SLs [*Ric87*]). Both views will help to classify and understand the phonon modes found in the nitride SLs studies here. They are investigated particularly with regard to their dependence on the in-plane strain and the propagation direction (as already discussed for the angular dispersion of the bulk phonon modes, Sect. 3.2.3).

The second perspective described above is based on a comparison of the bulk materials' phonon dispersion along the stacking direction of the SL. Since the enlargement of the atomic basis due to the SL stacking corresponds to a reduction of the Brillouin zone, effectively the phonon dispersions are folded along that direction. For cubic [001] stacking, this affects the (corresponding) Γ–X direction, whereas for hexagoal [0001] stacking, this affects the Γ–A direction. These parts of the dispersions are shown for unstrained bulk GaN and AlN in Fig. 5.2. Because of the different lattice constants of GaN and AlN the biaxial strain in the superlattice layers is compressive for GaN and tensile for AlN. As shown in Sect. 4.5.2, the phonon frequencies increase with increasing compressive strain. The only exception is the low-frequency E_2 mode of the wurtzite structure whose frequency decreases. The same holds for the zone-boundary TA phonons of the cubic nitrides. Therefore, due to the strain-induced shift of the bulk phonon dispersions, for any given in-plane lattice constant the partial overlap of the LO branches of GaN and AlN is enhanced for the SLs. At the same time, the energetical separation between all of the LO and the TO modes increases, and one can expect the TO modes region to be split into confined AlN and GaN phonons. Because of the opposite strain behavior of the transversal acoustic phonons, their branch overlap is reduced and TA modes confined to the AlN layers may occur (see Sect. 5.2.3).
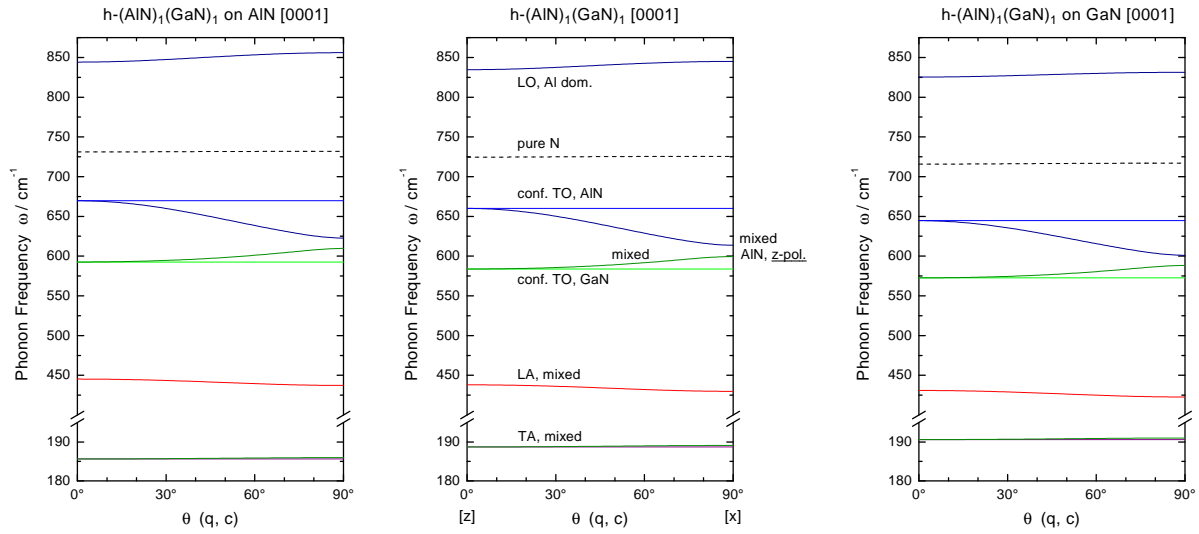
Figure 5.3 Angular dispersion of zone-center phonon modes of an h-(1×1)-[0001] SL for three different strain situations. Left: $a_{SL} = a_{AlN}$; center: a_{SL} of a free-standing SL; right: $a_{SL} = a_{GaN}$. The mode type and the dominant material character is indicated. $\theta(q, c)$ refers to the angle between the c axis of the SL and the phonon propagation direction $\vec{q}$.

For propagation along the stacking direction of the superlattice, transverse modes vibrate in the layer plane and are therefore twofold degenerate. This makes them easily distinguishable from longitudinal modes vibrating perpendicular to the layer plane. For this propagation direction, the longitudinal or transverse character of the modes is the same as for the corresponding bulk modes. This allows to identify the "origin" of the mode. Therefore, to identify a specific mode, the labeling "Lℵ" or "Tℵ" (with "ℵ" standing for either "A" or "O") is kept also for other propagation directions albeit the polarization of the mode might change.

5.2.2 Phonons of 1×1 Superlattices

The 1×1 superlattices play a special role in that of all short-period SLs, in their case the bulk dispersion is folded only once and that they are closest to an ordered alloy. All layers are interface layers and there is no part that could be considered as bulk-like. Therefore, for a hexagonal 1×1 SL in principle the phonon spectrum should be rather similar to that of a 2*H* crystal. Since also for the cubic 1×1 SLs one has a single folding along a high-symmetry direction, their spectrum should be similar to that of the hexagonal 1×1 SLs. For any higher-order SL, however, more foldings are involved and thereby the differences in the bulk dispersions become noticeable. We first discuss the findings for the h-(1×1)-[0001] SLs, the c-(1×1)-[001] SLs will be considered afterwards.

For the hexagonal 1×1 SLs, the phonon spectrum at the Γ point results from a "mixture" of the respective branches of the bulk dispersions, shifted according to the biaxial in-plane strain. Compared to the angular dispersion of the wurtzite nitrides discussed in Sect. 3.2.3, Fig. 5.3 shows some remarkable differences for the short-period wurtzite-based SLs. In addition to the angular dispersion present for the LO and the TO mode, here also the modes resulting from

the acoustic branches show angular dispersion. Moreover, in the range of the TO modes, an additional angular-dependent branch is observed. In the following, we discuss these findings for the modes in order of increasing frequency.

For propagation along the c axis (i.e., for $\theta = 0°$), the back-folded TA modes are twofold degenerate. However, for $\theta > 0°$, a small splitting occurs: With increasing in-plane component of $\vec{q}$, the macroscopic electric field can couple to the x-polarized mode. Due to the lowered symmetry compared to the $2H$ case, the latter's dynamical dipole moment $\mathbf{p}$ does not vanish. The limiting frequency for in-plane propagation (i.e., for $\theta = 90°$) of the dispersive branch depends both on the strength of its dynamical dipole moment and on the screening of the electric field. The same interpretation holds for the LA-derived mode whose angular dispersion is also due to a longitudinal–transverse splitting. However, since for in-plane propagation this mode is polarized along the z direction, the corresponding limiting frequency is a dielectric dispersion frequency, whereas the one for $\theta = 0°$ is determined by the dipole moment and the electric field.

According to the wurtzite bulk dispersions, for the TO phonons one can expect to find both GaN-confined as well as AlN-confined modes. They are indeed present in the h-(1 × 1)-[0001] SLs, the GaN-confined one having the lower and the AlN-confined one having the higher frequency. Similar to the TA-derived modes for $\theta = 0°$ they are twofold degenerate. For the wurtzite bulk phonons, two different TO modes are observed for $\theta = 90°$ due to the anisotropy of the $2H$ structure, which makes a difference with respect to the polarization direction. This frequency difference is a "purely mechanical" one and does not involve the macroscopic electric field. Since the same type of structural anisotropy exists in the SLs, also here a frequency difference between TO modes polarized along the SL stacking direction, z, and in the layer plane can be expected for in-plane propagation. This is indeed the case: For increasing θ, one of the GaN-confined TO modes changes its polarization direction from in-plane to z-oriented. It shows an upward angular dispersion and also changes its character to a mixed mode. In the limit of in-plane propagation, this mode is completely z-polarized and exhibits mainly AlN vibrations. Moreover, it possesses a large $\mathbf{p}$ (as compared to other modes) and is therefore strongly IR-active, its frequency therefore being one of the dielectric dispersion frequencies.

The other angular-dependent branch in the region of the TO modes, showing a downward dispersion into the gap between the AlN- and GaN-confined TO modes for increasing θ, needs special attention since this mode is a common feature of all short-period GaN/AlN-SLs studied here. It is a mixed mode that occurs both in the hexagonal and the cubic SLs. For in-plane propagation, this mode is polarized in the x direction and therefore couples to the electric field, hence its limiting frequency for $\theta = 90°$ is not a dielectric dispersion frequency and the mode is not a "purely mechanical" one. Interestingly, the dynamical dipole moment $\mathbf{p}$ of this mgde varies significantly with the angle: For $\theta = 0°$ it is one of the strongest, whereas for increasing θ it decreases and for $\theta = 90°$ reaches approximately 20 % of the original value. The origin of this mode will be analyzed below. Besides the angular-dependent TO modes discussed so far, there are two other TO modes that are nondispersive. For all angles, they remain confined TO modes. Both are strongly IR-active, their $\mathbf{p}$ being slightly less than that of the upward-dispersive TO branch.

In the region of the LO phonons, two modes are found. The one with the lower frequency exhibits vibrations of the N atoms only. It is mainly z polarized and has a weak $\mathbf{p}$. Corre-

spondingly, its dispersion is practically negligible. On the contrary, the LO branch with the highest frequency has a very strong **p**. Similar to the upward-dispersive TO mode it changes its polarization direction: For $\theta = 0°$ it is z-polarized, whereas for $\theta = 90°$ it is x-polarized. Hence, this mode always couples to the electric field and neither of its limiting frequencies is a dielectric dispersion frequency. This makes it similar to the IR-active LO mode observed for wurtzite bulk crystals. In the following, we further investigate this similarity.

One knows that in binary bulk polar crystals the LO–TO splitting corresponds to a lifting of the degeneracy between longitudinal and transversal modes having the same displacement pattern. The degeneracy is lifted due to the coupling of the LO modes to the electric field.[1] For wurtzite, this allows to establish a correspondence between the limiting values of the angular dispersion of the IR-active LO mode and that of the IR-active TO modes (i.e., the dielectric dispersion frequencies). This correspondence is explicitly expressed by the formula for the LO–TO splitting in the wurtzite case, Eq. (3.3). However, if several IR-active LO modes are present in a crystal, there is no such direct correspondence since several modes contribute to the LO–TO splitting, which then is given by Eq. (2.65), repeated here for convenience:

$$\sum_{j=1}^{r} \left[\omega_j^2(\vec{q}) - \omega_j^2(0) \right] = \frac{e^2}{\varepsilon_0 V} \sum_\kappa \frac{1}{M_\kappa} \frac{|\vec{q} \cdot \mathbf{Z}_{\mathrm{B}}(\kappa)|^2}{\vec{q} \cdot \boldsymbol{\varepsilon}_\infty \cdot \vec{q}} \, . \tag{5.3}$$

From this equation it is not possible to identify the corresponding modes since the pairing under the sum on the left-hand side is arbitrary. Moreover, although in principle the physical argument concerning the degeneracy of the displacement pattern holds, one cannot expect to always find the corresponding LO and TO modes by inspecting their displacements: Due to the non-analytical part of the dynamical matrix, not only the frequency of a longitudinal mode differs from that of the corresponding transversal mode but also its eigenvector might be altered.

In this situation, the numerical calculations can be used to closely inspect the influence of the electric field. By repeating the diagonalization of the full dynamical matrix but employing a different value for the components of the high-frequency dielectric constant, $\boldsymbol{\varepsilon}_\infty$, it is possible to simulate a gradual switch-on (or -off) of the components of the electric field. Thereby one can immediately see which transverse mode couples to the electric field and which LO frequency it gives rise to. If the field would be completely screened (or, equivalently, the coupling to the field would be suppressed by setting the effective charges to zero), only "purely mechanical" modes would be present and they would show no angular dispersion. For the short-period SLs discussed above, this means that both the uppermost LO mode as well as the downward-dispersive TO mode would vanish, and instead of the upward-dispersive TO mode there would be a constant mode at the limiting frequency for in-plane propagation. Both of the in-plane polarized, confined TO modes would be twofold degenerate throughout.[2]

Switching on only the z component of the field affects both the z-polarized TO mode and the "pure N" LO mode. For small angles θ, they exhibit an upward dispersion, and with increasing field strength, the limiting frequency of the former mode approaches the original frequency of the "pure N" LO mode, whereas the latter mode's frequency approaches the one

---

[1] It is exactly this degeneracy with respect to the displacements that also contributes to the static dielectric constant [cf. the generalized LST relation, Eq. (2.67)].

[2] Also the acoustic modes would take on their "purely mechanical" frequency values. Since for them the situation is clear, in the following only the optical modes are considered.

c-(AlN)$_1$(GaN)$_1$ [001]
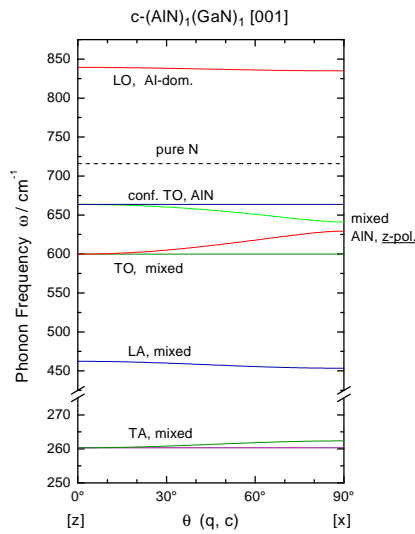
Figure 5.4 Angular dispersion of zone-center phonon modes of a c-(1×1)-[001] SL for an in-plane strain corresponding to a free-standing SL. The mode type and the dominant material character is indicated. $\theta(q, c)$ refers to the angle between the c axis of the SL and the phonon propagation direction $\vec{q}$.

of the uppermost LO mode. Hence, an anticrossing at the frequency of the "pure N" LO mode occurs. If the in-plane components of the electric field are heavily screened (choosing $(\varepsilon_\infty)_{xx} = (\varepsilon_\infty)_{yy} \approx 500,000$ works rather well), the coupling to the other IR-active modes is suppressed. But if the latter screening is reduced, anticrossing with the AlN-confined TO mode occurs, which could lead to a wrong interpretation. Vice versa, switching on only the in-plane components of the field while keeping the z component screened, both twofold-degenerate in-plane-polarized TO modes start to split into different limiting frequencies for $\theta \to 90°$: One branch remains unaffected while the other increases in frequency. The branch split off the AlN-confined TO mode approaches the corresponding limit of the uppermost LO mode, whereas the branch originating from the GaN-confined TO mode approaches the limiting frequency of the downward-dispersive TO mode.

The latter result is remarkable: It demonstrates the different ways the electric field acts among the IR-active modes: First, it is responsible for the limiting frequency values of the dispersive branches that are purely longitudinal, and second, it mixes these pure LO modes to produce the observed angular dispersion. This is clearly what happens for the uppermost LO branch: Its limiting frequencies are related to different TO modes (both of them are dominated by AlN vibrations), and the angular dispersion arises from a mixing of these pure LO modes. It has to be emphasized that the mixing is independent of the creation of the LO modes: Even if one of the limiting frequencies of an angular-dependent branch is a "purely mechanical" one, this does not mean that the other limiting frequency is the corresponding longitudinal one. This holds only for those branches where the longitudinal frequency is higher than the "purely mechanical" one, as is the case for the acoustic modes. On the contrary, the downward-dispersive TO branch does not connect a longitudinal mode to its transversal counterpart, since the latter must have a lower frequency than the longitudinal mode.

Figure 5.3 shows the angular dispersion of the h-(1×1)-[0001] SL for three different in-plane lattice constant, thereby illustrating the influence of a biaxial strain in the basal plane on the superlattice phonons. Corresponding to their bulk behaviour, it can be seen that for increasing a_{SL}, all modes shift to lower frequencies except for the TA-derived ones. The same behaviour with respect to in-plane strain is also found for the c-(1×1)-[001] SLs. The angular

dispersion of the latter is therefore shown in Fig. 5.4 only for one in-plane lattice constant. Also the interpretation of the phonon modes of the cubic-derived SL is completely analogous to that of the hexagonal one. However, three deviations have to be mentioned: First, the lower TO mode is of mixed character and not a GaN-confined one. Second, the LO-derived mode that exhibits only N vibrations has a symmetric pattern with no associated dipole moment, in accordance with the internal structural symmetry (C_2) of the cubic-derived SLs described above. The latter kind of a $\mathbf{p} = \mathbf{0}$ mode is a typcial feature of the cubic-derived SLs. Third, there is a noticeable longitudinal–transverse splitting for the TA-derived mode. This means that the coupling to the electric field is stronger and that this mode also contributes to the static dielectric constant.

5.2.3   Folded Acoustic Phonons

Viewed as a bulk crystal, all $3N - 3$ nonzero Γ-point phonon modes of a short-period super-lattice are optical modes. However, as in the case of the low-frequency B_1 and E_2 mode of $2H$, the lowest $(3N/2) - 3$ nonzero modes can be interpreted as resulting from back-folded acoustic branches of the bulk dispersion. This simple distinction between modes of different origin, just by counting the number of modes (ordered by increasing frequency), is fairly easy for the nitride SLs since there is a large energetical gap between the optical and acoustic modes in bulk GaN which also affects the acoustic modes of the SL.

From its displacement pattern (i. e., the eigenvector) one can identify the dominant material character of a mode (whether it is more related to AlN or GaN vibrations). For the acoustic modes, the general finding is that if new Γ-point modes appear due to back-folding of an interior section of the bulk dispersion (i. e., not from a high-symmetry point), this degenerate frequency splits into a pair of modes, where in many cases the high-frequency one is dominated by Al vibrations and the low-frequency one by Ga vibrations, with a non-negligible contribution also from the other cation type. However, this is not a general rule and a correlation with other quantities (strength of the frequency splitting, number of layers) is hard to establish. For cubic-derived SLs larger than 1×1, modes with $\mathbf{p} = \mathbf{0}$ occur also among the folded acoustic modes.

The strain present in the GaN and AlN layers affects the LA-derived and the TA-derived modes differently: As described for the 1×1 SLs, with increasing tensile strain, the LA-derived modes decrease in frequency, whereas there is an increase for the frequency of the TA-derived modes. For some adjacent LA and TA modes the possibility of a reversed order is implied under different strain situations. This happens, e. g., for the c-(2×2)-SL. Moreover, since the overlap of the TA branches of correspondingly-strained bulk materials decreases under these strain conditions, TA-derived modes confined to the AlN layers occur. As an example, in Fig. 5.5 vibrational pattern of some of the folded acoustic modes of a free-standing h-(3×3)-[0001] SL are shown.

The LA-derived modes exhibit a similar distribution of their displacements. The same holds for the TA- and LA-derived modes of the cubic SLs. In general, the confinement of the upper-most LA-derived mode is not as marked as for the uppermost TA-derived one. Practically, this holds for any in-plane lattice constant, since what matters is the relative position of the branches of the GaN and AlN bulk dispersion. This hardly changes since the biaxial shift coefficients of GaN and AlN phonons are rather similar (cf. Chapter 4).
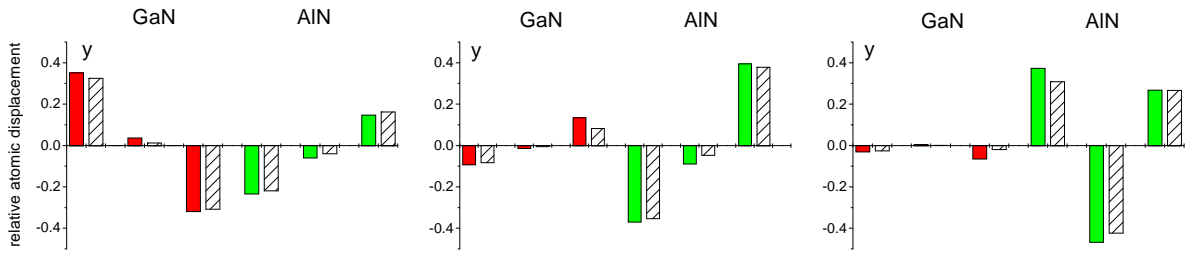
Figure 5.5 Displacement pattern of folded TA modes of an h-(3×3)-[0001] SL (schematic; dark grey columns: Ga displacements, light grey columns: Al displacements; hatched columns: N displacements). The relative atomic displacements in *y* direction are shown for three modes with $\theta = 0°$ (i. e., $\vec{q} \| c$) versus the atomic layer position. Left: Mode with $\omega = 92$ cm^{-1}, folded from $\pi/3\ell$, corresponding to a full period of 6ℓ; propagating. Center: Mode with $\omega = 180$ cm^{-1}, folded from $2\pi/3\ell$, corresponding to a full period of 3ℓ; AlN-dominated. Right: Mode with $\omega = 229$ cm^{-1}, folded from π/ℓ, corresponding to a full period of 2ℓ; confined. Here, ℓ denotes an effective bilayer thickness.

5.2.4 TO Phonons

Due to the clear separation of the bulk TO phonon branches, in GaN/AlN SLs confined TO phonons are to be expected. The angular dispersion of the TO-phonon-related modes found for a cubic-derived 2×4 and a wurtzite-derived 3×3 SL are shown in Fig. 5.6. (Here, a compressive in-plane strain is chosen for the cubic SL for demonstrational purposes, since this strain increases the angular dispersion of the upward-dispersive mode.) For propagation along the SL stacking direction (i. e., $\theta = 0°$) three doubly degenerate GaN-confined and three doubly degenerate AlN-confined modes are found. In general, an $m \times n$ SL has m and n such modes (except for the hexagonal ones with $m + n$ odd, where a doubling of the number of modes occurs). Whereas the AlN-confined modes are found in a narrow frequency range both for the cubic und the hexagonal SL, the GaN-confined modes spread over a larger interval for the cubic SL but are closely spaced in the hexagonal SL. This is due to the differences in the bulk dispersion, cf. Fig. 5.2. As for the folded acoustic modes, the strain dependence of the confined TO modes follows that of the corresponding bulk phonons.

As already noticed for the 1×1 SLs, for increasing θ a downward-dispersive branch is found, reaching from the AlN-confined modes into the gap, towards the GaN-confined modes. For reasons to be explained below, this mode is labeled "interface" in Fig. 5.6. However, concerning the dispersive branch found in the GaN-confined-modes' region, there is a significant difference between the cubic and the hexagonal SLs: The cubic SLs show a strongly upward-dispersive branch, whereas the hexagonal SLs possess a rather flat downward-dispersive one. As known from the 1×1 SLs, the GaN-TO-related dispersive branch is due to a mixing of a strongly IR-active in-plane-polarized TO mode with the strongly IR-active z-polarized mode (whose frequency is a dielectric dispersion frequency) found in the TO region. Correspondingly, the polarization and the character of this mode changes strongly with θ. For the hexagonal SL, this is shown in Fig. 5.7. The pattern of the z displacements is similar to a bulk TO(Γ) mode, since all cations vibrate in phase.
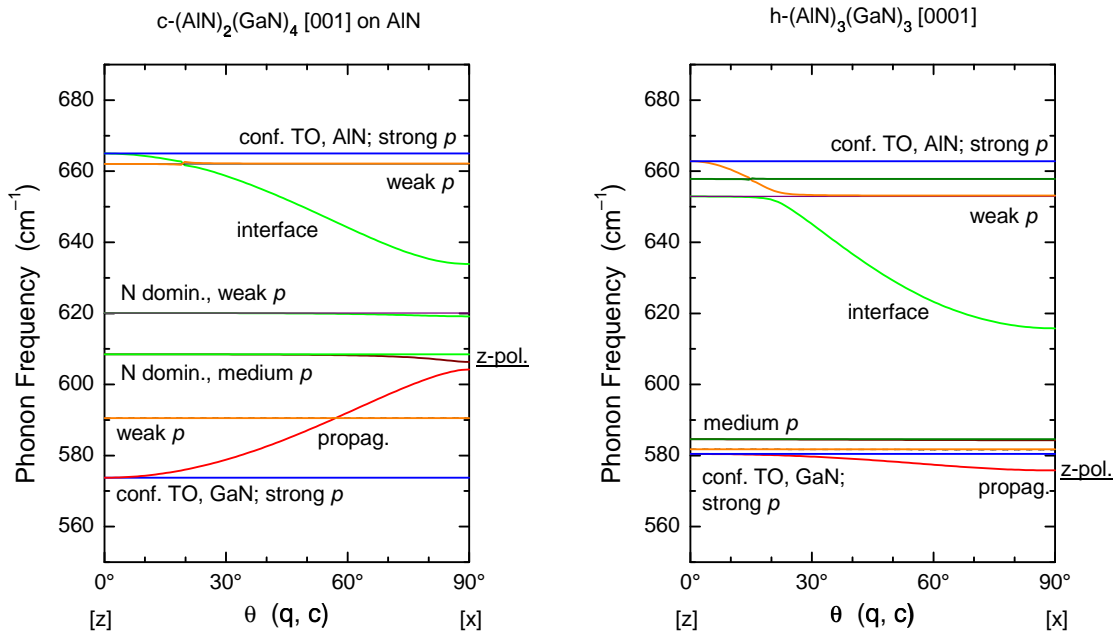
Figure 5.6 Angular dispersion of zone-center TO phonon modes. Left: cubic-derived 2×4 SL, $a_{SL} = a_{AlN}$. Right: wurtzite-derived 3×3 SL, a_{SL} of a free-standing SL. Besides the mode character (confined/propagating) also the relative strength of the dynamical dipole moment **p** is indicated.

In principle, the same holds for the cubic SL. However, since here the z-polarized mode has a slightly lower frequency than the second-highest GaN-confined TO mode and since the latter mode has a non-negligible dipole moment, an additional mode mixing occurs which results in an anticrossing for angles close to $\theta = 90°$. Hence, the upward-dispersive branch ends in a field-related longitudinal mode, similar to the downward-dispersive mode. The strongly IR-active z-polarized mode (marked "z-pol." in Fig. 5.6) is connected with the second-highest GaN-confined TO mode, giving a dispersion that becomes noticeable only for $\theta > 75°$.

As already described for the 1×1 SLs, the $\theta = 90°$ value for the mode found in the TO gap is determined by the field in the layer plane. For $\theta < 90°$ this branch is a mixture of this purely longitudinal mode with the AlN-confined TO mode that possesses the strongest dynamical dipole moment. However, according to the position of the latter mode relative to other AlN-confined modes with non-negligible dipole moments, an additional mixing with those modes may occur, which effectively results in a mode-crossing or anticrossing behaviour, as can be seen for the hexagonal SL in the right part of Fig. 5.6.

The attribution of an interface character to this mode is problematic since this mode is determined for vanishing wavevector **q**, but in order to exhibit the typical decay away from the interface the in-plane component of **q** must be nonzero. Nevertheless, it is justified for the following reasons: (i) Whereas the number of all other types of modes changes with the number of layers (m, n), this mode is always found as a single mode in the gap between the GaN-cofined and the AlN-confined modes. (ii) From a calculation for a GaN(5 nm)/AlN(5 nm) SL using the dielectric continuum model, an interface mode was found in exactly this frequency range [*Gle99*]. (iii) From this mode's displacement pattern, as shown for the h-(3×3)-[0001]
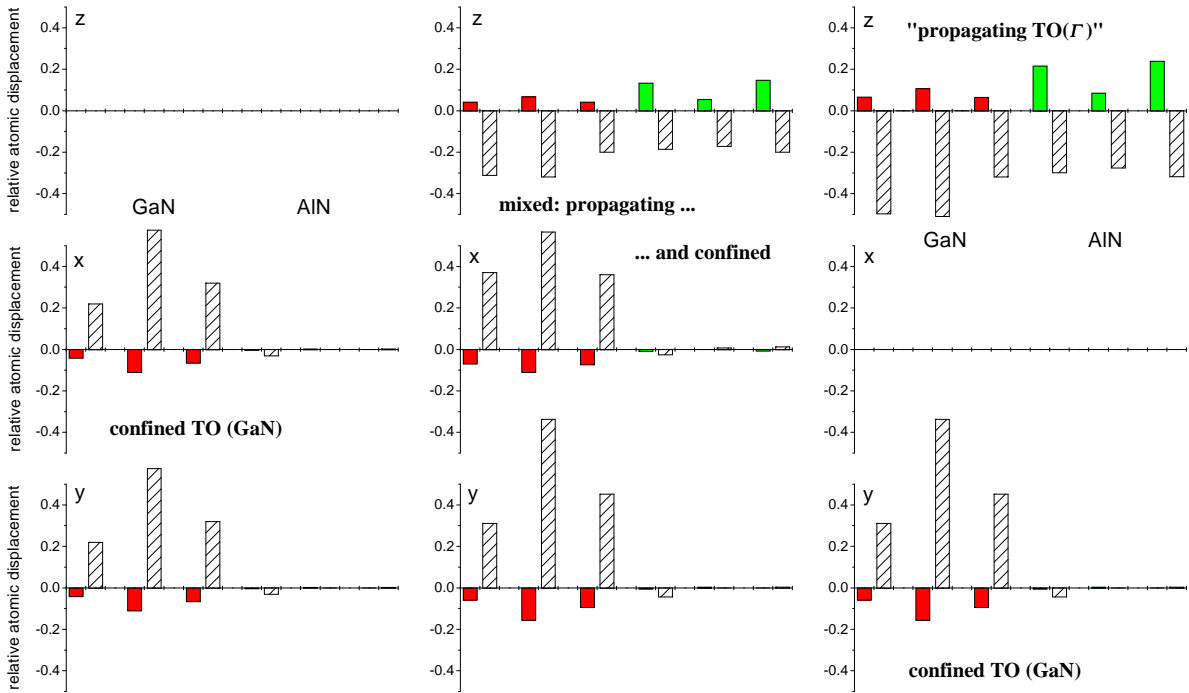
Figure 5.7 Displacement pattern of the lowest-frequency confined TO mode of an h-(3×3)-[0001] SL (schematic; cf. Fig. 5.5). The relative atomic displacements in z direction (top row), in x direction (middle row) and in y direction (bottom row) are shown for the lowest-frequency TO mode at different angles θ versus the atomic layer position. Left column: $\theta = 0°$, doubly-degenerate mode ($\omega = 580$ cm^{-1}). Middle column: $\theta = 45°$, split mode (y-polarized: $\omega = 580$ cm^{-1}, xz-polarized: $\omega = 579$ cm^{-1}). Right column: $\theta = 90°$, split mode (y-polarized: $\omega = 580$ cm^{-1}, xz-polarized: $\omega = 576$ cm^{-1}).

SL in Fig. 5.8, it can be seen that in contrast to the propagating z-polarized TO mode, the GaN and AlN parts of this mode are vibrating out-of-phase relative to each other. This not only justifies to characterize this mode as an interface mode [*Ger91*], it also explains its relatively weak dynamical dipole moment; a fact which was mentioned for the 1×1 SLs but also holds for the higher-order ones.

Finally we mentioned that, although not visible in Fig. 5.6, all doubly degenerate confined TO modes show a very weak splitting according to the strength of their dynamical dipole moment with the corresponding longitudinal frequency slightly above that of the transversal mode. Therefore, the so-called "alternation rule" that each dielectric dispersion frequency is followed by a corresponding LO mode is fulfilled. There has been some controversy about this rule concerning InP/GaP c-(1×1)-[111] SLs [*Als01*, *Ozo01*], which are similar to the GaN/AlN SLs in the sense that they represent the same relative atomic constellation of a III-V material system but shifted by a period in the periodic table of the elements. The angular dispersion calculated for this SLs is in accordance with experimental results [*Ozo01*]. Despite the different stacking direction, it qualitatively agrees completely with the one found here for the nitride 1×1 SLs. This confirms our interpretation that the phonon modes of the latter SLs are those of an ordered alloy.
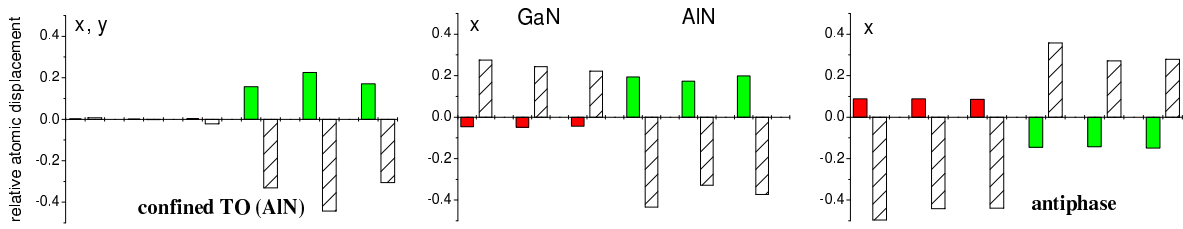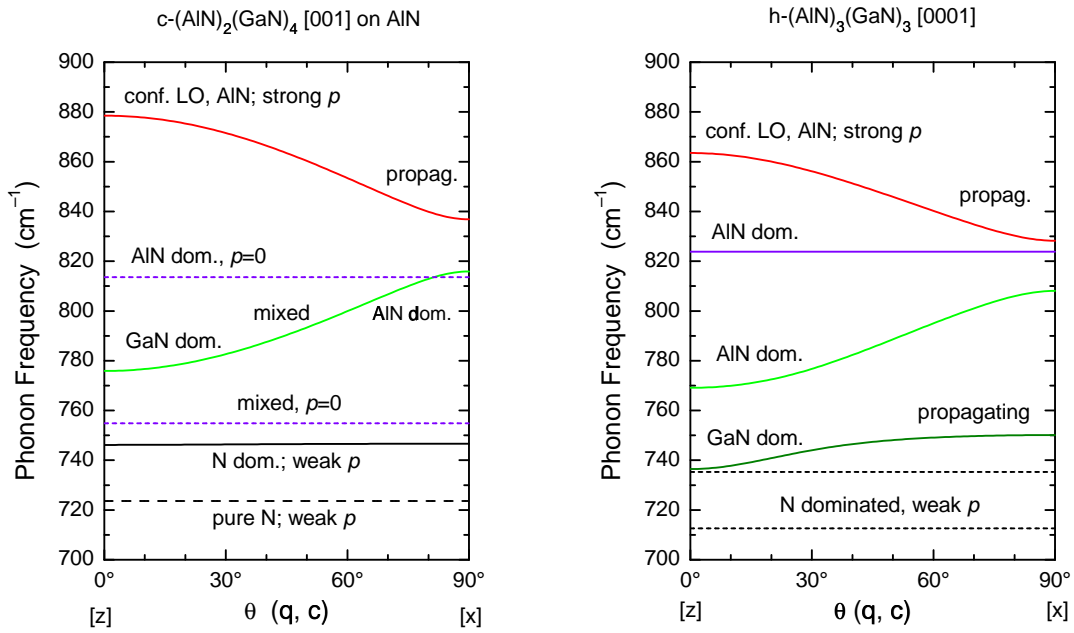
Figure 5.8 Displacement pattern of the TO-gap interface mode of an h-(3×3)-SL (schematic; cf. Fig. 5.5). This modes' relative atomic displacements in x direction are shown for three different propagation directions versus the atomic layer position. Left: $\theta = 0°$, $\omega = 663 \, \text{cm}^{-1}$; center: $\theta = 45°$, $\omega = 633 \, \text{cm}^{-1}$; right: $\theta = 90°$, $\omega = 616 \, \text{cm}^{-1}$. The mode pattern shown for $\theta = 0°$ is that of the highest-frequency AlN-confined TO mode, being the end of the IF-mode branch for small angles despite the mode-mixing-induced anticrossing, cf. Fig. 5.6, since it carries the full angular dependence.

5.2.5   LO Phonons

According to the bulk dispersion, all LO modes above $750 \ldots 800 \, \text{cm}^{-1}$ (depending on the strain state) should be related to AlN or to pure N vibrations. However, for in-plane propagation, the uppermost LO branch shown in Fig. 5.9 for a cubic-derived 2×4 and a wurtzite-derived 3×3 SL exhibits propagating character, with a non-negligible contribution of the Ga atoms. This can be seen from this mode's vibrational pattern, shown in Fig. 5.10 for the hexagonal SL. A similar pattern is found for the cubic SL. This propagating mode is strongly IR-active; it corresponds to the dispersive LO mode discussed already for the 1×1 SLs: Since with increasing θ it changes from z to x polarization, it always couples to the electric field, hence none of its limiting frequencies is a dielectric dispersion frequency.

In order to understand the angular dispersion of the LO modes, as shown in Fig. 5.9, we are interested in discerning the "purely mechanical" modes polarized along the SL c axis. From general symmetry considerations it follows that for a crystal of orthorhombic symmetry or higher and having N_b basis atoms there are $N_b - 1$ such modes polarized along each of the crystallographic axes [as mentioned in the discussion of Eq. (2.67)]. For the SLs investigated here, $N_b/2$ of these modes stem from the optical branches of the bulk constitutents. One of them is always found in the region of the TO modes. Therefore, $N_b/2 - 1$ "purely mechanical" modes remain to be indentified in the LO modes' region. Since there are always $N_b/2$ modes present in this region and the uppermost one is not related to a "purely mechanical" vibration, all other branches must be related to such vibrations. It turns out that the frequencies in the limit of in-plane propagation are those of the "purely mechanical" vibrations, since then they do not couple to the electric field.

Therefore, if the macroscopic electric field would be completely screened (or if the coupling to the field would be suppressed), all LO modes would remain constant at the frequency found for $\theta = 90°$ except for the uppermost one, which would vanish from the LO modes' region but show up again as an additional TO mode. When switching on the z component of the field, all z-polarized modes with a nonvanishing **p** experience an upward dispersion for small θ. With

Figure 5.9 Angular dispersion of zone-center LO phonon modes. Left: cubic-derived 2×4 SL, $a_{SL} = a_{AlN}$. Right: wurtzite-derived 3×3 SL, a_{SL} of a free-standing SL. Besides the mode character (confined/propagating) also the relative strength of the dynamical dipole moment **p** is indicated. Notice the mode crossing with the $\mathbf{p} = \mathbf{0}$ mode for the cubic SL.
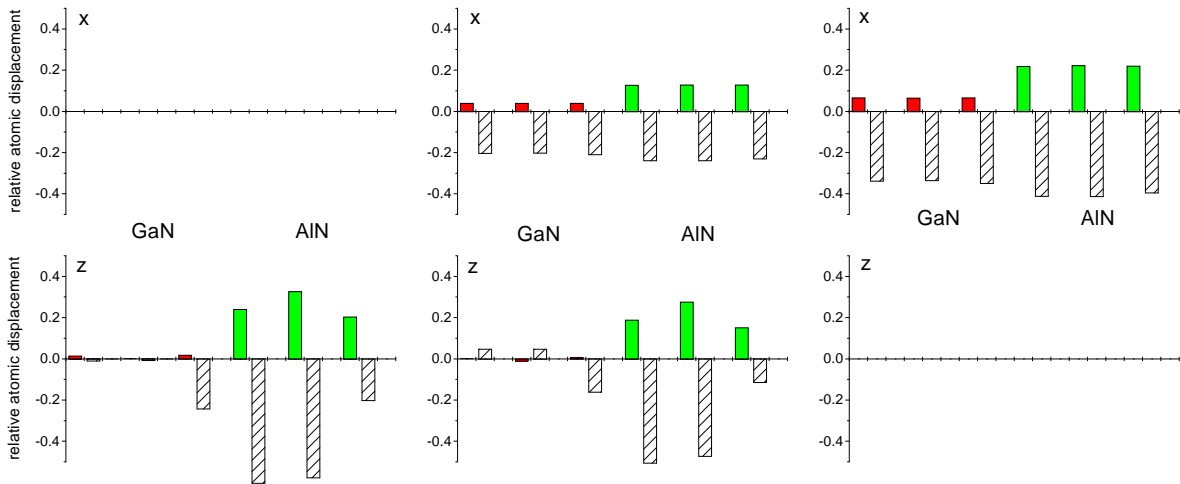
Figure 5.10 Displacement pattern of the uppermost LO mode of an h-(3×3)-SL (schematic; cf. Fig. 5.5). The relative atomic displacements in x direction (upper row) and in z direction (lower row) are shown for three different propagation directions versus the atomic layer position. Left: $\theta = 0°$, $\omega = 863$ cm^{-1}, AlN-confined. Center: $\theta = 45°$, $\omega = 849$ cm^{-1}, mixed propagating (x displacements) and quasi-confined (z displacements). Right: $\theta = 90°$, $\omega = 828$ cm^{-1}, propagating.

increasing field strength, each of these modes approaches the $\theta = 0°$ limiting frequency of the next-higher mode.

In other words: The limiting frequency for $\theta = 0°$ of the LO branches is, in the sense of an LO–TO splitting, related to the next "purely mechanical" LO vibration with a nonvanishing dipole moment found *below* the present one, not above — although the upward dispersion found for the SLs might lead to this wrong impression. The upward dispersion is merely due to the mixing of the different limiting frequencies. In particular, it does not imply that a decrease in frequency occurs due to the admixture of the macroscopic electric field. At least for crystals of orthorhombic symmetry of higher, the nonanalytic part of the dynamical matrix always leads to an increase of the vibrational frequency if a mode polarized along one of the crystallographic axes couples to the electric field.

Chapter 6

Summary and Outlook

In this dissertation, ab-initio investigations of the strain influence on vibrational properties of GaN and AlN as well as of short-period GaN/AlN superlattices are presented. Based on density-functional theory and density-functional perturbation theory, for differently strained structures complete phonon spectra and related properties are calculated unsing the local-density approximation and norm-conserving pseudopotentials. The results either agree with available experimental data, or the occurring discrepancies can be widely clarified, leading to a consistent picture. Where experimental results are not available, the results therefore present a reliable prediction of the missing data. In addition, the present results provide physical interpretations for the lattice-dynamical properties of GaN and AlN.

The ab-initio DFT-LDA calculations render the total energy of a given crystal structure in dependence on the atomic coordinates. For the minimization of the total energy, which yields the equilibrium structure, in this work a systematic variation of the atomic positions and a subsequent polynomial fit are performed. For a high enough cutoff energy of the plane-wave expansion this method leads to fairly precise lattice constants. Changes in the third position after the decimal point can be resolved. This accuracy is necessary since the final results must be given as a change of the investigated quantity (lattice parameters, phonon frequencies, dielectric constant etc.) relative to the change of the lattice constants. Thereby one faces the problem of dividing by a small quantity, thus an accuracy of the final result of the order of 1 % requires an accuracy for the determination of the lattice constants below 0.1 %. In this work, the latter accuracy is reached.

The bulk materials are considered being subject to three different deformations, corresponding to hydrostatic pressure, a biaxial stress in the basal plane, and a uniaxial pressure perpendicular to the basal plane. The latter case, although not realized experimentally, is included since it provides additional material parameters. Since it is complementary to hydrostatic pressure and biaxial stress, a comparison of the three independent calculations provides a consistency check of the results obtained. However, this requires the relaxed structures to be identical for each type of deformation. Since the relaxed structures serve as reference for the strain-related changes, a comparison of differently obtained results is possible only if they refer to the same reference. In this work, the conformity of the relaxed structures is obtained by choosing a rather large numerical cutoff energy. For the relaxed ground state of 3*C* and 2*H* polytypes of GaN and AlN, the lattice parameters, the bulk modulus and its pressure derivative are determined. The

coresponding equation of state, i. e., the pressure–volume relation, is in very good agreement with experimental data.

Further, we determine the variation of the lattice geometry (bond length and bond angles, lattice constant ratio c/a, internal paramter u) under the influence of hydrostatic pressure as well as of biaxial and uniaxial stress. The cubic polytypes of GaN and AlN behave practically the same, whereas for the wurtzite polytypes a significant difference is found: Under hydrostatic pressure, GaN undergoes a proportional contraction, whereas AlN shows an anisotropic behaviour. This is confirmed by experimental data. It is not easy to determine the internal parameter u experimentally, and it is not accessible using macroscopic elastic constants. On the other hand, it is an important material parameter since the polarization of the $2H$ polytypes changes considerably with u. Therefore, the structural results presented here provide an iomportant contribution to the description of the material properties of GaN and AlN.

From the relaxation calculations performed at different steps for the given deformation type it follows that over a range of approximately $\pm 2\,\%$ strain both polytypes of GaN and AlN behave almost elastically linear. From the proportionality factors and the bulk modulus we determine the elastic constants. Comparing these consistently determined data with literature values becomes clear which of the latter are reliable and which are not.

For the calculated strained structures the dynamical matrix, the tensor components of the dielectric constant and of the Born effective charges are calculated using DFPT. For these calculations it suffices to consider the primitive cell only; due to the perturbational approach, no supercell calculations are necessary to obtain results for the LO modes. The mode eigenvector determines the symmetry of the mode and the calculated frequencies can be classified accordingly. Using the generalized Lyddane–Sachs–Teller relation, the static dielectric constant can be calculated from the high-frequency one and the LO- and TO-mode frequencies. A calculation of the phonon frequencies in dependence on the internal parameter u (possible only in the theory) shows how sensitive the lattice vibrations react to changes in the atomic arrangements. Varying u by 1 % leads to a change in the phonon freqeuncies of approximately 5 %. This emphasizes how necessary it is to calculate the lattice parameters as precisely as possible.

In conjunction with the structural properties determined this renders the pressure and strain dependence of the dielectric properties and the phonon frquencies, which yield the mode Grüneisen parameter, the biaxial and uniaxial mode coefficients as well as the phonon deformation potentials. In this work, phonon deformation potentials of $2H$-AlN were presented for the first time; experimental values were not present at that time. The dielectric properties show marked nonlinearities in dependence on strain. The low-frequency E_2 mode of the $2H$ polytypes exhibits a particular pressure and strain dependence: Instead of shifting to higher energies under compressive deformations (as is observed for all other modes), its frequency decreases. This mode softening is, however, rather weak and it is not related to the pressure-induced phase transition of the nitrides. For the corresponding zone-boundary TA mode of the cubic we also find a softening. This behaviour is known from other materials. For silicon it was explained as being due to an interplay of central and angular forces. However, due to the high ionicity of the nitrides and the different masses of anion and cation this model cannot be transferred to the group-III nitrides. Employing the frozen-phonon method we show that the decrease in frequency of the E_2^{low} mode mainly results from a change in the interplay of Ewald and Hartree energy. Differences between GaN and AlN were observed as well as between the E_2^{low} and the

E_2^{high} mode: The increase of the latter mode's frequency is due to an interchanged role of the influence of Ewald and Hartree energy compared to the E_2^{low} mode.

Our results decisively contribute to the clarification of the pressure-induced increase of the LO–TO splitting, which is consistently observed in experiments. This increase is not due to an increase in ionicity (as for SiC) but to the decrease of the dielectric screening: Both the Born effective charge and the high-frequency dielectric constant decrease with increasing pressure. Yet the decrease of the dielectric constant is more pronounced, thus the screened effective charge, which is the relevant lattice-dynamical quantity determining the strength of the LO–TO splitting, is increasing with pressure.

All findings for strain dependences of lattice dynamical properties are compared with experimental results. For hydrostatic pressure, a systematic underestimation of the mode Grüneisen parameter is found, amounting to approximately 20 %. The reason for this discrepancy is not clear: Since it occurs both for GaN and AlN, it cannot be related to the nonlinear core correction that is employed for the Ga atom only. We suppose that it is related to an unsufficient description of the electronic states (especially the band gap) and their pressure and strain dependence. This problem appeared rather unexpectedly, since using the same method a rather good agreement of experimental and theoretical results for SiC and for other III–V semiconductors (mainly arsenides) was achieved. This systematic discrepancy only insignificantly belittles the value of the results obtained in this work, since still the relationships are given correctly. This refers both to the different mode coefficients of a single material as well as to a comparison of different materials and/or polytypes.

Comparing the calculated coefficients for biaxial stress with experimental data revealed much larger discrepancies than what should have been expected from the above-mentioned findings. A detailed investigation leads to the conclusion that most of the discrepancies are related to mistakes made in the conversion of the "raw" experimental data to the final result or to the usage of unreliable conversion factors. After correcting these conversions a reasonable agreement with the calculated results is found. Moreover, also discrepancies among the experimental data are reduced. As a conseqeunce of this revision the biaxial stress as inferred from Raman measurements must be larger than determined so far.

From the investigation of the short-period nitride superlattices (being treated as a model system for nitride heterostructures) several peculiarities are noticed. The internal relaxation of the superlattice leads to a geometry deviating from the one determined using elstic constants. This becomes noticeable especially for the hexagonal superlattices, where the heights of the GaN and AlN layers are modified in the opposite way as compared to the macroscopic theory (including the polarization and field effects). For the phonons, a distribution of the modes completely different from GaAs/AlAs superlattices is found. The energetical ordering of the modes and the partial overlap of the bulk phonon dispersions, which have to be considered with in the appropriate strain applied, leads to separate frequency regions for all of the LO and all of the TO modes as well as the acoustic modes.

The pseudomorphically strained GaN and AlN layers exhibit an increased frequency difference between the GaN and AlN TA modes. Hence AlN-confined folded TA modes appear. The highest-frequency LA modes are not completely confined to the AlN layers. Except for one of them, all TO modes are also confined modes; they are polarized in the layer plane. The deviating TO mode showing propagating behaviour is found in the frequency region of the GaN-confined

modes, its frequency being one of the dielectric dispersion frequencies and its polarization being directed along the stacking direction. In the band gap between the AlN-confined and the GaN-confined modes an interface mode is found for all superlattices, independent of the number of layers and the polytype. It is a planar mode exhibiting a strong angular dependence. Except for the ones dominated by nitrogen vibrations also the LO modes show angular dispersion, all being polarized mainly in the stacking direction. The only exception is the uppermost LO mode. It changes its polarization direction and it is strongly IR active, thus for all propagation directions it couples to the electric field, in complete analogy to the polar LO mode of bulk material. The strain dependence of all superlattice modes is determined by that of the bulk materials. All in all, the short-period superlattices exhibit phonon properties typical both for thicker superlattices (confined and interface modes) as well as for a bulk material.

From the results presented here further possible or useful investigations can be pointed out. Most urgent are analoguous calculations for InN, which were not tractable for some time because of technical problems. On the one hand, the band gap of InN as determined in the DFT-LDA calculation practically vanishes or even becomes negative, which leads to difficulties in the calculation of the phonons. On the other hand, it became obvious that the nonlinear core correction does not suffice to correctly describe the influence of the core elctrons. Although the lattice constant and the dielectric constant are obtained in reasonable agreement with experimental data (which are also critical for InN), the calculation of the phonon frequencies fails [*Ple98*]. Only when using a pseudopotential that takes the $4d$ electrons fully into account as valence electrons, valid results are obtained from a DFPT calculation [*Bun00*].

The methods used here can be applied to details of the structural and phonon properties as well as of their strain dependence (analogously to the comparison of the E_2^{low} and E_2^{high} mode). At many occasions one may notice hints that the high ionicity of the nitrides plays an important role already for their structural properties. Therefore it is reasonable to monitor the change in the static ionicity in dependence on strain also for the $2H$ polytypes. Due to the lowered symmetry, the method of Garcia and Cohen cannot be used. Instead, calculations based on the Berry-Phase approach would help here.

The most important extension would be, of course, to calculate ab-ititio the phonons of a mixed group-III nitride alloy. From model calculation the one- or two-mode behaviour to be expected is already known, therefore the simple virtual-crystal approximation cannot be used. In principle, a possibility would be to employ a cluster expansion method; another possibility would be the to employ a supercell and fill the atomic in a random way. However, the realization of the supercell calculation using normconserving pseudopotentials is an illusion due to the high cutoff energy required. A possible chance, then, is the use of non-normconserving pseudopotentials of the Vanderbilt type.

Bibliography

[*Ana91*]   E. Anastassakis, Solid State Commun. **78**, 347 (1991).

[*Age98*]   J. W. Ager III, G. Conti, L. T. Romano, and C. Kisielowski, Mater. Res. Soc. Sympos. Proc. **482**, 769 (1998).

[*Aka67*]   I. Akasaki and M. Hashimoto, Solid State Commun. **5**, 851 (1967).

[*Alc01*]   A. B. Alchagirov, J. P. Perdew, J. C. Boettger, R. C. Albers, and C. Fiolhais, Phys. Rev. B **63**, 22 41 15 (2001).

[*Als01*]   F. Alsina, J. Pascual, and N. Mestres, Phys. Rev. B **63**, 08 72 01 (2001).

[*Ama88*]   H. Amano, K. Hiramatsu, and I. Akasaki, Jpn. J. Appl. Phys. **27**, L1384 (1988).

[*Ama89*]   H. Amano, M. Kito, K. Hiramatsu, and I. Akasaki, Jpn. J. Appl. Phys. **28**, L2112 (1989).

[*Amb98*]   O. Ambacher, J. Phys. D: Appl. Phys. **31**, 2653 (1998).

[*Azu95*]   T. Azuhata, T. Sota, K. Suzuki, and S. Nakamura, J. Phys.: Condens. Matter **7**, L129 (1995).

[*Bac82*]   G. B. Bachelet, D. R. Hamann, and M. Schlüter, Phys. Rev. B **26**, 4199 (1982).

[*Bar73*]   A. S. Barker and M. Ilegems, Phys. Rev. B **7**, 743 (1973).

[*Bar80*]   U. von Barth and C. D. Gelatt, Phys. Rev. B **21**, 2222 (1980).

[*Bar01*]   S. Baroni, S. De Gironcoli, A. Dal Corso, and P. Giannozzi, Rev. Mod. Phys. **73**, 515 (2001).

[*Bec00*]   F. Bechstedt, Ulrike Grossner, and J. Furthmüller, Phys. Rev. B **62**, 8003 (2000).

[*Bec02a*]   F. Bechstedt and J. Furthmüller, J. Cryst. Growth **246**, 315 (2002).

[*Bec02b*]   F. Bechstedt, *Nitrides as seen by a theorist,* in: *Low-Dimensional Nitride Semiconductors,* ed. by B. Gil (Oxford University Press; Oxford, 2002), p. 11.

[*Beh99*]   M. K. Behbehani, E. L. Piner, S. X. Liu, N. A. El-Masry, and S. M. Bedair, Appl. Phys. Lett. **75**, 2202 (1999).

[*Böt83*]   H. Böttger, *Principles of the Theory of Lattice Dynamics* (Akademie-Verlag; Berlin, 1983).

[*Bon96*]   C. Boney, Z. Yu, W. H. Rowland, Jr., W. C. Hughes, J. W. Cook, Jr., J. F. Schetzina, G. Cantwell, and W. C. Harsch, J. Vac. Sci. Technol. B **14**, 2259 (1996).

[*Bor12*]   M. Born and Th. von Kármán, Z. Physik **13**, 357 (1912).

[*Bor27*]   M. Born and R. Oppenheimer, Ann. d. Physik **84**, 457 (1927).

[*Bor54*]   M. Born and K. Huang, *Dynamical Theory of Crystal Lattices* (Oxford University Press; Oxford, 1954).

[*Bun00*]   C. Bungaro, K. Rapcewicz, and J. Bernholc, Phys. Rev. B **61**, 6720 (2000).

[*Byk97*]   A. D. Bykhovski, B. L. Gelmont, and M. S. Shur, J. Appl. Phys. **81**, 6332 (1997).

[*Byl86*]   D. M. Bylander and L. Kleinman, Phys. Rev. B **34**, 5280 (1986).

[*Cep80*]   D. M. Ceperley and B. J. Alder, Phys. Rev. Lett. **45**, 566 (1980).

[*Cha73*]   D. J. Chadi and M. L. Cohen, Phys. Rev. B **8**, 5747 (1973).

[*Cho96*]   W. W. Chow, A. F. Wright, and J. S. Nelson, Appl. Phys. Lett. **68**, 296 (1996).

[*Chr93*]   N. E. Christensen and I. Gorczyca, Phys. Rev. B **47**, 4307 (1993).

[*Chr94*]   N. E. Christensen and I. Gorczyca, Phys. Rev. B **50**, 4397 (1994).

[*Coc62*]   W. Cochran and R. H. Cowley, J. Phys. Chem. Solids **23**, 447 (1962).

[*Coh89*]   M. L. Cohen and J. R. Chelikowsky, *Electronic Structure and Optical Properties of Semiconductors,* Springer Series in Solid-State Sciences **75** (Springer; Berlin, 1989).

[*CSN04*]   Compound Semiconductor News, March 2004
(`http://compoundsemiconductor.net/articles/news/8/3/12/1`).

[*Dal93*]   A. Dal Corso, S. Baroni, R. Resta, and S. de Gironcoli, Phys. Rev. B **47**, 3588 (1993).

[*Dav97*]   V. Yu. Davydov, N. S. Averkiev, I. N. Goncharuk, D. K. Nelson, I. P. Nikitina, A. S. Polkovnikov, A. N. Smirnov, M. A. Jacobson, and O. K. Semchinova, J. Appl. Phys. **82**, 5097 (1997).

[*Dav98*]   V. Yu. Davydov, Yu. E. Kitaev, I. N. Goncharuk, A. N. Smirnov, J. Graul, O. Semchinova, D. Uffmann, M. B. Smirnov, A. P. Mirgorodsky, and R. A. Evarestov, Phys. Rev. B **58**, 12 899 (1998).

[*Dav02*]   V. Yu. Davydov, A. A. Klochikhin, V. V. Emtsev, S. V. Ivanov, V. V. Vekshin, F. Bechstedt, J. Furthmüller, H. Harima, A. V. Mudryi, A. Hashimoto, A. Yamamoto, J. Aderhold, J. Graul, and E. E. Haller, Phys. Status Solidi B **230**, R4 (2002).

[*Deg98*]   C. Deger, E. Born, H. Angerer, O. Ambacher, M. Stutzmann, J. Hornsteiner, E. Riha, and G. Fischerauer, Appl. Phys. Lett. **72**, 2400 (1998).

[*Dem96*]   F. Demangeot, J. Frandon, M. A. Renucci, O. Briot, B. Gil, and R. L. Aulombard, Solid State Commun. **100**, 207 (1996); MRS Internet J. Nitride Semicond. Res. **1**, 23 (1996).

[*Det92*]   T. Detchprohm, K. Hiramatsu, K. Itoh, and I. Aksaki, Jpn. J. Appl. Phys. **31**, L1454 (1992).

[*Dre90*]   R. M. Dreizler and E. K. U. Gross, *Density Functional Theory* (Springer; Berlin, 1990).

[*Ejd71*]   E. Ejder, Phys. Status Solidi A **6**, 445 (1971).

[*Esch96*]   H. Eschrig, *The Fundamentals of Density Functional Theory* (Teubner; Leipzig, 1996).

[*Eva83*]   R. A. Evarestov and V. P. Smirnov, Phys. Status Solidi B **119**, 9 (1983).

[*Fer27*]   E. Fermi, Rend. Accad. Naz. Lincei **6**, 602 (1927).

[*Fer28*]   E. Fermi, Z. Phys. **48**, 73 (1928).

[*Fer34*]   E. Fermi, Nuovo Cimento **11**, 157 (1934).

[*Fil95*]   A. Filippetti, D. Vanderbilt, W. Zhang, Y. Cai, and G. B. Bachelet, Phys. Rev. B **52**, 11 793 (1995).

[*Fil96*]   L. Filippidis, H. Siegle, A. Hoffmann, C. Thomsen, K. Karch, and F. Bechstedt, Phys. Status Solidi B **198**, 621 (1996).

[*Gar93a*]   A. Garcia and M. L. Cohen, Phys. Rev. B **47**, 4215 (1993).

[*Gar93b*]   A. Garcia and M. L. Cohen, Phys. Rev. B **47**, 6751 (1993).

[*Ger91*]   H. Gerecke and F. Bechstedt, Phys. Rev. B **43**, 7053 (1991).

[*Gia91*]   P. Giannozzi, S. De Gironcoli, P. Pavone, and S. Baroni, Phys. Rev. B **43**, 7231 (1991).

[*Gie89*]   M. Giehler, M. Ramsteiner, P. Waltereit, K. H. Ploog, and H. Obloh, J. Appl. Phys. **89**, 3634 (2001).

[*Gle99*]   J. Gleize, M. A. Renucci, J. Frandon, and F. Demangeot, Phys. Rev. B **60**, 15 985 (1999).

[*Gle01*]   J. Gleize, J. Frandon, M. A. Renucci, and F. Bechstedt, Phys. Rev. B **63**, 07 33 08 (2001).

[*Gle03*]   J. Gleize, M. A. Renucci, J. Frandon, E. Bellet-Amalric, and B. Daudin, J. Appl. Phys. **93**, 2065 (2003).

[*God89*]   R. W. Godby and R. J. Needs, Phys. Rev. Lett **62**, 1169 (1989).

[*Gör94*]   A. Görling and M. Levy, Phys. Rev. A **50**, 196 (1994).

[*Gör95*]   A. Görling and M. Levy, Int. J. Quant. Chem. Symp. **29**, 93 (1995).

[*Gom86*]   P. Gomes Dacosta, O. H. Nielsen, and K. Kunc, J. Phys. C **19**, 3163 (1986).

[*Goñ01*]   A. R. Goñi, H. Siegle, K. Syassen, C. Thomsen, and J.-M. Wagner, Phys. Rev. B **64**, 03 52 05 (2001).

[*Gor95*]   I. Gorczyca, N. E. Christensen, E. L. Peltzer y Blanca, and C. O. Rodiguez, Phys. Rev. B **51**, 11 936 (1995).

[*Gri00*]   H. Grille, Ch. Schnittler, and F. Bechstedt, Phys. Rev. B **61**, 6091 (2000).

[*Gun85*]   O. Gunnarsson and R. O. Jones, Phys. Rev. B **31**, 7588 (1985).

[*Haa91*]   M. A. Haase, J. Qiu, J. M. DePuydt, and H. Cheng, Appl. Phys. Lett. **59**, 1272 (1991).

[*Ham79*]   D. R. Hamann, M. Schlüter, and C. Chiang, Phys. Rev. Lett. **43**, 1494 (1979).

[*Har89*]   W. A. Harrison, *Electronic Structure and the Properties of Solids* (Dover; New York, 1989).

[*Har99*]   H. Harima, T. Inoue, S. Nakashima, H. Okumura, Y. Ishida, S. Yoshida, T. Koizumi, H. Grille, and F. Bechstedt, Appl. Phys. Lett. **74**, 191 (1999).

[*Hau64*]   A. Haug, *Theoretische Festkörperphysik, Band 1* (Deuticke; Wien, 1964).

[*Hau00*]   P. Haupt, *Continuum Mechanics and Theory of Materials* (Springer; Berlin und Heidelberg, 2000).

[*Her40*]   C. Herring, Phys. Rev. **57**, 1169 (1940).

[*Hof96*]   A. Hoffmann, in: Festkörperprobleme / Advances in Solid State Phsics, Vol. 36, ed. by R. Helbig (Vieweg; Braunschweig und Wiesbaden, 1996), p. 33.

[*Hoh64*]   P. Hohenberg and W. Kohn, Phys. Rev. **136**, B864 (1964).

[*Jai00*]   S. C. Jain, M. Willander, J. Narayan, and R. Van Overstraeten, J. Appl. Phys. **87**, 965 (2000).

[*Jov03*]   V. D. Jovanović, Z. Ikonić, D. Indjin, P. Harrison, V. Milanović, and R. A. Soref, J. Appl. Phys. **93**, 3194 (2003).

[*Kar93*]   K. Karch, Ph. D. dissertation (*Ab-initio-Berechnung der statischen und dynamischen Eigenschaften des Diamanten, Siliziums und Siliziumcarbids,* Regensburg, 1993).

[*Kar96*] K. Karch and F. Bechstedt, Europhys. Lett. **35**, 195 (1996); K. Karch, F. Bechstedt, P. Pavone, and D. Strauch, Phys. Rev. B **53**, 13 400 (1996).

[*Kar97a*] K. Karch, F. Bechstedt, and T. Pletl, Phys. Rev. B **56**, 3560 (1997).

[*Kar97b*] K. Karch and F. Bechstedt, Phys. Rev. B **56**, 7404 (1997).

[*Kar98*] K. Karch, J.-M. Wagner, H. Siegle, C. Thomsen, and F. Bechstedt, Proc. 7th Int. Conf. SiC, III-Nitrides & Related Materials, ed. by G. Pensl, H. Morkoç, B. Monemar, and E. Janzén (Trans Tech Publ. Ltd.; Zürich, 1998), p. 303.

[*Kea66*] P. N. Keating, Phys. Rev. **145**, 627 (1966).

[*Kim94*] K. Kim, W. R. L. Lambrecht, and B. Segall, Phys. Rev. B **50**, 1502 (1994).

[*Kim96*] K. Kim, W. R. L. Lambrecht, and B. Segall, Phys. Rev. B **53**, 16 310 (1996).

[*Kis96*] C. Kisielowski, J. Krüger, S. Ruvimov, T. Suski, J. W. Ager, III, E. Jones, Z. Liliental-Weber, M. Rubin, E. R. Weber, M. D. Bremser, and R. F. Davis, Phys. Rev. B **54**, 17 745 (1996).

[*Kis02*] K. Kishino, A. Kikuchi, H. Kanazawa, and T. Tachibana, Appl. Phys. Lett. **81**, 1234 (2002).

[*Kit98*] Yu. E. Kitaev, M. F. Limonov, P. Tronc, and G. N. Yushin, Phys. Rev. B **57**, 14 209 (1998).

[*Kle80*] L. Kleinman, Phys. Rev. B **21**, 2630 (1980).

[*Klo98*] M. Klose, N. Wieser, G. C. Rohr, R. Dassow, F. Scholz, and J. Off, J. Cryst. Growth **189/190**, 634 (1998).

[*Koh65*] W. Kohn and L. J. Sham, Phys. Rev. **140**, A1133 (1965).

[*Kor97*] D. Korakakis, K. F. Ludwig, Jr., and T. D. Moustakas, Appl. Phys. Lett. **71**, 72 (1997).

[*Koz99*] P. Kozodoy, M. Hansen, S. P. DenBaars, and U. K. Mishra, Appl. Phys. Lett. **74**, 3681 (1999).

[*Kun81*] K. Kunc and R. M. Martin, Phys. Rev. B **24**, 2311 (1981).

[*Lag79*] O. Lagerstedt and B. Monemar, Phys. Rev. B **19**, 3064 (1979).

[*Law72*] P. Lawaetz, Phys. Rev. B **5**, 4039 (1972).

[*Led43*] W. Ledermann, Nature **151**, 197 (1943); Proc. Roy. Soc. **182**, 362 (1944).

[*Lei91*] T. Lei, M. Fanciulli, R. J. Molnar, T. D. Moustakas, R. J. Graham, and J. Scanlon, Appl. Phys. Lett. **59**, 944 (1991).

[*Les96*] M. Leszczynski, H. Teisseyre, T. Suski, I. Grzegory, M. Bockowski, J. Jun, S. Porowski, K. Pakuła, J. M. Baranowski, C. T. Foxon, and T. S. Cheng, Appl. Phys. Lett. **69**, 73 (1996).

[*Li03*] J. Li, K. B. Nam, M. L. Nakarmi, J. Y. Lin, H. X. Jiang, P. Carrier, and S.-H. Wei, Appl. Phys. Lett. **83**, 5163 (2003).

[*Lie83*] E. H. Lieb, Int. J. Quant. Chem. **24**, 243 (1983).

[*Liu93*] H. Liu, A. C. Frenkel, J. G. Kim, and R. M. Park, J. Appl. Phys. **74**, 6124 (1993).

[*Liu98*] Z. X. Liu, K. P. Korona, K. Syassen, J. Kuhl, K. Pakuła, J. M. Baranowski, I. Grzegory, and S. Porowski, Solid State Commun. **108**, 433 (1998).

[*Lou63*] R. Loudon, Adv. Phys. **13**, 423 (1963).

[*Lou82*] S. G. Louie, S. Frøyen, and M. L. Cohen, Phys. Rev. B **26**, 1738 (1982).

[*Luc71*]   G. Lucovsky, R. M. Martin, and E. Burstein, Phys. Rev. B **4**, 1367 (1971).

[*Maj96*]   J. A. Majewski, M. Städele, and P. Vogl, MRS Internet J. Nitride Semicond. Res. **1**, 30 (1996).

[*Mal97*]   F. Malengreau, M. Vermeersch, S. Hagège, R. Sporken, M. D. Lange, and R. Caudano, J. Mater. Res. **12**, 175 (1997).

[*Mar63*]   A. A. Maradudin, E. W. Montroll, and G. H. Weiss, *Theory of Lattice Dynamics in the Harmonic Approximation,* Solid State Physics Supplement 3, ed. by F. Seitz and D. Turnbull (Academic Press; New York and London, 1963).

[*Mar72*]   R. M. Martin, Phys. Rev. B **6**, 4546 (1972).

[*Mar86*]   J. L. Martins and A. Zunger, Phys. Rev. Lett. **56**, 1400 (1986).

[*Mat77*]   J. W. Matthew and A. E. Blakeslee, J. Vac. Sci. Technol. **14**, 989 (1977).

[*McN93*]   L. E. McNeil, M. Grimsditch, and R. H. French, J. Am. Ceram. Soc. **76**, 1132 (1993).

[*Miw93*]   K. Miwa and A. Fukumoto, Phys. Rev. B **48**, 7897 (1993).

[*Miz86*]   M. Mizuta, S. Fujieda, Y. Matsumoto and T. Kawamara, Jpn. J. Appl. Phys. **25**, L945 (1986).

[*Mon74*]   B. Monemar, Phys. Rev. B **10**, 676 (1974).

[*Mor94*]   H. Morkoç, S. Strite, G. B. Gao, M. E. Lin, B. Sverdlov, and M. Burns, J. Appl. Phys. **76**, 1363 (1994).

[*Nak97*]   S. Nakamura and G. Fasol, *The Blue Laser Diode – GaN based Light Emitters and Lasers* (Springer; Berlin, 1997).

[*Nak98*]   S. Nakamura, M. Senoh, S. Nagahama, N. Iwasa, T. Yamada, T. Matsushita, H. Kiyoku, Y. Sugimoto, T. Kozaki, H. Umemoto, M. Sano, and K. Chocho, Appl. Phys. Lett. **72**, 211 (1998).

[*Nye85*]   J. F. Nye, *Physical Properties of Crystals* (Oxford University Press; Oxford, 1985).

[*Ozo01*]   V. Ozoliņš and A. Zunger, Phys. Rev. B **63**, 08 72 02 (2001).

[*Pai89*]   M. J. Paisley, Z. Sitar, J. B. Posthill, and R. F. Davis, J. Vac. Sci. Technol. A **7**, 701 (1989).

[*Pav91*]   P. Pavone, Ph. D. dissertation (*Lattice Dynamics of Semiconductors from Density-Functional Perturbation Theory,* Trieste, 1991).

[*Per92*]   P. Perlin, C. Jauberthie-Carillon, J. P. Itie, A. San Miguel, I. Grzegory, and A. Polian, Phys. Rev. B **45**, 83 (1992).

[*Per93a*]   P. Perlin, A. Polian, J. P. Itie, I. Grzegory, E. Litwin-Staszewska, and T. Suski, Physica B **185**, 426 (1993).

[*Per93b*]   P. Perlin, A. Polian, and T. Suski, Phys. Rev. B **47**, 2874 (1993).

[*Per99*]   P. Perlin, T. Suski, J. W. Ager III, G. Conti, A. Polian, N. E. Christensen, I. Gorczyca, I. Grzegory, E. R. Weber, and E. E. Haller, Phys. Rev. B **60**, 1480 (1999).

[*PGN94*]   *Properties of Group-III Nitrides,* edited by J. H. Edgar (INSPEC, IEE; London, 1994).

[*Phi59*]   J. C. Phillips and L. Kleinman, Phys. Rev. **116**, 287 (1959).

[*Pik81*]   A. N. Pikhtin and A. D. Yas'kov, Sov. Phys. Semicond. **15**, 8 (1981).

[*Per81*]   P. Perdew and A. Zunger, Phys. Rev. B **23**, 5048 (1981).

[*Ple98*]   Th. Pletl, Ph. D. dissertation (*Gitterdynamik mit der ab initio-Methode,* Regensburg, 1998).

[*Pol96*]   A. Polian, M. Grimsditch, and I. Grzegory, J. Appl. Phys. **79**, 3343 (1996).

[*Pro01*]   T. Prokofyeva, M. Seon, J. Vanbuskirk, M. Holtz, S. A. Nikishin, N. N. Faleev, H. Temkin, and S. Zollner, Phys. Rev. B **63**, 12 53 13 (2001).

[*Ram94*]   G. Ramírez-Flores, H. Navarro-Contreras, A. Lastras-Martínez, R. C. Powell, and J. E. Greene, Phys. Rev. B **50**, 8433 (1994).

[*Ric87*]   E. Richter and D. Strauch, Solid State Commun. **64**, 867 (1987).

[*Rie96*]   W. Rieger, T. Metzger, H. Angerer, R. Dimitrov, O. Ambacher, and M. Stutzmann, Appl. Phys. Lett. **68**, 970 (1996).

[*Rob75*]   R. J. Robinson and Z. K. Kun, Appl. Phys. Lett. **27**, 74 (1975).

[*Rom00*]   L. T. Romano, C. G. Van de Walle, J. W. Ager III, W. Götz, and R. S. Kern, J. Appl. Phys. **87**, 7745 (2000).

[*San83*]   J. A. Sanjurjo, E. López-Cruz, P. Vogl, and M Cardona, Phys. Rev. B **28**, 4579 (1983).

[*Sap83*]   J. Sapriel, J. C. Michel, J. C. Tolédano, R. Vacher, J. Kervarec, and A. Regreny, Phys. Rev. B **28**, 2007 (1983).

[*Sar02*]   A. Sarua, M. Kuball, and J. E. Van Nostrand, Appl. Phys. Lett. **81**, 1426 (2002).

[*Sav78*]   V. A. Savastenko and A. U. Sheleg, Phys. Status Solidi A **48**, K135 (1978).

[*Sch77*]   H. Schulz and K. H. Thiemann, Solid State Commun. **23**, 815 (1977).

[*Sen95*]   T. Sengstag, N. Binggeli, and A. Baldereschi, Phys. Rev. B **52**, R8613 (1995).

[*Ser00*]   J. Serrano, A. Rubio, E. Hernández, A. Muñoz, and A. Mujica, Phys. Rev. B **62**, 16 612 (2000).

[*She80*]   W. F. Sherman, J. Phys. C: Solid. St. Phys. **13**, 4601 (1980).

[*She88*]   Y.-T. Shen, D. M. Bylander, and L. Kleinman, Phys. Rev. B **38**, 13 257 (1988).

[*She91*]   M. E. Sherwin and T. J. Drummond, J. Appl. Phys. **69**, 8423 (1991).

[*Shi97*]   E. L. Shirley, X. Zhu, and S. G. Louie, Phys. Rev. B **56**, 6648 (1997).

[*Shi98*]   K. Shimada, T. Sota, and K. Suzuki, J. Appl. Phys. **84**, 4951 (1998).

[*Sie97*]   H. Siegle, A. R. Goñi, C. Thomsen, C. Ulrich, K. Syassen, B. Schöttker, D. J. As, and D. Schikora, MRS Sympos. Proc. **468**, 225 (1997).

[*Sie98*]   H. Siegle, Ph. D. dissertation (*Gitterdynamik und Defekte in Gallium- und Aluminiumnitrid,* Wissenschaft und Technik Verlag; Berlin, 1998).

[*Som98*]   T. Someya and Y. Arakawa, Appl. Phys. Lett. **73**, 3653 (1998).

[*Sri90*]   G. P. Srivastava, *The Physics of Phonons* (Adam Hilger imprint; London, 1990).

[*Tet93*]   M. Teter, Phys. Rev. B **48**, 5031 (1993).

[*Tho27*]   L. H. Thomas, Proc. Cambridge Philos. Soc. **23**, 542 (1927).

[*Tho01*]   M. P. Thompson, G. W. Auner, T. S. Zheleva, K. A. Jones, S. J. Simko, and J. N. Hilfiker, J. Appl. Phys. **89**, 3331 (2001).

[*Tro91*]   N. Troullier and J. L. Martins, Phys. Rev. B **43**, 1993 (1991).

[*Tsu02*]   T. Tsuchiya, K. Kawamura, O. Ohtaka, H. Fukui, and T. Kikegawa, Solid State Commun. **121**, 555 (2002).

[*Uen92*]   M. Ueno, A. Onodera, O. Shimomura, and K. Takemura , Phys. Rev. B **45**, 10 123 (1992).

[*Uen94*]   M. Ueno, M. Yoshida, A. Onodera, O. Shimomura, and K. Takemura, Phys. Rev. B **49**, 14 (1994).

[*Ven75*]   G. Venkataraman, L. A. Feldkamp, and V. C. Sahni, *Dynamics of Perfect Crystals* (The MIT Press; Cambridge, Massachusetts, 1975).

[*Vin86*]   P. Vinet, J. Ferrante, J. R. Smith, and J. H. Rose, J. Phys. C **19**, L467 (1986).

[*Voi10*]   W. Voigt, *Lehrbuch der Kristallphysik* (B. G. Teubner; Leipzig, 1910), p. 962f.

[*Vol96*]   D. Volm, K. Oettinger, T. Streibl, D. Kovalev, M. Ben-Chorin, J. Diener, B. K. Meyer, J. Majewski, L. Eckey, A. Hoffmann, H. Amano, I. Akasaki, K. Hiramatsu, and T. Detchprohm, Phys. Rev. B **53**, 16 543 (1996).

[*Wen78*]   H. Wendel and R. M. Martin, Phys. Rev. Lett. **40**, 950 (1978).

[*Wie97*]   N. Wieser, M. Klose, R. Dassow, G. C. Rohr, F. Scholz, and J. Off, Mater. Sci. Eng. B **50**, 88 (1997).

[*Wie00*]   N. Wieser, Ph. D. dissertation (*Ramanspektroskopie an Gruppe-III-Nitriden,* Technische Universität München, 2000); private communication.

[*Woo87*]   D. M. Wood, S.-H. Wei, and A. Zunger, Phys. Rev. Lett. **58**, 1123 (1987).

[*Wri97*]   A. F. Wright, J. Appl. Phys. **82**, 2833 (1997).

[*Xia93*]   H. Xia, Q. Xia, and A. L. Ruoff, Phys. Rev. B **47**, 12 925 (1993).

[*Yam77*]   M. Yamaguchi, A. Yamamoto, and M. Kondo, J. Appl. Phys. **48**, 196 (1977).

[*Yam97*]   M. Yamaguchi, T. Yagi, T. Azuhata, T. Sota, K. Suzuki, S. Chichibu, and S. Nakamura, J. Phys.: Condens. Matter **9**, 241 (1997).

[*Yam99*]   M. Yamaguchi, T. Yagi, T. Sota, T. Deguchi, K. Shimada, and S. Nakamura, J. Appl. Phys. **85**, 8502 (1999).

[*Yam01*]   S. Yamaguchi, M. Kariya, T. Kashima, S. Nitta, M. Kosaki, Y. Yukawa, H. Amano, and I. Akasaki, Phys. Rev. B **64**, 03 53 18 (2001).

[*Yin80*]   M. T. Yin and M. L. Cohen, Phys. Rev. Lett. **45**, 1004 (1980).

[*Yu97*]   G. Yu, H. Ishikawa, T. Egawa, T. Soga, J. Watanabe, T. Jimbo, and M. Umeno, Jpn. J. Appl. Phys. **36**, L1029 (1997).

[*Zia03*]   E. Ziambaras and E. Schröder, Phys. Rev. B **68**, 06 41 12 (2003).

[*Zim92*]   J. M. Ziman, *Prinzipien der Festkörpertheorie* (Harry Deutsch; Thun und Frankfurt am Main, 2. Auflage 1992).

[*Zor01*]   A. Zoroddu, F. Bernardini, P. Ruggerone, and V. Fiorentini, Phys. Rev. B **64**, 04 52 08 (2001).

Publications

Some results contained in this thesis have already been published in the following articles:

1. J. M. Zhang, T. Ruf, M. Cardona, O. Ambacher, M. Stutzmann, J.-M. Wagner, and F. Bechstedt:
    Raman spectra of isotopic GaN,
    Phys. Rev. B **56**, 14 399 (1997).

2. K. Karch, J.-M. Wagner, and F. Bechstedt:
    Ab initio study of structural, dielectric, and dynamical properties of GaN,
    Phys. Rev. B **57**, 7043 (1998).

3. K. Karch, J.-M. Wagner, H. Siegle, C. Thomsen, and F. Bechstedt:
    Pressure-dependent dynamical and dielectric properties of GaN and AlN,
    Mater. Sci. Forum **264–268**, 303 (1998).

4. J.-M. Wagner, G. Portisch, K. Karch, and F. Bechstedt:
    Properties of strained and unstrained III-nitrides,
    Mater. Sci. Eng. B **59**, 248 (1999).

5. J.-M. Wagner and F. Bechstedt:
    Strain influence on III-nitrides: Ab initio studies of structural, lattice-dynamical, and dielectric properties,
    Phys. Status Solidi B **216**, 793 (1999).

6. J.-M. Wagner and F. Bechstedt:
    Phonon deformation potentials of α-GaN and -AlN: An ab initio calculation,
    Appl. Phys. Lett. **77**, 346 (2000).

7. J.-M. Wagner and F. Bechstedt:
    Pressure dependence of the dielectric and lattice-dynamical properties of GaN and AlN,
    Phys. Rev. B **62**, 4526 (2000).

8. J.-M. Wagner, J. Gleize, and F. Bechstedt:
    Strain effects on structural, dielectric, and lattice-dynamical properties of short-period GaN/AlN superlattices,
    IPAP Conf. Series **1**, 669 (2000).

9. J.-M. Wagner and F. Bechstedt:
    Peculiarities of phonons in strained short-period GaN/AlN superlatices: A first principles study,
    Springer Proceedings in Physics **87**, 883 (2001).

10. A. R. Goñi, H. Siegle, K. Syassen, C. Thomsen, and J.-M. Wagner:
    Effect of pressure on optical phonon modes and transverse effective charges in GaN and AlN,
    Phys. Rev. B **64**, 03 52 05 (2001).

11. J.-M. Wagner and F. Bechstedt:
    Properties of strained wurtzite GaN and AlN: Ab initio studies,
    Phys. Rev. B **66**, 11 52 02 (2002).

12. J.-M. Wagner and F. Bechstedt:
    Electronic and Phonon Deformation Potentials of GaN and AlN: Ab initio Calculations versus Experiment,
    Phys. Status Solidi B **234**, 965 (2002).

13. J.-M. Wagner and F. Bechstedt:
    First-principles study of phonon-mode softening under pressure: the case of GaN and AlN,
    Phys. Status Solidi B **235**, 464 (2003).

14. F. Bechstedt, J. Furthmüller, and J.-M. Wagner:
    Electronic and vibrational properties of group-III nitrides: Ab initio studies,
    Phys. Status Solidi C **0**, 1732 (2003).

Zusammenfassung

In dieser Dissertation werden Untersuchungen der Phononen von Gallium- und Aluminiumnitrid unter dem Einfluß von Verspannungen und von GaN/AlN-Übergittern vorgestellt, die auf parameterfreien numerischen Rechnungen beruhen. Ausgehend von der Dichtefunktionaltheorie (DFT) und der Dichtefunktionalstörungstherie (DFPT) werden im Rahmen der Näherung der lokalen Dichte (LDA) und unter Verwendung von normerhaltenden Pseudopotentialen die Gesamtenergie und das vollständige Phononenspektrum sowie mit der Gitterdynamik zusammenhängende Größen für unterschiedlich deformierte Kristallstrukturen bestimmt. Wo entsprechende experimentelle Daten vorhanden sind, zeigt sich eine gute Übereinstimmung bzw. lassen sich Inkonsistenzen aufzeigen und ihre Ursachen weitestgehend klären; wo diese Daten fehlen (etwa aufgrund unzureichender Probenqualität), stellen die berechneten Ergebnisse eine verläßliche Vorhersage dar. Darüber hinaus ermöglichen die Ergebnisse dieser Arbeit eine physikalische Interpretation der gitterdynamischen Eigenschaften von GaN und AlN sowie ihrer Abhängigkeit von der Deformation des Kristalls.

Das besondere Interesse an den Gruppe-III-Nitridhalbleitern GaN und AlN resultiert aus ihren besoderen Materialeigenschaften. Zusammen mit Indiumnitrid und in Form ternärer und quarternärer Legierungen sind sie für vielfältige Anwendungen in der Mikro- und Optoelektronik geeignet, so etwa für die Herstellung blauer Leuchtdioden und blauer Halbleiterlaser, von Hochleistungstransistoren zur Verstärkung von Mikrowellen, von UV-Photodetektoren, von akustischen Oberflächenwellenbauelementen und von im gesamten sichtbaren Spektralbereich absorbierenden Solarzellen. Insbesondere die Entwicklung des blauen Halbleiterlasers zum Einsatz in der optischen Datenspeicherung war lange Zeit eine treibende Kraft der Forschung und der industriellen Entwicklung auf diesem Gebiet.

Aufgrund der hexagonalen Kristallstruktur und der Wachstumsbedingungen stellt die Deformation der Nitridhalbleiterstrukturen einen Materialparameter von besonderer Bedeutung dar. Die starke spontane und piezoelektrische Polarisation beeinflußt über innere elektrische Felder die elektronischen und optischen Eigenschaften der Bauelemente. Ein einfaches Verfahren zur Ermittlung des Deformationsgrades ist daher sehr wichtig. Prinzipiell ist dies mittels Ramanspektrospkopie möglich, dies setzt aber Referenzwerte von Proben hoher Qualität voraus. Derartige Proben waren lange Zeit nicht vorhanden, und die wenigen experimentell bestimmten elastischen Eigenschaften sowie Phononendaten für deformierte (bzw. verspannte) Nitridschichten wichen deutlich voneinander ab. Diese Schwierigkeiten können durch parameterfreie numerische Rechnungen überwunden werden, die in der Lage sind, die benötigten Daten in verläßlicher Qualität zu ermitteln. Die vorliegende Arbeit widmet sich dieser Aufgabe.

Die DFT-LDA-Rechnungen liefern die Gesamtenergie einer gegebenen Kristallstruktur aus vollständig quantenmechanischen Rechnungen, d. h. ohne Rückgriff auf experimentelle Parameter. Diese Rechnungen werden deshalb auch als Ab-initio-Rechnungen bezeichnet. Bei dem hier verwendeten Programm sind lediglich die atomaren Koordinaten vorzugeben. Die Minimierung der Gesamtenergie zur Bestimmung der Gleichgewichtsstruktur wird durch eine systematische Variation der Atompositionen und einen anschließenden Polynomfit erreicht. Bei hinreichend hoher numerischer Abschneideenergie für die Entwicklung nach ebenen Wellen

führt dieses Verfahren zu sehr genauen Bestimmungen der Gitterkonstanten, Änderungen der dritten Nachkommastelle können aufgelöst werden. Das ist erforderlich, weil die Ergebnisse als Änderungen der untersuchten Größen (Gitterparameter, Phononenfrequenzen, dielektrische Konstante etc.) relativ zu den Gitterkonstantenänderungen angegeben werden. Man hat es dabei mit dem Problem zu tun, daß durch eine kleine Größe geteilt werden muß, daher ist eine Genauigkeit des Endergebnisses im Prozentbereich nur gewährleistet, wenn die einzelnen Gitterkonstanten mit einer Genauigkeit im Sub-Promille-Bereich bestimmt werden. Diese Genauigkeit bei der Bestimmung der Gitterkonstanten wird in der vorliegenden Arbeit erreicht.

Bei der Untersuchung der Volumenmaterialien werden drei verschiedene Deformationen berücksichtigt: Eine Kompression unter hydrostatischem Druck, eine biaxiale Verspannung in der Grundebene und ein uniaxialer Druck senkrecht zur Grundebene. Experimentell werden die beiden erstgenannten Deformationen untersucht. Der uniaxiale Fall liefert jedoch weitere Materialparameter und wird deshalb in die Untersuchungen mit einbezogen. Er verhält sich zudem komplementär zum hydrostatischen Druck und zur biaxialen Verspannung, so daß durch den Vergleich der Ergebnisse der drei unabhängigen Rechnungen eine Konsistenzprüfung möglich ist. Dies setzt jedoch voraus, daß die vollständig relaxierten Strukturen in allen drei Fällen übereinstimmen, weil der unverspannte Zustand der Bezugszustand ist. Nur bei einem identischen Bezugszustand ist es möglich, die Ergebnisse der unterschiedlichen Rechnungen miteinander in Beziehung zu setzen. In der vorliegenden Arbeit wird diese Übereinstimmung erzielt, indem eine sehr große Abschneideenergie gewählt wird.

Für den relaxierten Grundzustand der $3C$- und $2H$-Polytypen von GaN und AlN werden die Gitterkonstanten, der Kompressionsmodul und seine Ableitung nach dem Druck bestimmt. Die zugehörige Zustandsgleichung (d. h. die Druck-Volumen-Beziehung) stimmt hervorragend mit experimentellen Resultaten überein. Des weiteren wird die Kristallgeometrie unter dem Einfluß von hydrostatischem Druck sowie biaxialer und uniaxialer Verspannung berechnet und die Veränderungen der Bindungslängen und -winkel, des Verhältnisses der Gitterkonstanten c/a sowie (für die Wurtzitstruktur) des inneren Parameters u angegeben. Während sich die kubischen Polytypen nahezu identisch verhalten, ergibt sich eine unterschiedliche Deformation von $2H$-GaN und -AlN: GaN zeigt unter hydrostatischem Druck eine proportionale Kontraktion, wohingegen AlN anisotrop deformiert wird. Dies wird durch experimentelle Vergleichsdaten bestätigt. Im Experiment stellt sich der innere Parameter u als schwer zugängliche Größe heraus. Als innere Größe ist er zudem nicht über die makroskopischen elastischen Konstanten bestimmbar. Andererseits ist er ein wichtiger Materialparameter, denn die spontane Polarisation der wurtzitischen Nitride verändert sich wesentlich mit u. Damit liefern die hier erzielten Ergebnisse einen wichtigen Beitrag zur Beschreibung der Materialeigenschaften von GaN und AlN.

Anhand der für verschiedene Verzerrungsstufen unabhängig voneinander bestimmten Ergebnisse zeigt sich, daß sich die beiden Polytypen von GaN und AlN über einen weiten Bereich ($\pm 2\,\%$ Deformation) elastisch nahezu linear verhalten. Aus den Proportionalitätskoeffizienten und dem Kompressionsmodul bestimmen wir die elastischen Konstanten. Durch einen Vergleich der untereinander konsistent bestimmten Ergebnisse dieser Dissertation mit Literaturdaten wird aufgezeigt, welche davon als zuverlässig gelten können und welche nicht.

Für die für verschiedene Verspannungen relaxierten Strukturen wird mittels auf der DFPT beruhenden Rechnungen die dynamischen Matrix, die Tensoren der hochfrequenten Dielektrizitätskonstante sowie der effektiven Ladungen der einzelnen Ionen bestimmt. Diese Rech-

nungen sind in ihrem numerischen Aufwand denen der Gesamtenergieberechnung vergleichbar und ermöglichen die Bestimmung des kompletten Phononenspektrums am Γ-Punkt (oder an einem anderen Punkt der Brillouinzone) allein mit Hilfe der primitiven Zelle. Durch die störungstheoretische Herangehensweise ist keine Superzellenrechnung erforderlich, um auch die LO-Moden zu erhalten. Anhand des Phononeneigenvektors läßt sich die Symmetrie der Mode erkennen und die berechnete Frequenz entsprechend klassifizieren. Mittels der verallgemeinerten Lyddane-Sachs-Teller-Relation läßt sich zudem anhand der LO- und TO-Frequenzen die statische Dielektrizitätskonstante aus der hochfrequenten berechnen.

Zusammen mit den Strukturbestimmungen liefert dies die Druck- und Verspannungsabhängigkeit der dielektrischen Größen und der Phononenfrequenzen. Daraus werden entsprechend die Moden-Grüneisenparameter, die biaxialen bzw. uniaxialen Modenkoeffizienten und die Phononen-Deformationspotentiale berechnet. Insbesondere werden in dieser Arbeit erstmalig Phononen-Deformationspotentiale für AlN bestimmt; experimentelle Werte lagen dafür lange Zeit nicht vor. Die dielektrischen Eigenschaften (Tensor der statischen und der hochfrequenten Dielektrizitätskonstante sowie der Bornschen effektive Ladungen) zeigen ausgeprägte Nichtlinearitäten in Abhängigkeit von der Deformation.

Die untere (niederfrequente) E_2-Phononenmode der $2H$-Polytypen zeigt eine Besonderheit in ihrer Druck- und Verspannungsabhängigkeit: Entgegen dem Trend aller anderen Moden, bei kompressiver Deformation zu höheren Werten zu verschieben, nimmt die Frequenz dieser Mode ab. Dieses sogenannte Softening ist aber nur schwach ausgeprägt, so daß das Verhalten dieser Mode nicht mit dem vom äußeren Druck hervorgerufenen strukturellen Phasenübergang der Nitride zusammenhängt. Im Sinne einer Faltung der Brillouinzone, die man für den Vergleich der Eigenschaften der $3C$- und $2H$-Polytypen annehmen kann, entspricht die untere E_2-Mode einem transversal-akustischen Zonenrandphonon der $3C$-Polytypen. Auch für diese Moden finden wir eine Frequenzabnahme unter Druck. Dieses Verhalten ist von anderen Materialien her bekannt. Für Silizium wurde es mit einer Veränderung des Zusammenspiels von Zentral- und Winkelkräften erklärt. Wegen der hohen Ionizität der Nitridhalbleiter und der unterschiedlichen Anion- und Kation-Massen läßt sich dieses einfache Modell jedoch nicht auf GaN und AlN übertragen. Unter Verwendung der sogenannten Frozen-Phonon-Methode zeigen wir, daß die Frequenzabnahme der unteren E_2-Mode unter Druck aus einem unterschiedlichen Zusammenspiel von Ewald- und Hartree-Energie resultiert. Dabei zeigen sich zum einen Unterschiede zwischen $2H$-GaN und -AlN, zum anderen stellt sich heraus, daß die Frequenzzunahme der oberen (höherfrequenten) E_2-Mode auf einen Rollentausch des Einflusses der Ewald- und der Hartree-Energie zurückgeht.

Unsere Ergebnisse zur Druckabhängigkeit der Phononenfrequenzen tragen überdies entscheidend dazu bei, in einer Kooperation mit Experimentatoren das Verhalten der LO-TO-Aufspaltung unter Druck zu erklären. Die auch experimentell gefundene Zunahme der LO-TO-Aufspaltung geht nicht auf eine Zunahme der Ionizität zurück (wie es bei SiC der Fall ist), sondern auf eine Abnahme der dielektrischen Abschirmung: Sowohl die Bornsche effektive Ladung als auch die hochfrequente Dielektrizitätskonstante nehmen unter Druck ab. Die Abnahme der Dielektrizitätskonstante ist dabei stärker ausgeprägt, so daß die abgeschirmte effektive Ladung zunimmt; letztere ist die für die LO-TO-Aufspaltung maßgebliche gitterdynamische Größe.

Die berechneten Ergebnisse zur Abhängigkeit der gitterdynamischen Eigenschaften von der Verspannung werden detailliert mit experimentellen Befunden verglichen. Dabei zeigt sich bezüglich des hydrostatischen Druckes eine systematische Abweichung der Rechnungen gegenüber dem Experiment: Die Moden-Grüneisenparameter sowohl des AlN als auch des GaN werden um ca. 20 % unterschätzt. Der Grund für diese Abweichungen ist unklar: Weil sie sowohl bei AlN als auch bei GaN auftreten, können sie nicht durch die nur beim Ga-Atom verwendete nichtlineare Rumpfkorrektur verursacht sein. Vielmehr ist zu vermuten, daß sie mit einer unzureichenden Beschreibung der elektronischen Zustände (insbesondere der Bandlücke) und ihrer Druck- bzw. Verspannungsabhängigkeit zusammenhängen. Dieses Problem ist unerwartet aufgetreten, mit der gleichen Methode ist zuvor eine sehr gute Übereinstimmung der Ergebnisse für SiC sowie für andere III-V-Halbleiter (insbesondere Arsenide) erzielt worden. Diese systematische Abweichung schmälert den Wert der in dieser Dissertation enthaltenen Ergebnisse jedoch nur unerheblich, weil die Größenverhältnisse richtig wiedergegeben werden. Dies betrifft sowohl die Größe der Koeffizienten verschiedener Moden eines Materials als auch den Vergleich verschiedener Materialien bzw. Polytypen.

Bei einem Vergleich der berechneten Koeffizienten für biaxiale Verspannung mit entsprechenden experimentellen Daten ergeben sich weitaus größere Abweichungen, als sie nach den zuvor beschriebenen Befunden zu erwarten sind. Bei einer eingehenden Prüfung stellt sich heraus, daß viele der Abweichungen auf Fehler in der Auswertung oder auf die Verwendung unzuverlässiger Daten zurückgehen, die für die Umrechnung der unmittelbar gemessenen Größen benutzt werden. Nach einer entsprechenden Korrektur ergibt sich eine wesentlich bessere Übereinstimmung sowohl der experimentellen Daten mit den in dieser Arbeit berechneten Ergebnissen als auch der experimentellen Daten untereinander. Eine Konsequenz dieser Revision häufig verwendeter experimenteller Materialparameter ist, daß die anhand von Ramanmessungen ermittelte Verspannung größer ist als bislang angenommen.

Bei der Untersuchung der Struktur und der Phononenmoden kurzperiodischer Übergitter, die als Modellsystem für Heterostrukturen dienen, lassen sich einige Besonderheiten feststellen. Die innere Relaxation des Übergitters resultiert in einer Geometrie, die von der mittels der elastischen Konstanten bestimmten abweicht. Dies zeigt sich besonders deutlich bei den hexagonalen Übergittern, bei denen sich die Höhen der GaN- und der AlN-Schicht in entgegengesetzter Weise ändern, als es von der makroskopischen Theorie her zu erwarten ist. Bei den Phononen ergibt sich ein deutlich anderes Bild, als es von GaAs/AlAs-Übergittern her bekannt ist. Durch die energetische Ordnung der Moden und den partiellen Überlap der Phononendispersionen der Volumenmaterialien, die in dem entsprechenden Verspannungszustand zu kombinieren sind, ergibt sich eine Aufteilung des resultierenden Spektrums in die Bereiche sämtlicher LO- und sämtlicher TO-Moden sowie der akustischen Moden.

Die gegenseitige pseudomorphe Verspannung der GaN- und AlN-Schichten führt zu einer Vergrößerung des Frequenzunterschiedes der TA-Moden von GaN und AlN. Infolgedessen treten auf die AlN-Schichten begrenzte TA-Moden auf, die obersten LA-Moden sind dagegen nicht vollständig auf die AlN-Schichten begrenzt. Bis auf eine sind die TO-Moden ebenfalls schichtbegrenzte Moden; sie sind in der Schichtebene polarisiert. Die ein davon abweichendes Verhalten zeigende ausgebreitete TO-Mode findet sich im Frequenzbereich der GaN-TO-Moden. Ihre Frequenz stellt eine der dielektrischen Dispersionsfrequenzen dar, und sie ist längs der Stapelungsrichtung polarisiert. Im Bereich der Bandlücke zwischen den AlN- und den GaN-

artigen TO-Moden tritt für alle Übergitter, unabhängig von der Anzahl der Schichten, eine polare Grenzschichtmode auf, die eine stark ausgeprägte Winkelabhängigkeit aufweist. Mit Ausnahme der von Stickstoffauslenkungen dominierten sind auch die LO-Moden stark winkelabhängig. Bis auf die oberste sind die LO-Moden für alle Ausbreitungsrichtungen im wesentlichen in der Stapelungsrichtung des Übergitters polarisiert. Dagegen ändert die oberste LO-Mode ihre Polarisationsrichtung mit der Ausbreitungsrichtung. Sie ist zudem stark IR-aktiv, so daß sie für alle Ausbreitungsrichtungen an das makroskopische elektrische Feld koppelt, analog zu der polaren LO-Mode eines Volumenmaterials. Die Verspannungsabhängigkeit aller Übergittermoden wird durch die der reinen Volumenmaterialien bestimmt. Insgesamt zeigen die kurzperiodischen Übergitter sowohl einige der für dickere Übergitter typischen Phononeneigenschaften (schichtbegrenzte Moden und Grenzflächenmoden) als auch eine sehr große Ähnlichkeit zu den Eigenschaften eines Volumenmaterials.

Anhand der hier vorgestellten Ergebnisse läßt sich bereits erkennen, welche weitergehenden Untersuchungen möglich bzw. sinnvoll wären. Am dringlichsten sind analoge Untersuchungen zum InN, welches sich der Berechnung lange Zeit entzogen hat. Zum einen ist die Bandlücke des InN in der DFT-LDA-Rechnung verschwindend gering bzw. kann sie negativ werden, was zu Problemen bei der Berechnung der Phononen führt. Zum anderen zeigt sich, daß die Verwendung der nichtlinearen Rumpfkorrektur nicht ausreicht, um den Einfluß der Rumpfelektronen richtig zu beschreiben. Obwohl die Gitterkonstante und die Dielektrizitätskonstante bei Verwendung der NLCC in guter Übereinstimmung mit experimentellen Daten erhalten werden (die aber für InN ebenfalls kritisch sind), schlägt die Berechnung der Phononen fehl. Erst mit einem Pseudopotential, das die $4d$-Elekronen voll als Valenzelektronen berücksichtigt, gelangt man mittels DFPT-Rechnungen zu brauchbaren Ergebnissen.

Die hier benutzten Verfahren lassen sich vertieft auf Details der strukturellen und der Phononeneigenschaften sowie ihrer Deformationsabhängigkeit anwenden, etwa um unterschiedliches Verhalten in Abhängigkeit von der Modensymmetrie zu untersuchen (analog zu dem Vergleich der E_2^{low}- und der E_2^{high}-Mode). An vielen Stellen ergeben sich Hinweise, daß die hohe Ionizität der Nitride eine wichtige Rolle bereits bei den strukturellen Eigenschaften spielt. Sehr sinnvoll ist es daher, die Veränderung der statischen Ionizität unter Deformationseinfluß auch für die $2H$-Polytypen zu untersuchen. Wegen der geringeren Symmetrie ist das Verfahen von Garcia und Cohen jedoch nicht anwendbar. Hier würden auf der Berry-Phasen-Methode beruhende Rechnungen weiterhelfen.

Die wichtigste Erweiterung stellt jedoch zweifelsohne die Ab-initio-Berechnung der Phononen von Mischkristallen dar. Aus Modellrechnungen ist das zu erwartende Ein- bzw. Zwei-Moden-Verhalten bestimmter Mischkristalle bereits bekannt, daher kann die einfache Näherung des virtuellen Kristalls nicht verwendet werden. Eine generelle Möglichkeit der Berechnung besteht in einer Clusterentwicklung, eine andere in der Verwendung einer Superzelle mit zufällig durchmischter atomarer Verteilung. Letzteres ist jedoch aufgrund der hohen erforderlichen Abschneideenergie bei der Verwendung normerhaltender Pseudopotentiale ein illusorisches Unterfangen. Hier wären sinnvollerweise nichtnormerhaltende Vanderbilt-Pseudopotentiale zu verwenden.

Lebenslauf

Name	Jan-Martin Wagner
Geburtstag	24. Juli 1967
Geburtsort	Berlin
Familienstand	ledig
Staatsangehörigkeit	deutsch
Eltern	Dorothe Wagner, geb. Berckenbrinck, Kindergärtnerin
	Hans-Günter Wagner, Diplomingenieur

1973–1977	Grundschule am Buschgraben, Berlin-Zehlendorf
1977–1979	Nord-Grundschule, Berlin-Zehlendorf
1979–1985	Schadow-Oberschule (Gymnasium), Berlin-Zehlendorf
Dezember 1985	Abitur (Gesamtnote: 1,5)

1986–1996	Studium der Physik, Technische Universität Berlin
1988	Werkstattpraktikum (Metallbearbeitung) in der Schweißtechnischen Lehr- und Versuchsanstalt Berlin
1989–1993	Tutor für Theoretische Physik, Institut für Theoretische Physik der TU Berlin
November 1996	Physik-Diplom (Gesamturteil: sehr gut); Thema der Diplomarbeit: „Höhere Ordnungen bei der entarteten Vierwellenmischung in Halbleitern. Untersuchung exzitonischer Zweiniveausysteme" (Betreuer: Prof. Dr. I. Broser; Kooperation: Prof. Dr. R. Zimmermann, Humboldt-Universität zu Berlin)

1997–heute	Arbeit an der Dissertation bei Prof. Dr. F. Bechstedt, Friedrich-Schiller-Universität Jena
1997–2002	Wissenschaftlicher Mitarbeiter am Institut für Festkörpertheorie und Theoretische Optik (heute: „und -optik") der FSU im Rahmen des DFG-Schwerpunktprogramms „Gruppe-III-Nitride und ihre Heterostrukturen: Wachstum, materialwissenschaftliche Grundlagen und Anwendungen" (SPP 1032)

Jena, den 13. Mai 2004

Ehrenwörtliche Erklärung

Ich erkläre hiermit ehrenwörtlich, daß ich die vorliegende Arbeit selbständig, ohne unzulässige Hilfe Dritter und ohne Benutzung anderer als der angegebenen Hilfsmittel und Literatur angefertigt habe. Die aus anderen Quellen direkt oder indirekt übernommenen Daten und Konzepte sind unter Angaben der Quelle gekennzeichnet.

Bei der Auswahl und Auswertung des Materials haben mir die nachstehend aufgeführten Personen in der jeweils beschriebenen Weise unentgeltlich geholfen:
1. Prof. Dr. Friedhelm Bechstedt (als betreuender Hochschullehrer),
2. Dr. Krystian Karch (Betreuung in der Einarbeitungsphase),
3. Dr. habil. Pasquale Pavone (technische Hilfen zum Programmcode).

Weitere Personen waren an der inhaltlich-materiellen Erstellung der vorliegenden Arbeit nicht beteiligt. Insbesondere habe ich hierfür nicht die entgeltliche Hilfe von Vermittlungs- bzw. Beratungsdiensten (Promotionsberater oder andere Personen) in Anspruch genommen. Niemand hat von mir unmittelbar oder mittelbar geldwerte Leistungen für Arbeiten enthalten, die im Zusammenhang mit dem Inhalt der vorgelegten Dissertation stehen.

Die Arbeit wurde bisher weder im In- noch im Ausland in gleicher oder ähnlicher Form einer anderen Prüfungsbehörde vorgelegt.

Die geltende Promotionsordnung der Physikalisch-Astronomischen Fakultät ist mir bekannt.

Ich versichere ehrenwörtlich, daß ich nach bestem Wissen die reine Wahrheit gesagt und nichts verschwiegen habe.

Jena, den 13. Mai 2004

Danksagung

Ich möchte mich bei allen herzlich bedanken, die mich bei dieser Arbeit unterstützt und zu ihrem Gelingen beigetragen haben, sei es durch eine physikalische Diskussion, in Form von praktischer Unterweisung im Umgang mit Rechnern und Programmen oder einfach nur durch ihre Anwesenheit im richtigen Moment.

Vor allem danke ich meinem Betreuer und Doktorvater Prof. Friedhelm Bechstedt für seine optimistische Geduld, seine immerwährende Diskussionsbereitschaft und für die Freiheit, die ich bei der Wahl von Wegen, Zeit und Ziel hatte. Nichtsdestoweniger waren seine Ideen und sein unermüdliches Interesse am Fortgang der Arbeit für ihr Gelingen und für die Fülle der Ergebnisse von großer Bedeutung.

Für die schnelle Einarbeitung in die Handhabung der Programme und die Betreuung in den ersten Wochen danke ich Dr. Krystian Karch. Technische Unterstützung bei der und physikalisches Verständnis rund um die Phononenberechnung verdanke ich Dr. habil. Pasquale Pavone und Dr. Thomas Pletl, denen ich zudem für ihre Gastfreundschaft bei meinen Aufenthalten in Regensburg danke. Für finanzielle Unterstützung danke ich der Deutschen Forschungsgemeinschaft (Projekt Be1346/8), für Rechenzeit dem John-von-Neumann-Institut für Computing im Forschungszentrum Jülich (Projekt hjn10).

Im Rahmen dieser Arbeit haben sich einige interessante Kontakte ergeben. Für physikalische Diskussionen bzw. die Bereitstellung experimenteller Ergebnisse danke ich Prof. Alejandro Goñi, Dr. Henrik Siegle, Dr. Jérôme Gleize und Dr. Nicolai Wieser. Wertvolle Hinweise zur Frozen-phonon-Methode verdanke ich Prof. Gyaneshwar P. Srivastava. Für die Übernahme der externen Gutachten und die lebhafte Diskussion bei der Verteidigung danke ich Prof. Dieter Strauch und Dr. habil. Axel Hoffmann. Ein ganz besonderer Dank gilt Dr. habil. Robert Heitz († 2003) für seinen Blick von außen und seine stete Anregung zum Perspektivwechsel.

Darüber hinaus danke ich allen Kolleginnen und Kollegen am IFTO für ihre Hilfsbereitschaft und die gute Arbeitsatmosphäre, insbesondere unserer Sekretärin Sylvia Hofmann und unserer Computeradministratorin Dipl.-Phys. Marion Fiedler. Für in mancherlei Diskussionen über eine Vielzahl von Themen und Dingen gewonnene tiefgehende Einsichten danke ich Dr. Hans-Christian Weißker, ihm verdanke ich auch meinen Doktorhut. Meinem langjährigen Zimmer- und Konferenzgefährten Dr. Karsten Hannewald danke ich speziell für einen bestimmten Postertransport. Für ihr offenes Ohr bzw. diverse Aufmunterungen danke ich Dr. Andreas Zywietz, Dr. Luis Ramos und Dr. Andrej Stekolnikov; Dr. Birgit Adolph danke ich besonders herzlich für das Korrekturlesen des Manuskripts. – Außerdem danke ich Reinhard K. Köhler für seine Motivationskünste und dafür, daß er nicht mit ihnen gegeizt hat.

Zum Schluß danke ich von ganzem Herzen meinen Eltern.